



# Politecnico di Bari

Repository Istituzionale dei Prodotti della Ricerca del Politecnico di Bari

Design and characterization of resonant devices for optical applications

This is a PhD Thesis

*Original Citation:*

Design and characterization of resonant devices for optical applications / Kashif, Muhammad Fayyaz. - ELETTRONICO. - (2022). [10.60576/poliba/iris/kashif-muhammad-fayyaz\_phd2022]

*Availability:*

This version is available at <http://hdl.handle.net/11589/232998> since: 2021-12-30

*Published version*

DOI:10.60576/poliba/iris/kashif-muhammad-fayyaz\_phd2022

Publisher: Politecnico di Bari

*Terms of use:*

(Article begins on next page)



Politecnico  
di Bari

Department of Electrical and Information Engineering  
ELECTRICAL AND INFORMATION ENGINEERING  
PH.D. PROGRAM

SSD: ING-INF/02-ELECTROMAGNETIC FIELDS

---

# Design and Characterization of Resonant Devices for Optical Applications

---

*Author:*

Muhammad Fayyaz KASHIF

*Supervisor:*

Prof. Marco GRANDE

A thesis submitted to the *Polytechnic University of Bari* in fulfillment of the  
requirement for the degree of Doctor of Philosophy.

---

Course no: XXXIV, 01/11/2018 - 31/10/2021





Politecnico  
di Bari

Department of Electrical and Information Engineering  
ELECTRICAL AND INFORMATION ENGINEERING  
PH.D. PROGRAM

SSD: ING-INF/02-ELECTROMAGNETIC FIELDS

DOCTORAL THESIS

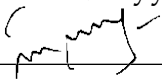
---

**Design and Characterization of Resonant Devices  
for Optical Applications**

---

*Author:*

Muhammad Fayyaz KASHIF


  
\_\_\_\_\_ *firma*

*Referees:*

Prof. Fabio BARONIO  
Dr. Valeria MARROCCO

*Supervisor:*

Prof. Marco GRANDE

—  MARCO GRANDE  
30.12.2021  
15:47:09 UTC *firma*

*Coordinator Ph.D. Program:*

Prof.  CARPENTIERI MARIO

—   
\_\_\_\_\_ *firma*

---

RSA/2048 bits  
Course no: XXXIV, 01/11/2018 - 31/10/2021



# Liberatoria per L'Archiviazione della Tesi di Dottorato

Il/la sottoscritto **Muhammad Fayyaz KASHIF** nato a **Mianwali** il **20/12/1986** residente a **Lecce** in **Enrico de Nicola 2A** iscritto al 3° anno di Corso di Dottorato di Ricerca in **Ingegneria Elettrica e dell'Informazione** ciclo **XXXIV** ed essendo stato ammesso a sostenere l'esame finale con la prevista discussione della tesi dal titolo:

**Design and Characterization of Resonant Devices for Optical Applications**


## DICHIARA

1. di essere consapevole che, ai sensi del D.P.R. n. 445 del 28.12.2000, le dichiarazioni mendaci, la falsità negli atti e l'uso di atti falsi sono puniti ai sensi del codice penale e delle Leggi speciali in materia, e che nel caso ricorressero dette ipotesi, decade fin dall'inizio e senza necessità di nessuna formalità dai benefici conseguenti al provvedimento emanato sulla base di tali dichiarazioni;
2. di essere iscritto al Corso di Dottorato di ricerca **Ingegneria Elettrica e dell'Informazione** ciclo **XXXIV**, corso attivato ai sensi del "Regolamento dei Corsi di Dottorato di ricerca del Politecnico di Bari", emanato con D.R. n.286 del 01.07.2013;
3. di essere pienamente a conoscenza delle disposizioni contenute nel predetto Regolamento in merito alla procedura di deposito, pubblicazione e autoarchiviazione della tesi di dottorato nell'Archivio Istituzionale ad accesso aperto alla letteratura scientifica;
4. di essere consapevole che attraverso l'autoarchiviazione delle tesi nell'Archivio Istituzionale ad accesso aperto alla letteratura scientifica del Politecnico di Bari (IRIS-POLIBA), l'Ateneo archiverà e renderà consultabile in rete (nel rispetto della Policy di Ateneo di cui al D.R. 642 del 13.11.2015) il testo completo della tesi di dottorato, fatta salva la possibilità di sottoscrizione di apposite licenze per le relative condizioni di utilizzo (<http://www.creativecommons.it/Licenze>), e fatte salve, altresì, le eventuali esigenze di "embargo", legate a strette considerazioni sulla tutelabilità e sfruttamento industriale/commerciale dei contenuti della tesi, da rappresentarsi mediante compilazione e sottoscrizione del modulo in calce (Richiesta di embargo);

5. che la tesi da depositare in IRIS-POLIBA, in formato digitale (PDF/A) sarà del tutto identica a quelle consegnate/inviolate/da inviarsi ai componenti della commissione per l'esame finale e a qualsiasi altra copia depositata presso gli Uffici del Politecnico di Bari in forma cartacea o digitale, ovvero a quella da discutere in sede di esame finale, a quella da depositare, a cura dell'Ateneo, presso le Biblioteche Nazionali Centrali di Roma e Firenze e presso tutti gli Uffici competenti per legge al momento del deposito stesso, e che di conseguenza va esclusa qualsiasi responsabilità del Politecnico di Bari per quanto riguarda eventuali errori, imprecisioni o omissioni nei contenuti della tesi;
6. che il contenuto e l'organizzazione della tesi è opera originale realizzata dal sottoscritto e non compromette in alcun modo i diritti di terzi, ivi compresi quelli relativi alla sicurezza dei dati personali; che pertanto il Politecnico di Bari ed i suoi funzionari sono in ogni caso esenti da responsabilità di qualsivoglia natura: civile, amministrativa e penale e saranno dal sottoscritto tenuti indenni da qualsiasi richiesta o rivendicazione da parte di terzi;
7. che il contenuto della tesi non infrange in alcun modo il diritto d'Autore né gli obblighi connessi alla salvaguardia di diritti morali od economici di altri autori o di altri aventi diritto, sia per testi, immagini, foto, tabelle, o altre parti di cui la tesi è composta.

Luogo e data: Bari, 30/12/2021

Firma:



Il/La sottoscritto, con l'autoarchiviazione della propria tesi di dottorato nell'Archivio Istituzionale ad accesso aperto del Politecnico di Bari (POLIBA-IRIS), pur mantenendo su di essa tutti i diritti d'autore, morali ed economici, ai sensi della normativa vigente (Legge 633/1941 e ss.mm.ii.),

**CONCEDE**

- al Politecnico di Bari il permesso di trasferire l'opera su qualsiasi supporto e di convertirla in qualsiasi formato al fine di una corretta conservazione nel tempo. Il Politecnico di Bari garantisce che non verrà effettuata alcuna modifica al contenuto e alla struttura dell'opera.
- al Politecnico di Bari la possibilità di riprodurre l'opera in più di una copia per fini di sicurezza, back-up e conservazione.

Luogo e data: Bari, 30/12/2021

Firma:



# Abstract

Muhammad Fayyaz KASHIF

*Design and Characterization of Resonant Devices for Optical Applications*

Periodic structures have attracted huge research interest over the past many years due to their interesting electromagnetic properties. There are lots of useful applications in the fields of photonics and microwave engineering that come from periodic structures. Examples of periodic structures include diffraction gratings, photonic crystals, phased array antennas, frequency selective surfaces, and metamaterials. A diffraction grating is composed of diffracting elements arranged periodically. The spacing between these elements is comparable to the wavelength of the incident light. The amplitude, or phase, or both, of the diffracted electromagnetic radiation from a diffraction grating, can be modified in a controlled and predictable manner. Another interesting phenomenon is the presence of sharp resonant features in the optical spectra of the gratings such as Guided-Mode Resonances (GMR). GMR gratings have been employed in wide-ranging applications such as sensors for biosensing, optical absorbers, efficient photodetectors and tunable filters for optical communication systems, reflection mirrors for lasers, and spectrometers.

The first part of this work focuses on the design, fabrication, and characterization of resonant pillar gratings. This is further split into two parts. The first part describes the graphene-based pillar grating for optical absorber applications. The performance of the proposed periodic structure is investigated through numerical simulations. The proposed design exploits the guided mode resonances of the structure to achieve enhanced absorption in the monolayer graphene. In the second part, a phase change material vanadium-dioxide ( $\text{VO}_2$ ) is integrated with the pillar grating structure to achieve the thermal tuning of the optical response exploiting the phase change properties of  $\text{VO}_2$ . The grating has been fabricated utilizing a nanoimprint lithography system exploiting a silicon mold.  $\text{VO}_2$  nano-powders have been deposited by spin-coating. In addition to the experimental tests, the proposed structure is simulated using the RCWA method.

Next, plasmonic grating structures on planar as well curved surfaces are designed and analyzed through numerical simulations for sensing and Surface Enhanced Raman Spectroscopy (SERS) applications. The work related to plasmonic

structures has also been further split into two parts. In the first part, a planar plasmonic grating is designed and synthesized for sensing applications in the transmission domain exploiting Extraordinary Transmittance (EOT) properties of the plasmonic modes as well as the sensitivity of these modes to the changes in the refractive index of the surrounding media. A Finite Difference Time Domain (FDTD) model of the finite set of nanoplatelets has been developed to theoretically investigate and optimize the nanostructure as well as validate the experimental results. Plasmonic modes can concentrate light to much smaller locations creating field hotspots. This makes plasmonic structures a suitable platform for SERS. In the second part of the work, plasmonic gratings on planar and curved surfaces are investigated as SERS platforms.

# Publications

## Journal Papers

1. F. Pisano, **M. F. Kashif**, A. Balena, M. Pisanello, F. De Angelis, L. M. de la Prida, M. Valiente, A. D’Orazio, M. De Vittorio, M. Grande, and F. Pisanello, “Plasmonics on a neural implant: Engineering light–matter interactions on the non-planar surface of tapered optical fibers,” *Advanced Optical Materials*, p. 2101649, 2021.
2. F. Pisano, A. Balena, **M. F. Kashif**, M. Pisanello, G. de Marzo, L. Algieri, A. Quattieri, L. Sileo, T. Stomeo, A. D’Orazio, M. D. Vittorio, F. Pisanello, and M. Grande, “High transmission from 2d periodic plasmonic fiite arrays with sub-20 nm gaps realized with ga focused ion beam milling,” *Nanotechnology*, vol. 31, no. 43, p. 435301, 2020.
3. **M. F. Kashif**, G. V. Bianco, T. Stomeo, M. A. Vincenti, D. de Ceglia, M. De Vittorio, M. Scalora, G. Bruno, A. D’Orazio, and M. Grande, “Graphene-based cylindrical pillar gratings for polarization-insensitive optical absorbers,” *Applied Sciences*, vol. 9, no. 12, 2019.

## Conference Proceedings

1. **M. F. Kashif**, T. Stomeo, F. Guido, M. A. Vincenti, I. Vassalini, M. De Vittorio, A. D’Orazio, I. Alessandri, C. De Angelis, M. Grande, and D. de Ceglia, “Tuning the optical response of a dielectric grating using vanadium-dioxide as a phase-change material,” in *Society of Photo-Optical Instrumentation Engineers (SPIE) Conference Series*, vol. 11796 of *Society of Photo-Optical Instrumentation Engineers (SPIE) Conference Series*, p. 1179621, 2021
2. **M. F. Kashif**, A. D’Orazio, M. Grande, T. Stomeo, F. Guido, M. de Vittorio, M. A. Vincenti, I. Vassalini, I. Alessandri, C. de Angelis, and D. de Ceglia, “Thermal tuning of resonant gratings using a phase-change material,” in *22nd International Conference on Transparent Optical Networks (ICTON)*, pp. 1–4, 2020.
3. **M. F. Kashif**, F. Pisano, A. Balena, M. Pisanello, T. Stomeo, F. Pisanello, M. De Vittorio, A. D’Orazio, and M. Grande, “Plasmonic nanostructures on curved surfaces for fiber-based sensors,” in *22nd International Conference on Transparent Optical Networks (ICTON)*, pp. 1–4, 2020.
4. **M. F. Kashif**, F. Pisano, A. Balena, M. Pisanello, T. Stomeo, M. De Vittorio, F. Pisanello, A. D’Orazio, and M. Grande, “Segmented-wave analysis of nano-gratings on curved surfaces,” in *2020 Italian Conference on Optics and Photonics (ICOP)*, pp. 1–3, 2020.

5. **M. F. Kashif**, F. Pisano, A. Balena, M. Pisanello, G. de Marzo, L. Algieri, A. Qaltieri, L. Sileo, T. Stomeo, A. D’Orazio, M. D. Vittorio, F. Pisanello, and M. Grande, “Optical properties of finite subsets of finite-milled 2d periodic arrays of gold nanoplatelets with sub-20-nm gaps,” in *Frontiers in Optics / Laser Science*, p. JTh4B.6, Optical Society of America, 2020.
6. M. Grande, G. V. Bianco, **M.F. Kashif**, M. Scalora, G. Bruno and A. D’Orazio, “Reconfigurable and Optically Transparent Graphene-Based Devices” *ICTON 2019*, doi: 10.1109/ICTON.2019.8840518

### Conference Presentations

1. **M. F. Kashif**, T. Stomeo, F. Guido, M. A. Vincenti, I. Vassalini, M. De Vittorio, A. D’Orazio, I. Alessandri, C. De Angelis, M. Grande, D. de Ceglia, " Fabrication of vanadium-dioxide for thermal tuning in photonic structures," 47th Micro and Nano Engineering Conference (MNE), Turin, 2021.
2. **M. F. Kashif**, “Applications of Photonic Technologies for Smart Mobility”, International Workshop on Smart Mobility in Future Cities: The Apulia Industry Summit, Bari, October, 2019.
3. **M. F. Kashif**, Giuseppe Valerio Bianco, Tiziana Stomeo, Maria Antonietta Vincenti, Domenico de Ceglia, Massimo De Vittorio, Michael Scalora, Giovanni Bruno, Antonella D’Orazio, and Marco Grande “Graphene-Based Cylindrical Pillar Gratings for Polarization-Insensitive Optical Absorbers”, *Photonics & Electromagnetics Research Symposium (PIERS)*, Rome, June 2019.

# Acknowledgements

I would first like to thank my supervisor, Prof. Marco Grande, for his continuous support and guidance throughout my stay in his laboratory. He provided me with a great research environment and facilities. He gave me opportunities to be part of his collaborative projects with other research groups and always encouraged me to participate in international conferences and workshops. This has greatly helped me sharpen my research skills and broaden my vision. I would also like to thank the head of our research group, Prof. Antonella D'Orazio, for her administrative support that helped me smoothly continue my work.

I would like to thank all of my colleagues at nPEG for their advice and valuable discussions. I would say special thanks to Ilaria Marasco and Giovanni Niro for their great help in resolving administrative issues at various times. I would also thank my colleague Gennaro Gelao for his help on different occasions and fruitful discussions.

I would like to acknowledge my colleagues from the Italian Institute of Technology (IIT) Lecce for their wonderful collaboration. I would particularly like to thank Dr. Tiziana Stomeo for her help with device fabrication at IIT clean room.

Finally, I would like to thank my parents, my uncle Sultan Ahmad, my siblings, and my wife Samar for their support, love, and prayers. In particular, I would like to acknowledge my elder brother Irshad Ahmad for his continuous parental support to me throughout my academic career.



# Contents

<b>Liberatoria per L'Archiviazione della Tesi di Dottorato</b>	<b>iii</b>
<b>Abstract</b>	<b>v</b>
<b>Publications</b>	<b>vii</b>
<b>Acknowledgements</b>	<b>ix</b>
<b>List of Figures</b>	<b>xiii</b>
<b>List of Tables</b>	<b>xxi</b>
<b>1 Introduction to Periodic Structures</b>	<b>1</b>
1.1 Dielectric function of materials . . . . .	3
1.1.1 Lorentz model for metals . . . . .	5
1.1.2 Drude model for metals . . . . .	7
1.1.3 Drude-Lorentz model . . . . .	8
1.1.4 Sellmeier equation . . . . .	10
1.1.5 Nonlinear properties of materials . . . . .	11
1.2 Graphene . . . . .	12
1.3 Vanadium dioxide ( $\text{VO}_2$ ) . . . . .	13
1.4 Numerical methods in electromagnetics . . . . .	15
1.4.1 Finite Difference Time Domain (FDTD) method . . . . .	15
1.4.2 Rigorous Coupled Wave Analysis (RCWA) method . . . . .	17
1.4.3 Beam Propagation Method (BPM) . . . . .	18
<b>2 Design, Fabrication, and Characterization of Pillar Gratings</b>	<b>23</b>
2.1 Guided-Mode Resonance . . . . .	23
2.2 Graphene based pillar grating for optical absorber . . . . .	25
2.2.1 State of the art . . . . .	25
2.2.2 Design of the two-dimensional grating . . . . .	26
2.2.3 Numerical results . . . . .	26
2.2.4 Discussion . . . . .	32
2.3 Thermal tuning of resonant grating using phase change material . . . . .	33
2.3.1 State of the art . . . . .	33
2.3.2 Numerical model . . . . .	34
2.3.3 Numerical results . . . . .	35

2.3.4	Device fabrication . . . . .	40
2.3.5	Device characterization . . . . .	41
2.3.6	Discussion . . . . .	44
<b>3</b>	<b>Design of Plasmonic Gratings for Sensing and SERS Applications</b>	<b>45</b>
3.1	Introduction to plasmonics . . . . .	45
3.1.1	Surface plasmon polariton . . . . .	45
3.1.2	Excitation of surface plasmon . . . . .	47
3.2	FIB milled 2D array of plasmonic nanoplatelets . . . . .	48
3.2.1	Device fabrication and measurements . . . . .	49
3.2.2	Numerical Modelling . . . . .	50
3.2.3	Sensing performance . . . . .	53
3.3	Plasmonic nanostructures on curved surface . . . . .	55
3.3.1	State of the art and recent developments . . . . .	55
3.3.2	Segmented-wave analysis of plasmonic grating on a curved surface . . . . .	58
3.4	Spectrally tunable curved plasmonic grating on tapered optical fiber .	61
3.4.1	Grating emission spectra . . . . .	61
3.5	Surface Enhanced Raman Scattering (SERS) . . . . .	65
3.5.1	Curved plasmonic grating as a SERS platform . . . . .	66
3.5.2	EOT from a nanohole array on optical fiber facet . . . . .	71
<b>4</b>	<b>Conclusion</b>	<b>73</b>

# List of Figures

- 1.1 A plot of a typical Lorentz response with  $\omega_p = 2$ ,  $\omega_0 = 2$ , and  $\Gamma = 0.3$ . 7
- 1.2 Dielectric function  $\epsilon(\omega)$  of gold (solid lines) derived by the Drude model of equation (1.20) and fitted to the experimentally measured dielectric data for gold (dotted line). This model has limited validity at visible wavelengths. . . . . 8
- 1.3 Dielectric function  $\epsilon(\omega)$  of gold derived by Drude-Lorentz model (solid lines) of equation (1.30) using a single Lorentz oscillator and fitted to the experimentally measured dielectric data for gold (dotted line). The effect of changing the damping rate parameter is shown when its value is changed from (a) one time to (b) five times. . . . . 10
- 1.4 Refractive indices of the pure silica glass (a) and silicon nitride (b) show the data from the Sellmeier equation (solid line) fitted to the experimentally measured data (dots) at VIS-NIR wavelengths. . . . . 11
- 1.5 Real (bold) and imaginary (dashed) parts of the refractive index of a thin film of VO<sub>2</sub> at 30°C (insulator phase) and 30°C (metallic phase). . 14
- 1.6 A plot of the temperature-dependent dynamic complex refractive index of a thin film of VO<sub>2</sub> when the temperature is varied from 30°C to 100°C. The bold lines show the real and the dashed lines show the imaginary part of the refractive index. . . . . 15
- 2.1 A sketch of a diffraction grating having a period  $p$  placed on a slab waveguide. The refractive index of the waveguide layer  $n_2$  is greater than the refractive index of the cladding layer  $n_1$  and the substrate  $n_3$ . 23
- 2.2 (a) Sketch of a 2D graphene-based dielectric grating with an array of cylindrical nanopillars. (b) The cross-sectional (xz) view of the single period of the device used for simulations. . . . . 27
- 2.3 Optical reflectance (dashed blue line), the transmittance (dotted black line), and absorption (solid red line) spectra (a-b) without and (c-d) with graphene layer for both (a-c) TE and (b-d) TM plane waves at normal incidence. The device period  $p$ , waveguide Ta<sub>2</sub>O<sub>5</sub> thickness  $t_{Ta_2O_5}$ , and PMMA pillars height  $t_{PMMA}$  for this simulation result are set as 600nm, 150nm, and 600nm respectively. . . . . 28

2.4	Field profiles (a) amplitude of $E_y$ component and (b) amplitude of $E_x$ component at $0.9\mu m$ for the device parameters of Fig.2.2. The white lines show the device structure where the monolayer graphene is positioned at $z = 0.15\mu m$ (marked by the black line). (c-d) field profiles without the monolayer graphene. . . . .	28
2.5	Absorption spectra of the proposed structure under varying grating period for normally incident TE polarized plane wave. The waveguide $Ta_2O_5$ thickness $t_{Ta_2O_5}$ , and PMMA pillars height $t_{PMMA}$ are fixed at $150nm$ and $600nm$ respectively. . . . .	29
2.6	(a) Absorption map with respect to the variation of $Ta_2O_5$ layer thickness $t_{Ta_2O_5}$ under TE at normal illumination when the period $p$ and PMMA pillar height $t_{PMMA}$ are fixed at $600nm$ and $600nm$ respectively. (b) Absorption map under TE normal illumination, when PMMA pillar thickness $t_{PMMA}$ is varied from $300nm$ to $900nm$ . The period $p$ and waveguide $Ta_2O_5$ thickness $t_{Ta_2O_5}$ are fixed at $600nm$ and $150nm$ respectively. . . . .	30
2.7	Absorption maps of the device for varying incidence angle ( $0^\circ - 90^\circ$ ) under both TE and TM polarizations. For (a) and (b) device period $p$ , the waveguide $Ta_2O_5$ thickness $t_{Ta_2O_5}$ , and PMMA pillars height $t_{PMMA}$ are fixed at $450nm$ , $150nm$ , and $600nm$ respectively whereas for (c) and (d) the period $p$ is changed to $600nm$ . . . . .	31
2.8	Peak absorption wavelength when the incident angle is varied in range $0^\circ - 20^\circ$ . (a-b) The device period $p$ , the waveguide $Ta_2O_5$ thickness $t_{Ta_2O_5}$ , and PMMA pillars height $t_{PMMA}$ are fixed at $450nm$ , $150nm$ , and $600nm$ respectively. (c-d) The device period $p$ , the waveguide $Ta_2O_5$ thickness $t_{Ta_2O_5}$ , and PMMA pillars height $t_{PMMA}$ are fixed at $600nm$ , $150nm$ , and $600nm$ respectively. . . . .	31
2.9	Peak absorption wavelength of the device for varying incidence angle ( $70^\circ - 90^\circ$ ) under both TE and TM polarizations. The device period $p$ , the waveguide $Ta_2O_5$ thickness $t_{Ta_2O_5}$ , and PMMA pillars height $t_{PMMA}$ are fixed at $600nm$ , $150nm$ , and $600nm$ respectively. . . . .	32
2.10	(a) A sketch of an unpatterned semi-infinite ultra-thin $VO_2$ film on top of a glass substrate, (b) A sketch of an unpatterned semi-infinite $VO_2$ film on top of a $AlN/Cu$ bilayer supported by glass substrate, (c) A sketch of the periodic array of nano-pillars coated with an ultra-thin film of $VO_2$ . . . . .	35
2.11	Reflectance spectra from a semi-infinite ultra-thin ( $\lambda/60 = 10nm$ ) layer of $VO_2$ under normal incidence for the low temperature insulating (blue line) and high temperature metallic (dashed-dotted red line) phases as well as the absolute difference between the two (dashed black line). . . . .	36

- 2.12 (a) Map of the delta-reflectance spectra from an unpatterned semi-infinite structure shown in Fig.2.10(b) under normal incidence when the thickness of VO<sub>2</sub> film is changed from 10nm to 200nm. The thickness of AlN layer is fixed at 150nm. (b) Map of the delta-reflectance spectra from an unpatterned semi-infinite structure shown in Fig. 2.10(b) covered with a thin (150nm) film of VO<sub>2</sub> under normal incidence when the thickness of AlN layer is changed from 80 nm to 160 nm. (c) Line plots of the reflectance corresponding to the upper white line ( $t_{AlN} = 150nm$ ) in (b) showing the low temperature insulating (blue line) and high temperature metallic (dashed-dotted red line) phases as well as the absolute difference between the two (dotted black line). (d) As in (c) corresponding to the lower white line ( $t_{AlN} = 90nm$ ) in (b). 37
- 2.13 Reflectance spectra of a pillar grating coated with an ultra-thin (10nm) film of VO<sub>2</sub> under normal incidence for the low temperature insulating (blue line) and high temperature metallic (dashed-dotted red line) phases as well as the absolute difference between the two (dotted black line). The grating has a period of 750nm and AlN layer has a thickness of 150nm. (b) Same as in (a) for a grating that has a period of 670nm and AlN layer has a thickness of 90nm. . . . . 38
- 2.14 Electric and magnetic fields enhancement on resonance at 752nm for the configuration in Fig.2.10(c). . . . . 38
- 2.15 (a) Simulated delta-reflectance from an unpatterned semi-infinite structure (Fig.2.10(b)) covered with 150nm thick VO<sub>2</sub> film at VIS-NIR wavelengths for [0 – 90] degree incidence angle of the TM polarized incident light. (b) Same as in (a) for TE polarized incident light. (c) Simulated delta-reflectance spectra from grating covered with an ultra-thin (10nm) film of VO<sub>2</sub> at VIS-NIR wavelengths for [0 – 90] degree incidence angle of the TM polarized incident light. (d) Same as in (c) for TE polarized incident light. . . . . 39
- 2.16 Schematic diagram of the steps involved in the fabrication process of a VO<sub>2</sub> layer atop nanopillars. (b) Sputtering, (c) spin coating, (d-e-f) nanoimprint lithography and (g) VO<sub>2</sub> nanoparticles spin coating. . . . 40
- 2.17 (a) An SEM picture of the fabricated nanopillar grating taken before the spin-coating of VO<sub>2</sub> nano-powders [70] (b) An image of the pillar grating taken from the microscope objective. The black dots correspond to VO<sub>2</sub> nano-particle clusters. . . . . 41
- 2.18 An SEM picture of the nanopillar grating taken after the spin-coating of VO<sub>2</sub> nano-powder (a) at 10μm scale (b) at 5μm scale. . . . . 41
- 2.19 A sketch of the optical measurement setup. An optical image of the device as seen from the microscope (dots correspond to the VO<sub>2</sub> NP clusters) is shown in inset 1. Inset 2 shows the heater used in the setup for sample heating. . . . . 42

2.20	(a) Measured reflectance spectra of the device under a thermal stimulus at three different time instants when the temperature is increased from the room temperature ( $T < T_o$ ) to a value higher than the phase transition temperature of VO <sub>2</sub> ( $T > T_o$ ) and decreased back to the lower temperature. (b) The colormap of the change in the measured reflectance during a full measurement cycle of 6 minutes. . . . .	43
2.21	(a) Experimental reflectance from the grating at low temperature insulating phase ( $T < T_o$ ) and high temperature ( $T > T_o$ ) metallic phase. (b) Simulated reflectance from the grating at low temperature insulating phase ( $T < T_o$ ) and high temperature ( $T > T_o$ ) metallic phase. . . .	44
3.1	Sketch of a SPP propagation at a single interface between a metal and a dielectric. . . . .	46
3.2	(a) A sketch of the Kretschmann configuration for SPP coupling (b) A sketch of the Otto configuration for SPP coupling (c) A sketching showing phase-matching condition of light to SPP using a 1D grating. . . . .	48
3.3	Design of nanoplatelet array with a close-up of the tapered groove extending into the substrate. (b) An SEM picture of an array [17] with $P = 630nm$ . The inset shows a zoom on the nanoplatelets corner, with a gap width approaching $10nm$ . . . . .	49
3.4	(a) Nano-gap orientation in array $A_1$ and array $A_2$ , milled at period $P_A = 550nm$ with V-H and H-V order, respectively [17]. (b) Reflectance (black) and transmittance (red) spectra for $A_1$ (solid line) and $A_2$ (dashed line) for H-polarized light. (c) As in (b) for V-polarized light. (d) Nano-gap orientation in array $B_1$ and array $B_2$ , milled at period $P_B = 630nm$ with V-H and H-V groove order, respectively. (e) As in (b) for $B_1$ and $B_2$ arrays. (f) As in (c) for $B_1$ and $B_2$ arrays. . . . .	50
3.5	(a) 2D Sketch of the gold nanoplatelets grating (b) A sketch of a unit cell of the periodic array simulated as a periodic structure using RCWA and FDTD methods (c) A sketch of a finite subset of the periodic array simulated FDTD method. . . . .	51
3.6	Reflectance and transmittance spectra for device $B_1$ . . . . .	51
3.7	(a) Reflectance (black) and transmittance (red) spectra for infinite arrays of gold NPs, with periodicity $p = 630nm$ calculated with FDTD method. (b) FDTD simulation of reflectance (black) and transmittance (red) for a normally incident Gaussian beam pulse with a Gaussian spatial profile (TM polarization, centered at $600nm$ ) (c) As in b for $p = 550nm$ . (d-e-f) Effect of the variation of the illumination beam waist (d), of the array periodicity (e) and of the bottom gap size $w$ (f) on the reflectance spectrum. . . . .	53

3.8	(a) Simulated reflectance when a thin film of distilled water (blue line) or isopropyl alcohol (red line) covers the NP array. (b) Reflectance spectra measured with the array immersed in distilled water (blue dots) or IPA (red dots). (c) Dark field images of a NP array with periodicity $p = 550nm$ covered in air (top) or IPA (bottom). Scale bar is $15\mu m$ . (d) As in (a) for transmitted light (e) (d) As in (b) for transmitted light. . . . .	54
3.9	(a) A sketch of a continuous layer on a curved cylindrical substrate. (b) a 2D view of the geometry. (c) a 2D view with segmentation of the curved surface. . . . .	56
3.10	(a) Reflectance map for a $50nm$ gold as the light incident angle is varied from 0 to 70 degrees. (b) $\theta_{ofs}$ deduced when the background is air (37 degrees) and water (55 degrees). . . . .	57
3.11	(a) Reflectance spectra for a $30nm$ gold layer when the curvature radius is changed from $250\mu m$ to a flat surface. (b) same as (a) for $50nm$ gold layer (c) same as (a) for a $70nm$ gold layer. . . . .	58
3.12	A sketch of the gold nano-grating on a cylindrical glass substrate. . . . .	58
3.13	(a) A 2D view of the geometry (b) A 2D view with segmentation of the curved surface. . . . .	59
3.14	Transmittance spectra from segments when angle $\phi$ is varied in the xz plane. . . . .	60
3.15	Total transmittance spectra obtained by segmentation-based technique (solid line) and by the 3D FDTD curved model (dashed line). . . . .	60
3.16	(a) A sketch of a curved plasmonic grating on gold coated tapered optical fiber. The inset shows the grating on uniform cylindrical glass substrate assuming a slow varying taper (b) A sketch of the gold grating on a planar glass substrate showing diffracted orders in the transmission domain under an excitation from the glass substrate (c) A sketch of an array of nanoholes on the end facet of an optical fiber. The end facet is coated with a gold layer. . . . .	61
3.17	Maps of diffracted angles for transmitted orders at each wavelength and the angle of incidence (a) $0^{th}$ order (b) $1^{st}$ order (c) $-1^{st}$ order (d) $-2^{nd}$ order. The colour bar indicates the emission angles. . . . .	62
3.18	Maps of diffracted power for transmitted orders at each wavelength and the angle of incidence (a) $0^{th}$ order (b) $1^{st}$ order (c) $-1^{st}$ order (d) $-2^{nd}$ , respectively. . . . .	63
3.19	Emission spectra of the individual diffracted orders as function of the wavelength and emission angles (a) $0^{th}$ order (b) $1^{st}$ order (c) $-1^{st}$ order (d) $-2^{nd}$ . The considered range for emission angles is $[-50\ 50]$ degrees. . . . .	64

- 3.20 Emission spectra (dispersion diagram) of the grating as function of the wavelength and diffracted angles for three periodicities (a)  $630nm$  (b)  $700nm$  (c)  $750nm$ . . . . . 64
- 3.21 Spectrally tunable surface plasmon resonances on the curved fiber surface. (a) An SEM picture of the fabricated curved nanograting on a tapered optical fiber. (b) Diagram of the Fourier microscopy system used to measure the dispersion diagrams for curved nanograting at several periodicities. (c) Measured dispersion diagrams for curved nanograting milled with periodicities of  $630nm$ ,  $700nm$ , and  $750nm$  [111]. . . . . 65
- 3.22 The simulated Raman spectra of a thin layer (0.5 micron) of olive oil in transmission and reflection domains at an input field intensity of  $E = 1 \times 10^6 V/m$ . . . . . 67
- 3.23 (a) The simulated SERS spectra showing the Stoke signal at  $1441cm^{-1}$  ( $885nm$ ) in transmission and reflection domains when a thin layer of olive oil is placed on a planar gold grating (b) Same as in (a) showing the Stoke signal at  $2887cm^{-1}$  ( $1015nm$ ). A 2D FDTD model of gold grating is used to calculate these spectra. The grating has a period  $p = 600nm$ , width  $w = 100nm$  and the gold layer thickness is  $130nm$ . The input field intensity used is  $E = 5 \times 10^5 V/m$ . . . . . 67
- 3.24 The simulated SERS spectra showing the Stoke signal at  $1441cm^{-1}$  ( $885nm$ ) in transmission and reflection domains when a thin layer of olive oil is placed on a curved gold grating (a) The grating has a period  $p = 600nm$ , width  $w = 300nm$  and the gold layer thickness is  $100nm$  (b) The grating has a period  $p = 600nm$ , width  $w = 300nm$  and the gold layer thickness is  $130nm$  (c) The grating has a period  $p = 600nm$ , width  $w = 470nm$  and the gold layer thickness is  $100nm$  (d) The grating has a period  $p = 600nm$ , width  $w = 470nm$  and the gold layer thickness is  $130nm$ . A 3D FDTD model of gold grating is used to calculate these spectra. The input field intensity used is  $E = 1 \times 10^5 V/m$ . Apart from the targeted Stoke signal at  $1441cm^{-1}$  a second Stoke peak at  $2887cm^{-1}$  also appears in the spectra. . . . . 68
- 3.25 The simulated SERS spectra showing the Stoke signal at  $2887cm^{-1}$  ( $1015nm$ ) in transmission and reflection domains when a thin layer of olive oil is placed on a curved gold grating. The grating has a period  $p = 600nm$ , width  $w = 470nm$  and the gold layer thickness is  $130nm$ . A 3D FDTD model of gold grating is used to calculate these spectra. The input field intensity used is  $E = 1 \times 10^5 V/m$ . . . . . 69

- 3.26 (a) Electric field intensity profile of the curved grating in XZ plane at  $885\text{nm}$  when light is incident at an angle ( $\theta$ ) of  $60^\circ$  [111] (b) Electric field intensity profile of the curved grating in YZ plane at  $885\text{ nm}$  snapped at the center of the curved grating, (c) Same as in (b) snapped at the corner of the curved grating, (d) Same as in (a) at  $1015\text{nm}$ , (e) Same as in (b) at  $1015\text{nm}$ , (f) Same as in (c) at  $1015\text{nm}$ . . . . . 70
- 3.27 Plasmon-assisted spectroscopy with tapered optical fiber probe. (a) Sketch of the experimental measurement. The tapered optical fiber, immersed in olive oil, receives illumination from the back facet. The  $785\text{nm}$  light is emitted from the curved nanograting that, in turn, collects the Raman signal and couples it with the waveguide. (b) Raman spectra of olive oil collected with the tapered optical fiber (blue) and with a standard objective lens (green) around the  $1441\text{cm}^{-1}$  (top) and  $2800 - 3000\text{cm}^{-1}$  (bottom) bands. The intensity counts of the reference signals have been normalized to the tapered optical fiber measurements for the ease of comparison. nTF in the legend stands for the nano tapered fiber [111]. . . . . 71
- 3.28 Simulated transmittance through nanohole arrays at  $633\text{ nm}$ . . . . . 72
- 3.29 Near field image from a sub-section of a nanohole array showing sub-diffraction beam shaping. . . . . 72



# List of Tables

1.1	Values of the fitting parameters. . . . .	9
3.1	Measured geometrical parameters of the fabricated nanoplatelets arrays. . . . .	50
3.2	Simulated and experimental values of the sensitivity and FOM for both reflection and transmission domains. . . . .	54



This work is dedicated to my  
parents especially my father who  
worked very hard all his life to  
provide us with quality  
education.



## Chapter 1

# Introduction to Periodic Structures

Periodic structures have attracted huge research interest over the past many years due to their interesting electromagnetic properties. There are lots of useful applications in the fields of photonics and microwave engineering that come from periodic structures. Examples of periodic structures include diffraction gratings, photonic crystals, phased array antennas, frequency selective surfaces, and metamaterials [1].

A diffraction grating is composed of diffracting elements arranged periodically. The spacing between these elements is comparable to the wavelength of the incident light. The amplitude, or phase, or both, of the diffracted electromagnetic radiation from a diffraction grating, can be modified in a controlled and predictable manner. This is fundamentally possible due to the periodic variation of the refractive index near the surface of the grating [2]. Another interesting phenomenon is the presence of sharp resonant features in the optical spectra of the grating. The study of these resonance effects dates back more than 100 years by the work of Wood on optical gratings in 1902 [3]. The theoretical interpretation of these effects was given by Rayleigh [4] and Fano [5] in the later years. Many years later, Hessel and Oltiden [6] presented a complete interpretation of grating anomalies and divided them into two parts: one being the Wood's anomalies which correspond to the exchange of energy between the diffracted orders, and the second being the resonant-like anomalies which correspond to the guided mode in the grating or the waveguide coupled to the grating. This kind of resonant grating structures are termed as Guide-Mode Resonance (GMR) gratings and are also known with many different names such as leaky mode resonant gratings and resonant waveguide gratings. They can produce a variety of optical effects for example coupling, filtering, focusing, field enhancement and nonlinear effects. Moreover, their optical response can be modulated by tuning the optical parameters of the incident light source and/or the geometrical parameters of the structure as well as the material properties. GMR gratings have been employed in wide ranging applications including but not limited to sensors for biosensing, optical absorbers, efficient photodetectors and tunable filters for optical communication systems, reflection mirrors for lasers, and spectrometers [7], [8].

The first part of this work focuses on the design, fabrication, and characterization of resonant pillar gratings. This is further split into two parts. The first part describes the graphene-based pillar grating for optical absorber applications [9]. The

performance of the proposed periodic structure is investigated through numerical simulations. Simulations are carried out employing Rigorous Coupled Wave Analysis (RCWA) method. The proposed design exploits the guide mode resonances of the structure to achieve enhanced absorption in the monolayer graphene. In the second part, a phase change material vanadium-dioxide ( $\text{VO}_2$ ) is incorporated with the pillar grating structure to achieve the thermal tuning of the optical response exploiting the phase change properties of the  $\text{VO}_2$  [10]. The grating has been fabricated utilizing a nanoimprint lithography system exploiting a silicon mold (footprint of  $2.5 \times 2.5\text{mm}$  and  $900\text{nm}$  deep holes). Vanadium-oxide nano-powders have been deposited by spin-coating. In addition to the experimental tests, the proposed structure is simulated using the RCWA method.

Next, plasmonic grating structures on planar as well curved surfaces are designed and analyzed through numerical simulations for sensing and Surface Enhanced Raman Spectroscopy (SERS) applications. Plasmonic nanostructures support Surface Plasmon Resonance (SPR) and Localised Surface Plasmon Resonance (LSPR). The coupling of light into plasmonic modes requires momentum matching. Several techniques have been developed in this regard. One of the most common techniques to excite the SPP for sensing is the Kretschmann configuration [11]. However, this technique is only suitable for flat surfaces. Another common technique to excite SPRs is grating coupling. Periodic structures exhibit very narrow resonances due to the formation of leaky modes and can excite plasmonic modes without the need for complex arrangements based on prisms [12, 13]. Plasmonic modes exhibit unique properties such as nonradiative bound nature, extremely short wavelengths, strong near fields, and are highly sensitive to changes in the refractive index of the surrounding media. Based on this, they find applications in biosensing and spectroscopy [14, 15, 16]. The work related to plasmonic structures has also been further split into two parts. In the first part, a planar plasmonic grating (2D array of gold nanoplatelets) is designed and synthesized for sensing applications in the transmission domain exploiting Extraordinary Transmittance (EOT) properties of the plasmonic modes as well as the sensitivity of these modes to the changes in the refractive index of the surrounding media [17, 18]. An array of gold nanoplatelets has been fabricated on a glass substrate using a Focussed Ion Beam (FIB) milling system. A Finite Difference Time Domain (FDTD) model of the finite set of nanoplatelets has been developed to theoretically investigate and optimize the nanostructure as well as validate the experimental results. Plasmonic modes can concentrate light to much smaller locations creating field hotspots. This makes plasmonic structures a suitable platform for SERS. In the second part of the work, plasmonic gratings on planar and curved surfaces are investigated as SERS platforms. The rest of this thesis is organized as follows:

**Chapter 1:** A review of the state of the art topics covered in this thesis is presented. Basics of the electromagnetic properties of the materials are briefly explained. The dispersive analytical as well empirical models of the different materials used in

this work are covered. A brief description and background of the numerical methods used in this work are presented.

**Chapter 2:** Basic theory of diffraction gratings and GMR is briefly presented. This chapter covers the design, analysis, fabrication, and measurements of pillar gratings. In the first part, graphene-based pillar gratings are detailed for optical absorber applications. The second part of this chapter explains the design, fabrication, and measurement of VO<sub>2</sub> based pillar gratings.

**Chapter 3:** A brief theoretical background of the SPR is provided. Details on the design and analysis of plasmonic nanostructures on planar as well as curved surfaces for sensing and SERS applications are provided. The first part covers the numerical modeling of a finite subset of gold nanoplatelets fabricated through FIB milling. In the second part, nonlinear simulation models of plasmonic gratings are explained for SERS applications.

**Chapter 4:** The main outcomes of this research work are summarised.

## 1.1 Dielectric function of materials

Classically, the optical and dispersive properties of the materials are described by a complex dielectric function. Along with the experimental techniques to measure the complex dielectric function of the materials, several analytical models have also been developed over the years to theoretically calculate the material properties at the diverse range of electromagnetic radiations. In the following, after introducing the complex dielectric function of materials through Maxwell's equations, Lorentz and Drude models for metals are elaborated as these are the most used models, especially for metals. A brief introduction of another material model called the Sellmeier equation is also presented.

Like any of the electromagnetic phenomena, Maxwell's equations are taken as starting point to study the electromagnetic response of the metals.

$$\nabla \cdot \mathbf{D} = \rho_v \quad (1.1)$$

$$\nabla \cdot \mathbf{B} = 0 \quad (1.2)$$

$$\nabla \times \mathbf{E} = -\frac{\partial \mathbf{B}}{\partial t} \quad (1.3)$$

$$\nabla \times \mathbf{H} = \mathbf{J} + \frac{\partial \mathbf{D}}{\partial t} \quad (1.4)$$

These equations describe the relation among electromagnetic fields, electric field  $\mathbf{E}$ , magnetic field  $\mathbf{B}$ , dielectric displacement  $\mathbf{D}$  and magnetic induction  $\mathbf{H}$ , the charge density  $\rho_v$ , and current density  $\mathbf{J}$ . However, Maxwell's equations do not directly describe how the fields interact with materials. Two more fields called polarization  $\mathbf{P}$  and magnetization  $\mathbf{M}$  are linked to other fields by:

$$\mathbf{D} = \varepsilon_0 \mathbf{E} + \mathbf{P} \quad (1.5)$$

$$\mathbf{H} = \frac{1}{\mu_0} \mathbf{B} + \mathbf{M} \quad (1.6)$$

where  $\varepsilon_0$  and  $\mu_0$  are the electric permittivity and magnetic permeability of the free space, respectively.  $\mathbf{P}$  describes the electric dipole moment per unit volume inside the material. It is related to charge density via  $\nabla \cdot \mathbf{P} = -\rho$ . Further, the relation between internal charge and current densities results in:

$$\mathbf{J} = \frac{\partial \mathbf{P}}{\partial t}. \quad (1.7)$$

It is worth noting that  $\mathbf{M}$  can be neglected for a non-magnetic response.

The constitutive relations given below describe the interaction of fields with materials via linear relations. These equations contain the fundamental parameters of relative electric permittivity  $\varepsilon$ , relative magnetic permeability  $\mu$ , and electrical conductivity  $\sigma$ . The relative magnetic permeability  $\mu$  is 1 for nonmagnetic materials.

$$\mathbf{D} = \varepsilon_0 \varepsilon \mathbf{E} \quad (1.8)$$

$$\mathbf{B} = \mu_0 \mu \mathbf{H} \quad (1.9)$$

$$\mathbf{J} = \sigma \mathbf{E} \quad (1.10)$$

The constitutive relations describe above are valid for linear and isotropic materials only where these properties are independent of the direction and strength of the fields. The linear relation (1.8) between  $\mathbf{D}$  and  $\mathbf{E}$  is often also implicitly defined in terms of the dielectric susceptibility  $\chi$  which describes the linear relation between  $\mathbf{P}$  and  $\mathbf{E}$  by:

$$\mathbf{P} = \varepsilon_0 \chi \mathbf{E}. \quad (1.11)$$

Considering the dispersion in time and space the linear constitutive relations can be generalized as follows:

$$\mathbf{D}(\mathbf{r}, t) = \varepsilon_0 \int dt' d\mathbf{r}' \varepsilon(\mathbf{r} - \mathbf{r}', t - t') \mathbf{E}(\mathbf{r}', t') \quad (1.12)$$

$$\mathbf{J}(\mathbf{r}, t) = \varepsilon_0 \int dt' d\mathbf{r}' \sigma(\mathbf{r} - \mathbf{r}', t - t') \mathbf{E}(\mathbf{r}', t'). \quad (1.13)$$

These equations can be significantly simplified to get constitutive relations in the Fourier domain.

$$\mathbf{D}(\mathbf{K}, \omega) = \varepsilon_0 \varepsilon(\mathbf{K}, \omega) \mathbf{E}(\mathbf{K}, \omega) \quad (1.14)$$

$$\mathbf{J}(\mathbf{K}, \omega) = \sigma(\mathbf{K}, \omega) \mathbf{E}(\mathbf{K}, \omega) \quad (1.15)$$

Using equations (1.5), (1.7), and (1.14), a fundamental relation between the electric permittivity and the conductivity is found. The electromagnetic phenomenon of metals can be described using either of these fundamental quantities. However, historically, conductivity is a preferred choice at microwave frequencies whereas permittivity also referred to as the dielectric function is used at optical frequencies. These are related as following:

$$\varepsilon(K, \omega) = 1 + j \frac{\sigma(K, \omega)}{\varepsilon_0 \omega}. \quad (1.16)$$

This works deals with devices at optical frequencies, so from now on wards only dielectric function  $\varepsilon$  will be considered. The equation (1.16) can further be simplified to the limit of a spatial local response  $\varepsilon(K = 0, \omega) = \varepsilon(\omega)$ . In general,  $\varepsilon$  is complex valued function  $\varepsilon(\omega) = \varepsilon_1(\omega) + j\varepsilon_2(\omega)$ . The complex refractive index of a material can be determined from the dielectric function as follows:

$$\bar{n}(\omega) = n(\omega) + j\kappa(\omega) = \sqrt{\varepsilon(\omega)}. \quad (1.17)$$

The real part  $n$  of the refractive index quantifies the lowering of the phase velocity of the propagating waves while the imaginary part  $\kappa$ , called the extinction coefficient, determines the optical absorption of electromagnetic waves propagating through the medium [19].

### 1.1.1 Lorentz model for metals

The optical properties of the metals, as well as dielectrics, can be modeled by a Lorentz oscillator model. It is based on the motion of electron plasma against a fixed background of positive ions core. It assumes electron oscillations in response to the applied electromagnetic field like a mass-spring system. Just like a classical harmonic oscillator, an equation of motion for an electron considering both free-electron plasma and bound electrons subjected to an external electric field  $\mathbf{E}$  can be written as:

$$m \frac{\partial^2 r}{\partial t^2} + m\gamma \frac{\partial r}{\partial t} + m\omega_0^2 r = -qE \quad (1.18)$$

where  $m$  and  $q$  are the mass and charge of an electron, respectively,  $\gamma$  is the damping rate, and  $\omega_0$  is the natural frequency. By taking the Fourier transform and after simplification, the displacement  $r(\omega)$  can be described as:

$$r(\omega) = -\frac{q}{E} \frac{E(\omega)}{m\omega_0^2 - \omega^2 - j\omega\gamma}. \quad (1.19)$$

It tells how far a charge is displaced from its equilibrium position. The displacement of electrons is in turn a measure of dipole moment which contributes to the polarization of material. From this average polarization of all atoms in a material

considering  $N$  as electron density which is the number of electrons per unit volume can be written as:

$$\mathbf{P}(\omega) = -\frac{Nq^2}{m} \frac{\mathbf{E}(\omega)}{m\omega_0^2 - \omega^2 - j\omega\gamma} \quad (1.20)$$

Since

$$\mathbf{P}(\omega) = \varepsilon_0 \chi(\omega) \mathbf{E}(\omega). \quad (1.21)$$

This leads to an equation for electric susceptibility as:

$$\chi(\omega) = \frac{\omega_p^2}{m\omega_0^2 - \omega^2 - j\omega\gamma} \quad (1.22)$$

where  $\omega_p^2 = \left(\frac{nq^2}{\varepsilon_0 m}\right)$  is called the plasma frequency. Inserting equation (1.11) into equation (1.8) yields:

$$\mathbf{D}(\omega) = \varepsilon_0 (1 + \chi(\omega)) \mathbf{E}(\omega). \quad (1.23)$$

By comparing the above expression with the equation (1.8), the dielectric function can be written in terms of electric susceptibility as follows:

$$\varepsilon(\omega) = 1 + \chi(\omega). \quad (1.24)$$

Using the electric susceptibility derived by using the Lorentz oscillator from equation (1.22), the final expression for the complex dielectric functions comes out as:

$$\varepsilon(\omega) = 1 + \frac{\omega_p^2}{m\omega_0^2 - \omega^2 - j\omega\gamma}. \quad (1.25)$$

The dielectric function described by (1.25) is known as the Lorentz model of the optical response of metals. This dielectric function has only one resonance whereas in the case of real materials there can be multiple resonances. A typical Lorentz response is plotted in Fig.1.1. It can be noticed that the response is dispersive. The imaginary part is very high near the resonance which means higher losses. Far from the resonance, the value of the imaginary part is low. The bandwidth of the resonance is determined by the damping rate. At much higher frequencies, the real part approaches unity with negligible imaginary part giving the material vacuum characteristics.

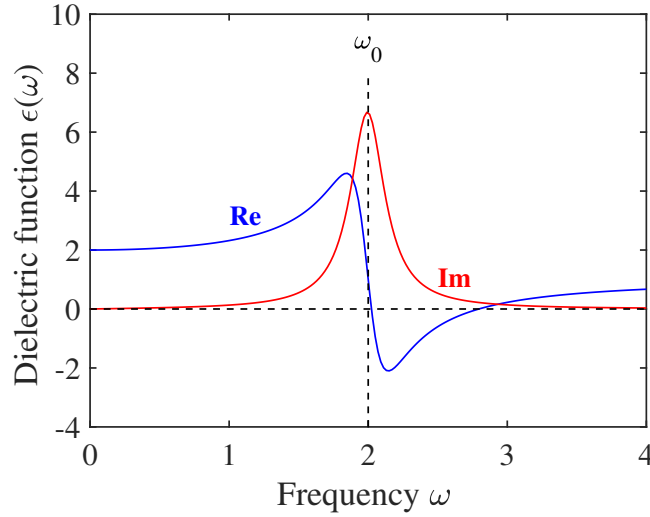


FIGURE 1.1: A plot of a typical Lorentz response with  $\omega_p = 2$ ,  $\omega_0 = 2$ , and  $\Gamma = 0.3$ .

### 1.1.2 Drude model for metals

The Drude model is a special case of the Lorentz model. In metals, the majority is of free electrons. For this reason, the contribution from bound electrons can be neglected which implies the restoring force is negligible and there is no natural frequency  $\omega_0$ . This leads to a simple expression given as follows:

$$\varepsilon(\omega) = 1 - \frac{\omega_p^2}{\omega^2 - j\omega\gamma}. \quad (1.26)$$

The motion of free electrons is damped via collisions occurring with a characteristic collision frequency  $\gamma = 1/\tau$ . The parameter  $\tau$  is known as the relaxation time of the free electron gas, which is typically on the order of  $10^{-14}$ s at room temperature, corresponding to  $\gamma = 100$ THz. The ideal metals behave like a free electron gas which means no damping as  $\tau$  approaches infinity resulting in only real-valued dielectric function which attains a value of unity for  $\omega \gg \omega_p$  as follows:

$$\varepsilon(\omega) = 1 - \frac{\omega_p^2}{\omega^2}. \quad (1.27)$$

For real metals, a correction term  $P_\infty = \varepsilon_0(\varepsilon_\infty - 1)E$  is added to account for d-band electrons polarization in equation (1.26). The dielectric function becomes:

$$\varepsilon(\omega) = \varepsilon_\infty - \frac{\omega_p^2}{\omega^2 + j\omega\gamma} \quad (1.28)$$

where the dielectric constant  $\varepsilon_\infty$  usually is in the range  $1 \leq \varepsilon_\infty \leq 10$ . The Drude model is valid for microwave and radio frequencies where  $\omega < \omega_p$ . In the case of metals, the optical response is correctly described up to the interband transition threshold. For example, for gold, the Drude model is valid for up to  $600$ nm. A plot of

the Drude model for gold fitted to the experimentally measured gold data is shown in Fig.1.2.

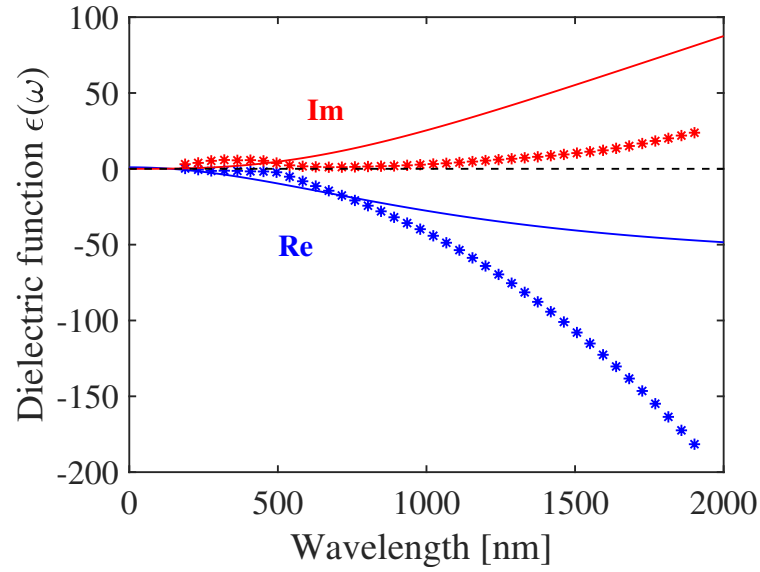


FIGURE 1.2: Dielectric function  $\epsilon(\omega)$  of gold (solid lines) derived by the Drude model of equation (1.20) and fitted to the experimentally measured dielectric data for gold (dotted line). This model has limited validity at visible wavelengths.

### 1.1.3 Drude-Lorentz model

Drude and Lorentz models can be combined to account for both the intraband (Drude model) and interband (Lorentz model) electron transitions. It eliminates the problem of the imaginary part of the dielectric function approaching zero at higher frequencies as described in the previous section. Several Lorentz terms with the individual resonant frequency of each interband transition are expanded for best fit to the experimental data. The resulting dielectric function is given as:

$$\epsilon(\omega) = \epsilon_{\infty} - \frac{\omega_p^2}{\omega^2 + j\omega\gamma} + \sum_{k=1}^N \frac{A_k \omega_k^2}{\omega_k^2 - \omega^2 - j\omega\gamma_k}. \quad (1.29)$$

The main advantage of having analytical formulae for the dielectric function is that they can be easily incorporated into numerical simulation software packages. For example, the finite-difference time-domain (FDTD) requires an analytical model of materials including dispersion to produce a broadband result in a single run.

The dielectric data usually retrieved from experimental data handbooks available in the literature [20, 21] is mostly for bulk materials. However, thin films of materials ranging from a few tens to hundreds of nano-meters are used for plasmonic and photonic devices. It has been reported in a recent experimental study [22] that the dielectric function of the metals is determined by their structural morphology and is strongly dependent upon the film thickness. Since the imaginary part of the

TABLE 1.1: Values of the fitting parameters.

Parameter	Value
$\varepsilon_\infty$	6.155991
$\gamma_D(\text{rad/s})$	$1.66938 \times 10^{15}$
$\omega_D(\text{rad/s})$	$1.34759 \times 10^{16}$
$\Delta\varepsilon$	2.07122
$\omega_L(\text{rad/s})$	$4.66171 \times 10^{15}$
$\gamma_L(\text{rad/s})$	$7.20958 \times 10^{13}$

dielectric function is responsible for optical losses in metals, the procedure described in [22] is used to adjust a fitting parameter called damping rate (or scattering loss) to analyze the influence of film thickness on the optical absorption. The scattering loss parameter can further be tuned as one, two, and three times that of initial value to account for optical losses by thin gold films [23]. The Drude-Lorentz model proposed in [24] is used. The model is described by equation (1.30) where  $\gamma_D$  and  $\gamma_L$  are damping coefficients,  $\omega_p$  is the plasma angular frequency,  $\omega_L$  is the resonance frequency of the Lorentz oscillator,  $\delta\varepsilon$  is oscillator strength and  $\varepsilon_\infty$  is the relative permittivity for high frequencies.

$$\varepsilon_{DL}(\omega) = \varepsilon_\infty - \frac{\omega_p^2}{\omega(\omega + j\gamma_D)} - \frac{\delta\varepsilon\omega_L^2}{\omega^2 - \omega_L^2 + j\gamma_L\omega} \quad (1.30)$$

Values of the different parameters taken from [24] are shown in Table.1.1 below. The value of damping rate  $\gamma$  can be adjusted to match the thickness of the samples. The resulting dielectric function of the gold is fitted against the experimentally measured data for gold as shown in Fig.1.3. The effect of the tuning of the damping rate parameter is also demonstrated.

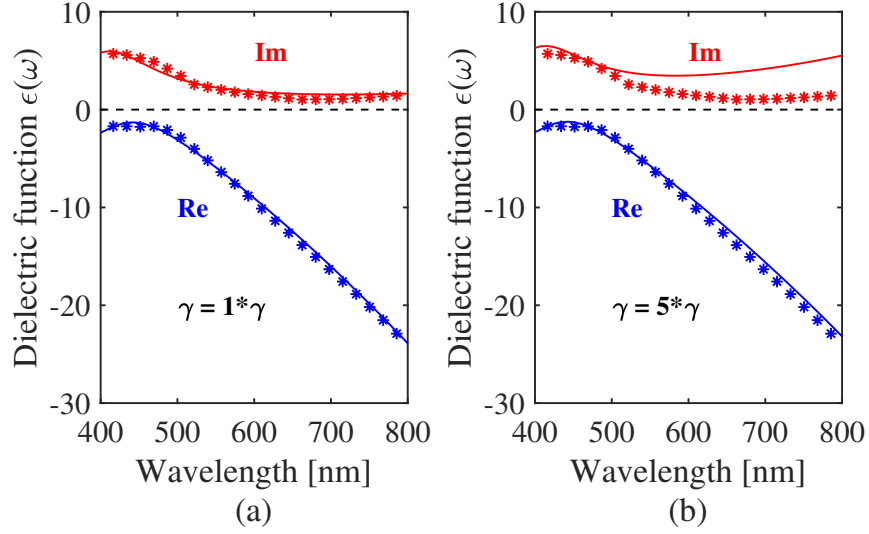


FIGURE 1.3: Dielectric function  $\epsilon(\omega)$  of gold derived by Drude-Lorentz model (solid lines) of equation (1.30) using a single Lorentz oscillator and fitted to the experimentally measured dielectric data for gold (dotted line). The effect of changing the damping rate parameter is shown when its value is changed from (a) one time to (b) five times.

### 1.1.4 Sellmeier equation

Sellmeier equation is an empirical formula that describes the relationship between the refractive index and wavelength particularly for the transparent media. It is based on Cauchy's work on the modeling of dispersion. The Sellmeier equation in its general form is written as:

$$n^2(\lambda) = 1 + \sum_{i=1}^N \frac{B_i \lambda^2}{\lambda^2 - C_i^2} \quad (1.31)$$

where  $B_i$  and  $C_i$  are experimentally determined Sellmeier coefficients.  $B_i$  represents the strength of  $i^{\text{th}}$  resonance at the  $C_i$  wavelength. Refractive indices of pure silica glass and silicon nitride ( $\text{Si}_3\text{N}_4$ ) are plotted in Fig.1.4 showing the data calculated by the Sellmeier equation (1.31) fitted to the measured points (red dots). The Sellmeier coefficients for glass used are  $B_1 = 0.6961663$ ,  $B_2 = 0.4079426$ ,  $B_3 = 0.8974794$ ,  $C_1 = 0.0684043\mu\text{m}$ ,  $C_2 = 0.1162414\mu\text{m}$  and,  $C_3 = 9.896161\mu\text{m}$  which are adopted from [25]. For silicon nitride, the coefficients are taken from [26]. The values are  $B_1 = 3.0249$ ,  $B_2 = 40314$ ,  $C_1 = 0.1353406\mu\text{m}$  and,  $C_2 = 1239.842\mu\text{m}$ .

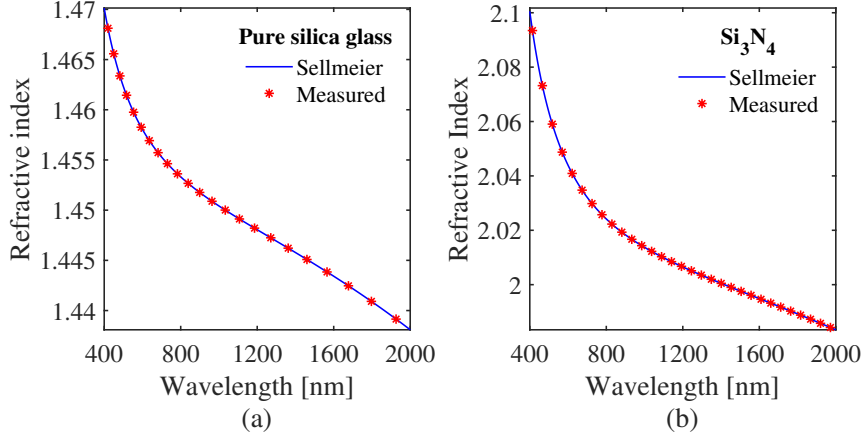


FIGURE 1.4: Refractive indices of the pure silica glass (a) and silicon nitride (b) show the data from the Sellmeier equation (solid line) fitted to the experimentally measured data (dots) at VIS-NIR wavelengths.

### 1.1.5 Nonlinear properties of materials

Equation (1.11) describes the linear relation between  $\mathbf{P}$  and  $\mathbf{E}$ . In general, this relation is nonlinear and is dependent upon the strength of the fields. The complete relation can be expressed as a polynomial [27] as following:

$$\mathbf{P} = \varepsilon_0 \chi^{(1)} \mathbf{E} + \varepsilon_0 \chi^{(2)} \mathbf{E}^2 + \varepsilon_0 \chi^{(3)} \mathbf{E}^2 + \dots \quad (1.32)$$

where  $\chi^{(1)}$ ,  $\chi^{(2)}$ , and  $\chi^{(3)}$  are first, second, and third-order electric susceptibilities. The second and third-order nonlinear susceptibilities are responsible for distinct physical processes. The third-order electric susceptibility ( $\chi^{(3)}$ ) is used to model Kerr and Raman interactions. It has units of  $\frac{m^2}{V^2}$ . The dispersive  $\chi^{(3)}$  can be described as a Lorentz like oscillator as follows:

$$\chi^{(3)}(\omega) = \alpha \chi_0^{(3)} + (1 - \alpha) \frac{\chi_0^{(3)} \omega_{RAMAN}}{\omega_{RAMAN}^2 - 2j\delta\omega - \omega^2} \quad (1.33)$$

where  $\alpha$  is a splitting parameter that splits the third-order nonlinearity into Kerr and Raman effects and sets the relative strength of each interaction,  $\omega_{RAMAN}$  is the Raman resonance frequency and  $\chi_0^{(3)}$  is the third-order electric susceptibility of the material.  $\delta$  is the damping factor that controls the line width of the resonance. Equation (1.33) shows a single resonance. A linear sum of multiple resonances can also be used as described in (1.29).

The total refractive index of material has both linear and nonlinear terms and is written as follows:

$$n = n_0 + n_2 I \quad (1.34)$$

where  $n_0$  is the linear refractive index,  $n_2$  is the nonlinear refractive index and  $I$  is the intensity of the light beam. The nonlinear refractive index  $n_2$  is dependent upon the  $\chi^{(3)}$  and its relation is given as:

$$n_2 = \frac{3\chi^{(3)}}{4n_0^2} Z_0 \quad (1.35)$$

where  $Z_0$  is the free space impedance.  $n_2$  has a unit of  $\frac{m^2}{W}$ .

Generally, all materials are nonlinear. However, some have stronger nonlinear responses than others. A very intense electric field is required to excite nonlinear behavior. Nonlinear properties are commonly exploited at optical frequencies. At microwave frequencies, materials undergo a breakdown before the nonlinear effects can be observed. Nonlinear materials have numerous applications for example second harmonic generation, frequency mixing, third-harmonic generation, and Raman spectroscopy.

## 1.2 Graphene

Graphene is a two-dimensional material consisting of a single layer of carbon atoms arranged in a honeycomb lattice. Over recent years it has emerged as an attractive two-dimensional material due to its exceptional mechanical, electrical, and optical properties. K.S. Novoselov et. al. were able to fabricate an ultra-thin layer of graphene in 2004 in their pioneering work for which they were awarded the Nobel Prize in Physics in 2010 [28]. Since then, it has attracted significant scientific activity for the research and development of graphene-based electronic and optical devices. Monolayer graphene exhibits superior thermodynamic characteristics compared to atomically thin metal films and supports variation in charge concentration under electric field effect which makes it suitable for the development of nanoelectronics devices. In the optical domain, it is suitable for applications in sensors, photodetectors, and meta-surfaces, etc.

Several different material models of graphene are being used for the simulation of graphene-based devices. This includes the conventional permittivity model [29] and surface conductivity model of graphene [30, 31]. The conductivity of graphene is expressed by the Kubo formula as:

$$\sigma(\omega, \mu_c, \Gamma, T) = \frac{je^2(\omega - j2\Gamma)}{\pi\hbar^2} \left[ \frac{1}{(\omega - j2\Gamma)^2} \int_0^\infty \epsilon \left( \frac{\partial f_d(\epsilon)}{\partial \epsilon} - \frac{\partial f_d(-\epsilon)}{\partial \epsilon} \right) d\epsilon - \int_0^\infty \frac{f_d(-\epsilon) - f_d(\epsilon)}{(\omega - j2\Gamma)^2 - 4(\epsilon/\hbar)^2} d\epsilon \right] \quad (1.36)$$

where  $\omega$  is the angular frequency,  $\mu_c$  is chemical potential,  $\Gamma$  is scattering rate,  $T$  is temperature,  $e$  is the electron charge,  $\hbar$  is the reduced Planck's constant, and  $f_d(\epsilon)$  is the Fermi-Dirac distribution. The expression in equation (1.36) includes both intra-band and interband transitions.

In [29], a simple method is presented to derive an approximate dielectric function of graphene at visible wavelengths. The results are consistent with the experimental spectra. The obtained dielectric function can accurately describe graphene

behavior for various thicknesses of graphene starting from monolayer graphene to bulk graphite. The general equation for the light propagation through an absorbing medium is given as:

$$\frac{4\pi k}{\lambda} = -\frac{1}{nd} \ln \left[ \frac{I}{I_0} \frac{1}{1-R} \right] \quad (1.37)$$

where  $n$  is the real part of the refractive index,  $k$  is extinction coefficient,  $d$  is thickness,  $\lambda$  is the wavelength,  $R$  is the reflected light, and  $I$  and  $I_0$  are the transmitted and incident light intensities, respectively. At visible wavelengths, (1.37) is approximated for a single layer of graphene considering  $R = 0$  and  $I/I_0 \sim (1 - \pi\alpha)$ . The resultant equation is written as:

$$k = -\frac{\lambda}{4\pi nd} \ln [1 - \pi\alpha] = L_1 \frac{\lambda}{n}. \quad (1.38)$$

For monolayer graphene, thickness  $d = 0.34nm$  which gives  $L_1 = 5.446\mu m^{-1}$ . The real part of the refractive index  $n$  is considered a constant. This is a reasonable approximation since the real part of the refractive index of graphite does not have sharp resonances at visible wavelengths. The value of  $n$  is chosen to best fit the measured spectra. Then the value of the imaginary part of the refractive index  $k$  is obtained from equation (1.38). For bulk graphite, the best fit gives a value of 3 for  $n$ .

### 1.3 Vanadium dioxide (VO<sub>2</sub>)

Phase change materials are currently receiving great attention for the development of tunable photonic devices. The phase transition can be controlled externally by temperature, electrical, or an optical signal. This results in drastic changes in the electrical and optical properties of the material. The ability to dynamically change the physical characteristics of the material can open up new possibilities for the design and fabrication of electrical and optical devices whose response can be dynamically controlled and modulated. Vanadium dioxide (VO<sub>2</sub>) is one of the most promising phase change materials. It undergoes reasonably large changes in the refractive index under a low-intensity stimulus. The insulator to a metal phase transition happens at a temperature of 68°C which is easily attainable under ordinary circumstances. The phase transition of VO<sub>2</sub> is reversible once the external stimulus is removed and it can withstand millions of cycles [32]. Moreover, the phase transition is achievable over a broadband range of optical wavelengths from visible to infrared.

Under phase transition conditions, there is a structural change inside the material from a monoclinic insulator phase to a tetragonal metallic phase. This results in changes in the electrical and optical properties of the material. The measured complex refractive index of vanadium dioxide used in this work is plotted in Fig.1.5 at visible and near-infrared wavelengths. The plot shows refractive index data at two different temperatures, 30°C and 100°C which corresponds to an insulator and a

metallic phase of the material, respectively. The experimentally measured refractive index data for a thin film of VO<sub>2</sub> is taken from [33].

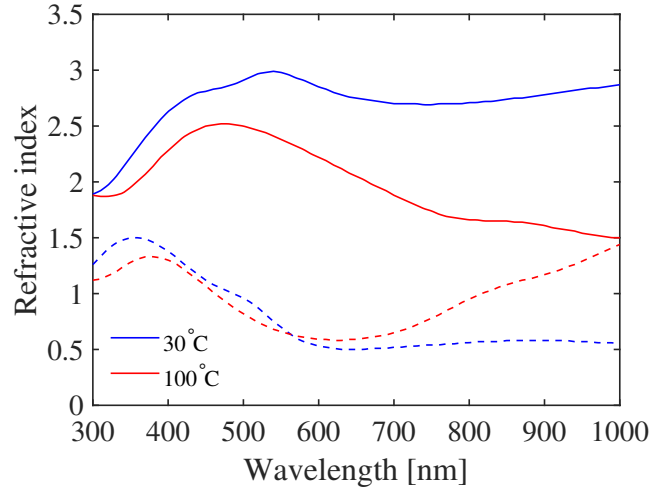


FIGURE 1.5: Real (bold) and imaginary (dashed) parts of the refractive index of a thin film of VO<sub>2</sub> at 30°C (insulator phase) and 100°C (metallic phase).

For tunability where it is needed to dynamically change the refractive index of the VO<sub>2</sub> over a given temperature range, the intermediate refractive index data can be approximated using effective medium theories. Using a simpler Looyenga rule refractive indices of VO<sub>2</sub> can be approximated as in equation (1.39). Temperature-dependent  $F$  can be expressed in equation (1.40) where  $k_B$  is Boltzmann constant,  $w$  is the width of temperature range and  $T_{half}$  is the temperature at which half of the film volume is in the metallic state. The resulting complex refractive index of VO<sub>2</sub> over a temperature range of [30 – 100]°C is shown in Fig.1.6.

$$\epsilon_{eff}^s = (1 - F)\epsilon_i^s + F\epsilon_m^s \quad (1.39)$$

$$F(T) = \frac{1}{1 + \exp\left[\frac{w}{k_b}\left(\frac{1}{T} - \frac{1}{T_{half}}\right)\right]} \quad (1.40)$$

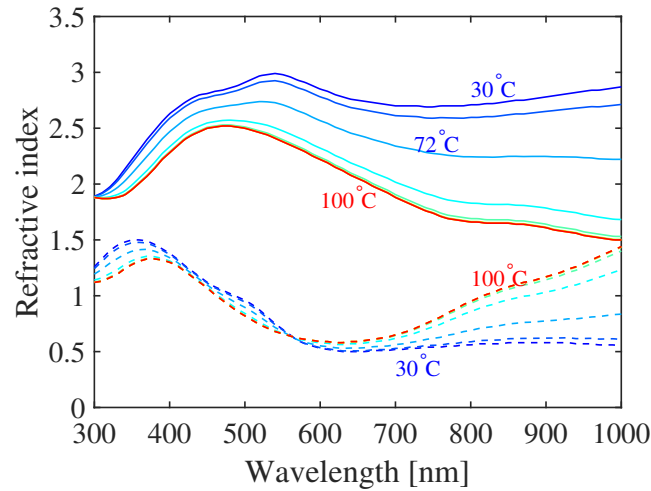


FIGURE 1.6: A plot of the temperature-dependent dynamic complex refractive index of a thin film of  $\text{VO}_2$  when the temperature is varied from  $30^\circ\text{C}$  to  $100^\circ\text{C}$ . The bold lines show the real and the dashed lines show the imaginary part of the refractive index.

## 1.4 Numerical methods in electromagnetics

In this work, three different numerical techniques namely Finite Difference Time Domain (FDTD) method, Rigorous Coupled Wave Analysis (RCWA) method, and Beam Propagation Method (BPM) have been used for the investigations and analysis of photonic structures composed of finite and infinite periodic structures having dielectric as well as metallic components. A brief description of the technical background of these methods is given below.

### 1.4.1 Finite Difference Time Domain (FDTD) method

The FDTD method is based on the rigorous solution of Maxwell's equations. It is a widely used method for the solution of electromagnetic problems such as scattering from metallic and dielectric objects and antennas. The technique was first developed by K. Yee in 1934 and then improved by others in the early 70s. It is simple to implement and suitable for broadband simulations. It is also applicable for nonlinear problems. Being a time-domain method, it is excellent for field visualization. However, it is a computationally expensive method and requires a large amount of memory, computational power, and time. FDTD is basically a time-domain method, but frequency analysis is also possible using the Fast Fourier Transform (FFT) and the Discrete Fourier Transform (DFT). A book by Taflove and Hagness [34] is a definitive reference on this subject. Several other books and numerous commercial software packages that implement FDTD algorithms are also available [35, 36, 37]. A commercial FDTD package by RSoft called FullWAVE has been used for simulations in this work.

The general formulation of the method is based on Maxwell's curl equations (1.3) and (1.4). Assuming no flow of currents ( $\mathbf{J} = 0$ ) and no free charges ( $\rho = 0$ ), these equations can be expanded in cartesian coordinates for the lossless case as:

$$\begin{aligned}
\varepsilon_0 \frac{\partial E_x}{\partial t} &= \frac{\partial H_z}{\partial y} - \frac{\partial H_y}{\partial z} \\
-\varepsilon_0 \frac{\partial E_y}{\partial t} &= \frac{\partial H_z}{\partial x} - \frac{\partial H_x}{\partial z} \\
\varepsilon_0 \frac{\partial E_z}{\partial t} &= \frac{\partial H_y}{\partial x} - \frac{\partial H_x}{\partial y} \\
-\mu_0 \frac{\partial H_x}{\partial t} &= \frac{\partial E_z}{\partial y} - \frac{\partial E_y}{\partial z} \\
\mu_0 \frac{\partial H_y}{\partial t} &= \frac{\partial E_z}{\partial x} - \frac{\partial E_x}{\partial z} \\
-\mu_0 \frac{\partial H_z}{\partial t} &= \frac{\partial E_y}{\partial x} - \frac{\partial E_x}{\partial y}.
\end{aligned} \tag{1.41}$$

Based on the Yee method, the above equations are solved by first discretizing the equations via central differences in time and space as in equation (1.42) written for  $E_x$ , and then numerically solving these equations in software.

$$\frac{(E_x)_i^{(n+1/2)} - (E_x)_i^{(n-1/2)}}{\Delta t} = \frac{1}{\varepsilon_0} \frac{(H_z)_{(i+1/2)}^n - (H_z)_{(i-1/2)}^n}{\Delta y} - \frac{1}{\varepsilon_0} \frac{(H_y)_{(i+1/2)}^n - (H_y)_{(i-1/2)}^n}{\Delta z} \tag{1.42}$$

Update equation (1.43) is obtained by solving the difference equations which express unknown fields (future) in terms of known fields (past). These steps are repeated until the fields are obtained over the desired duration.

$$E_{t+\Delta t} = E_t + \frac{\Delta t}{\varepsilon} (\nabla \times H_{t+\Delta t/2}) \tag{1.43}$$

Along with Maxwell's curl equations, the constitutive relations (1.8) and (1.9) are used to get  $\mathbf{E}$  and  $\mathbf{H}$  fields from  $\mathbf{D}$  and  $\mathbf{B}$  fields and to include losses and the material dispersion in the calculations.

An initial launch field can be expressed as (1.44) having both a spatial and temporal component. A variety of different excitation schemes can be used for example a continuous wave, a Gaussian pulse, or an impulse function.

$$\phi_L(\mathbf{r}, t) = f(\mathbf{r}_0) g(t) \tag{1.44}$$

Additional numerical simulation parameters are required in the FDTD algorithm. This includes a finite simulation domain, the boundary condition(s), the spatial grid sizes, a time step, and total simulation time. Choice of these parameters is important as it can affect the accuracy of the results and the stability of the simulation. Perfectly matched layer (PML) and periodic boundary conditions are supported in the

FDTD method to simulate finite as well as infinite periodic structures. The spatial grid sizes ( $\Delta x$ ,  $\Delta y$ , and  $\Delta z$ ) should be small enough to resolve the smallest features of the fields. However, grid sizes must be chosen wisely for an accurate and efficient simulation. A rule of thumb is to set the grid sizes as  $\lambda/10$  at least where  $\lambda$  is the wavelength in the material. Time step affects the stability of the simulation. For a stable simulation, the Courant condition (1.45) must be followed:

$$c\Delta t < \frac{1}{\sqrt{\frac{1}{\Delta x^2} + \frac{1}{\Delta y^2} + \frac{1}{\Delta z^2}}} \quad (1.45)$$

$c$  is the velocity of light. Stop time must be long enough so that all fields in the simulation domain are converged.

### 1.4.2 Rigorous Coupled Wave Analysis (RCWA) method

The RCWA method was first developed in the 1980s [38, 39]. It is also known with alternative names of Fourier modal method and transfer matrix method with a plane wave basis [40]. It is typically known to solve scattering from periodic structures. RCWA is a rigorous method based on the full vectorial solution of Maxwell's equations. In this work, a commercial software package DiffractMOD by RSoft has been used to study diffractive optical structures [36]. It is based on the RCWA method and can be used to solve scattering from complicated periodic structures containing both dielectric and metallic components. Both lossy and dispersive materials can be incorporated. DiffractMOD can be applied to a wide range of devices such as diffraction gratings, polarization-sensitive devices, solar cells, etc., to name a few.

In the RCWA method Maxwell's equations are solved in the Fourier domain where fields are represented as a sum of coupled waves and the periodic dielectric function of the structure is represented as Fourier harmonics [41]. Maxwell's equations from equation (1.41) can be expressed in the frequency domain as:

$$\begin{aligned} \frac{\partial H_z}{\partial y} - \frac{\partial H_y}{\partial z} &= j\omega\epsilon_0\epsilon_{r,x}E_x \\ \frac{\partial H_z}{\partial x} - \frac{\partial H_x}{\partial z} &= -j\omega\epsilon_0\epsilon_{r,y}E_y \\ \frac{\partial H_y}{\partial x} - \frac{\partial H_x}{\partial y} &= j\omega\epsilon_0\epsilon_{r,z}E_z \\ \frac{\partial E_z}{\partial y} - \frac{\partial E_y}{\partial z} &= -j\omega\mu_0H_x \\ \frac{\partial E_z}{\partial x} - \frac{\partial E_x}{\partial z} &= j\omega\mu_0H_y \\ \frac{\partial E_y}{\partial x} - \frac{\partial E_x}{\partial y} &= -j\omega\mu_0H_z. \end{aligned} \quad (1.46)$$

The above equations can be expressed in terms of the transverse fields only by eliminating  $E_z$  and  $H_z$  dependency. The resulting equations are written as:

$$\begin{aligned}
\frac{\partial E_x}{\partial z} &= \left( \frac{-j}{\omega \epsilon_0} \frac{\partial}{\partial x} \frac{1}{\epsilon_{r,z}} \frac{\partial}{\partial y} \right) H_x + \left( \frac{j}{\omega \epsilon_0} \frac{\partial}{\partial x} \frac{1}{\epsilon_{r,z}} \frac{\partial}{\partial y} + j\omega \mu_0 \right) H_y \\
\frac{\partial E_y}{\partial z} &= \left( \frac{-j}{\omega \epsilon_0} \frac{\partial}{\partial y} \frac{1}{\epsilon_{r,z}} \frac{\partial}{\partial x} - j\omega \mu_0 \right) H_x + \left( \frac{j}{\omega \epsilon_0} \frac{\partial}{\partial y} \frac{1}{\epsilon_{r,z}} \frac{\partial}{\partial x} \right) H_y \\
\frac{\partial H_x}{\partial z} &= \left( \frac{j}{\omega \mu_0} \frac{\partial}{\partial x} \frac{\partial}{\partial y} \right) E_x + \left( \frac{-j}{\omega \mu_0} \frac{\partial}{\partial x} \frac{\partial}{\partial x} - j\omega \epsilon_0 \epsilon_{r,y} \right) E_y \\
\frac{\partial H_y}{\partial z} &= \left( \frac{j}{\omega \mu_0} \frac{\partial}{\partial y} \frac{\partial}{\partial y} + j\omega \epsilon_0 \epsilon_{r,x} \right) E_x + \left( \frac{-j}{\omega \mu_0} \frac{\partial}{\partial x} \frac{\partial}{\partial x} \right) E_y.
\end{aligned} \tag{1.47}$$

The periodic structure is divided into simple building blocks which are uniform in the  $z$ -direction. Bloch theorem is used to expand the above equations as well as the boundary conditions. Field components in a periodic structure are expressed as in (1.48). The higher-order terms are eliminated under the constraints of accuracy and speed to reduce the infinitely large number of terms.

$$\begin{aligned}
E_x &= e^{j(k_{x,0}x + k_{y,0}y)} \sum_p \sum_q e^{j\left(\frac{2\pi}{\Lambda_x} px + \frac{2\pi}{\Lambda_y} qy\right)} \sum_m a_{x,m,p,q} \left( f_m e^{j\kappa_m z} + g_m e^{-j\kappa_m z} \right) \\
E_y &= e^{j(k_{x,0}x + k_{y,0}y)} \sum_p \sum_q e^{j\left(\frac{2\pi}{\Lambda_x} px + \frac{2\pi}{\Lambda_y} qy\right)} \sum_m a_{y,m,p,q} \left( f_m e^{j\kappa_m z} + g_m e^{-j\kappa_m z} \right) \\
H_x &= e^{j(k_{x,0}x + k_{y,0}y)} \sum_p \sum_q e^{j\left(\frac{2\pi}{\Lambda_x} px + \frac{2\pi}{\Lambda_y} qy\right)} \sum_m a_{x,m,p,q} \left( f_m e^{j\kappa_m z} - g_m e^{-j\kappa_m z} \right) \\
H_y &= e^{j(k_{x,0}x + k_{y,0}y)} \sum_p \sum_q e^{j\left(\frac{2\pi}{\Lambda_x} px + \frac{2\pi}{\Lambda_y} qy\right)} \sum_m b_{x,m,p,q} \left( f_m e^{j\kappa_m z} - g_m e^{-j\kappa_m z} \right)
\end{aligned} \tag{1.48}$$

Using the above formulations, the problem is reduced to an eigen value problem as:

$$\mathbf{Ax} = \lambda \mathbf{x}. \tag{1.49}$$

Here  $\mathbf{A}$  comes from operators in (1.47),  $\lambda = \kappa_m^2$  is the required eigenvalue and  $a, b$  in (1.48) are calculated from the corresponding eigen values. Equation (1.48) can also be solved by the transmission-line methods. RCWA being a frequency domain method is an efficient solution to calculate reflection and transmission efficiencies of the diffracted orders from a diffractive optical element. Total reflectance, total transmittance can also be derived. The spatial field distribution can also be calculated.

### 1.4.3 Beam Propagation Method (BPM)

BPM is a widely used numerical method to study light propagation in optical waveguides. It is based on the numerical solution of the Helmholtz equation. BPM calculates the field profile along the waveguide given the refractive index information

over the entire waveguide structure. It is one of the most efficient numerical techniques requiring less memory and computation time to simulate complex structures with large index discontinuity [35]. The most advanced implementations of the BPM techniques involve wide-angle [42] and full vectorial algorithms with the ability to incorporate polarization effects, transparent boundary conditions, and taking care of back reflections. Furthermore, the anisotropic and nonlinear materials can also be modeled. A commercial BPM package by RSoft called BeamPROP has been used for simulations in this work. BPM-Matlab is an open-source resource especially for simulating light propagation in a wide variety of optical fiber geometries [43].

The simplest implementation of the BPM is based on the solution of the wave equation known as Helmholtz equation (1.50) under the assumptions of a scalar field and paraxiality which means the field polarization is neglected and propagation is restricted to a narrow range of angles.

$$\frac{\partial^2 E}{\partial x^2} + \frac{\partial^2 E}{\partial y^2} + \frac{\partial^2 E}{\partial z^2} + k^2(x, y, z)E = 0 \quad (1.50)$$

Here,  $E(x, y, z, t) = Ee^{-j\omega t}$  is the scalar field and  $k(x, y, z) = k_0 n(x, y, z)$  is the spatial dependent wavenumber with  $k_0$  being the free space wavenumber. Assuming a slowly varying field in the propagation direction, the field is expressed as:

$$E(x, y, z) = u(x, y, z)e^{-j\beta z} \quad (1.51)$$

where  $\beta$  is the propagation constant representing the average phase variation of the field  $E$ . Exact Helmholtz equation for a slowly varying field is obtained by substituting (1.51) into (1.50).

$$-\frac{\partial^2 u}{\partial z^2} + 2j\beta \frac{\partial u}{\partial z} = \frac{\partial^2 u}{\partial x^2} + \frac{\partial^2 u}{\partial y^2} + (k^2 - \beta^2)u \quad (1.52)$$

Assuming a slowly varying field and applying slow varying envelope approximation, the above equation can be reduced to

$$2j\beta \frac{\partial u}{\partial z} = \frac{\partial^2 u}{\partial x^2} + \frac{\partial^2 u}{\partial y^2} + (k^2 - \beta^2)u. \quad (1.53)$$

Equation (1.53) is the basic BPM equation for a three-dimensional (3D) problem and can be further simplified for a two-dimensional (2D) case by omitting the y dependence. These simplifications represent a first-order initial value problem that can be solved by integrating the above equation along the propagation axis  $z$ . A slowly varying field on the other hand can be solved numerically on a longitudinal grid. For many problems, the longitudinal grid ( $\Delta z$ ) can be much coarser than the wavelength which remarkably increases the efficiency of the technique. However, these relaxations limit the accuracy of the technique for structures with high index contrast along the propagation direction, complicated phase variations, and significant

reflections. The basic BPM equation (1.53) can be solved by several standard numerical methods. Fast Fourier Transform Beam Propagation Method (FFT-BPM) and the Finite-Difference Beam Propagation Method (FD-BPM) are the most prominent methods used to implement BPM. The FD-BPM is generally preferred over FFT-BPM due to its simplicity, higher accuracy, and improved efficiency. The issues of unstable solutions by FD-BPM are further addressed by the Crank-Nicolson scheme [44]. In FD-BPM, the field is represented along the propagation direction  $z$  (longitudinal direction) at the discrete points in the transverse plane ( $xy$ ). The field at the next  $z$  plane is derived from the field at the previous  $z$  plane. The step is repeated to compute the field along with the entire structure. For 2D case, the finite-difference discretization equation can be written as:

$$j \frac{u_i^{n+1} - u_i^n}{\Delta z} = \frac{1}{2\beta} \frac{u_{i+1}^n - 2u_i^n + u_{i-1}^n}{\Delta x^2} + \frac{1}{2\beta} (k_i^2 - \beta^2) \quad (1.54)$$

where  $u_i^n$  represents the field at  $i^{\text{th}}$  transverse grid point and  $n^{\text{th}}$  longitudinal plane,  $\Delta x$  and,  $\Delta z$  are the grid sizes. The inherent limitations with the basic BPM approach have been rectified with advanced implementations such as wide-angle and bi-directional BPM algorithms. The field polarizations are included by the vector BPM approach where the electric field is taken as a vector and derivation is done by vector wave equation instead of scalar field approximation. In the vector BPM approach, the equations are written in terms of coupled equations for slowly varying fields.

$$\begin{aligned} \frac{\partial u_x}{\partial z} &= A_{xx}u_x + A_{xy}u_y \\ \frac{\partial u_y}{\partial z} &= A_{yx}u_x + A_{yy}u_y \end{aligned} \quad (1.55)$$

The  $A_{ij}$  are complex differential operators and are given by the following expressions.

$$\begin{aligned} A_{xx}u_x &= \frac{j}{2\beta} \left\{ \frac{\partial}{\partial x} \left[ \frac{1}{n^2} \frac{\partial}{\partial x} (n^2 u_x) \right] + \frac{\partial^2 u_x}{\partial y^2} + (k^2 - \beta^2) u_x \right\} \\ A_{yy}u_y &= \frac{j}{2\beta} \left\{ \frac{\partial}{\partial y} \left[ \frac{1}{n^2} \frac{\partial}{\partial y} (n^2 u_y) \right] + \frac{\partial^2 u_y}{\partial x^2} + (k^2 - \beta^2) u_y \right\} \\ A_{yx}u_x &= \frac{j}{2\beta} \left\{ \frac{\partial}{\partial y} \left[ \frac{1}{n^2} \frac{\partial}{\partial x} (n^2 u_x) \right] + \frac{\partial^2 u_x}{\partial y \partial x} \right\} \\ A_{xy}u_y &= \frac{j}{2\beta} \left\{ \frac{\partial}{\partial x} \left[ \frac{1}{n^2} \frac{\partial}{\partial y} (n^2 u_y) \right] + \frac{\partial^2 u_y}{\partial x \partial y} \right\} \end{aligned} \quad (1.56)$$

The operators  $A_{xx}$  and  $A_{yy}$  correspond to field shapes and bend losses for TE and TM polarizations whereas  $A_{xy}$  and  $A_{yx}$  consider geometric effects of the structure. The above equations are referred to as full-vectorial BPM implementation. In cases

where coupling between two polarizations is weak, the operators  $A_{xy}$  and  $A_{yx}$  can be neglected. This simplification leads to semi-vectorial approximation.

The wide-angle BPM scheme considers the  $\frac{\partial^2 u}{\partial z^2}$  term which was neglected in the basic BPM approach described by (1.53). The Padé-based wide-angle technique is the most popular formulation to accomplish this. If  $D$  denotes the differential operator  $\frac{\partial}{\partial z}$  then the second-order term is given by the square of  $D$ . This makes (1.52) a quadratic equation in  $D$ , where  $D$  is given as:

$$\frac{\partial u}{\partial z} = j\beta \left( \sqrt{1+P} - 1 \right) u \quad (1.57)$$

where

$$P = \frac{1}{\beta^2} \left( \frac{\partial^2}{\partial x^2} + \frac{\partial^2}{\partial y^2} + (k^2 - \beta^2) \right). \quad (1.58)$$

The differential operator  $P$  is expanded via Padé approximations leading to the following wide-angle equation.

$$\frac{\partial u}{\partial z} = j\beta \frac{N_m(P)}{D_n(P)} u \quad (1.59)$$

$N_m$  and  $D_n$  are the polynomials of the differential operator  $P$  and  $(m,n)$  is the Padé order of approximation.



## Chapter 2

# Design, Fabrication, and Characterization of Pillar Gratings

### 2.1 Guided-Mode Resonance

Guided-mode resonance (GMR) is a physical phenomenon that originates when the guided modes of an optical waveguide are excited by the diffracted orders of a diffraction grating under the phase matching conditions. They are also called as leaky modes as the light that couples in also couples out. Two physical incidents are responsible for generating GMR – the diffraction from a grating and the waveguiding in a slab waveguide. A sketch of a diffraction grating on top of a slab waveguide is shown in Fig.2.1. A slab waveguide consists of a slab of high index material ( $n_2$ ) sandwiched between the two low index materials ( $n_1, n_3$ ). It works on the principle of total internal reflection based on Snell's law as described by the equation (2.1) which states that a light wave travelling from a high to low index material is totally reflected if the angle of the incident is greater than the critical angle  $\theta_c$ .

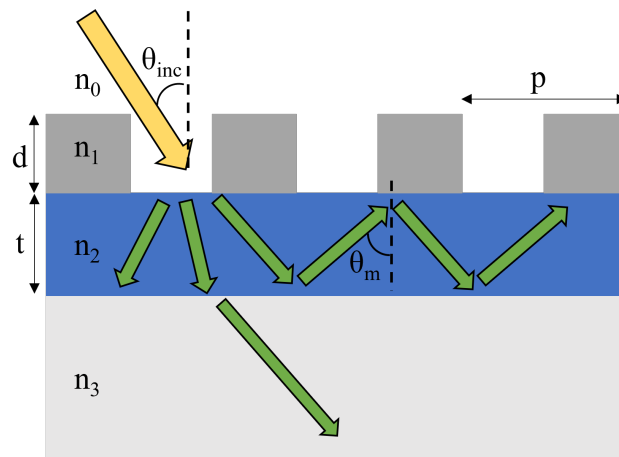


FIGURE 2.1: A sketch of a diffraction grating having a period  $p$  placed on a slab waveguide. The refractive index of the waveguide layer  $n_2$  is greater than the refractive index of the cladding layer  $n_1$  and the substrate  $n_3$ .

$$\theta_c = \sin^{-1} \left( \frac{n_1}{n_2} \right) \quad (2.1)$$

According to the ray tracing analysis only certain angles are allowed and the propagation constant  $\beta$  of a supported mode by the slab waveguide is give as:

$$\beta = k_0 n_{eff} = k_0 n_2 \sin(\theta_m) \quad (2.2)$$

here,  $k_0 = 2\pi/\lambda$  and  $\theta_m$  is the allowed angle of propagation. A complete analysis of a slab waveguide and its mode solutions involves rigorous techniques such as RCWA. A detailed theoretical description of the GMR is given by S.S. Wang and R. Magnusson [45]. TE and TM modes for a slab waveguide are given by the following equations (2.3) and (2.4), respectively.

$$\tan(\kappa_i t) = \frac{\kappa_i(\gamma_i + \delta_i)}{\kappa_i^2 - \gamma_i \delta_i} \quad (2.3)$$

$$\tan(\kappa_i t) = \frac{n_1^2 \kappa_i (n_3^2 \gamma_i + n_0^2 \delta_i)}{n_0^2 n_3^2 \kappa_i^2 - n_1^2 \gamma_i \delta_i} \quad (2.4)$$

where

$$\begin{aligned} \kappa_i &= \sqrt{n_2^2 k^2 - \beta_i^2} \\ \gamma_i &= \sqrt{\beta_i^2 - n_0^2 k^2} \\ \beta_i &= k(n_0 \sin(\theta_{inc}) - m \frac{\lambda}{p}) \\ k &= \frac{2\pi}{\lambda} \end{aligned}$$

The angles of the diffracted orders can be calculated from the grating equation which is given below.

$$n_2 \sin(\theta_m) = n_1 \sin(\theta_{inc}) - m \frac{\lambda}{p} \quad (2.5)$$

Under phase matching condition, the effective refractive index of the guided modes can be deduced from equations (2.2) and (2.5).

$$n_{eff} = n_1 \sin(\theta_{inc}) - m \frac{\lambda}{p} \quad (2.6)$$

For a guided mode, the neff has the following constraints.

$$\max[n_1, n_3] \leq n_{eff} < n_2 \quad (2.7)$$

By inserting value of  $n_{eff}$  from equations (2.6) into the above inequality a final expression is obtained which describes the region for the guided-mode resonance.

$$\max[n_1, n_3] \leq |n_1 \sin(\theta_{inc}) - m \frac{\lambda}{p}| < n_2 \quad (2.8)$$

## 2.2 Graphene based pillar grating for optical absorber

### 2.2.1 State of the art

Graphene has emerged as an attractive two-dimensional material due to its exceptional mechanical, electrical and optical properties [46]. Monolayer graphene exhibits better absorbance than different dielectric and metals of the same thickness. A considerable amount of theoretical and experimental work has been published in recent years to explore the potential of graphene in optical and microwave absorbers in different spectral ranges of the electromagnetic spectrum for various applications such as biosensors, optical filters, modulators, and efficient photodetector [47, 48, 49]. Monolayer graphene shows a constant absorption of about 2.3% over the visible and near-infrared wavelengths [50]. However, in the context of optical absorbers, this value is not enough substantially limiting its use in photonic devices. Therefore, enhancement of light absorption by monolayer graphene has drawn significant attention of researchers and several solutions have been proposed in the technical literature to achieve the perfect absorption. One and two-dimensional dielectric gratings exploit guided-mode resonance (GMR) to increase light-matter interaction. Light can be effectively coupled to graphene if incorporated with such gratings [51]. By varying geometrical parameters of the grating structure, the resonant wavelength and the bandwidth of absorption can be tuned. A number of numerical studies [52, 53, 54, 55] report perfect absorption of light in graphene incorporated dielectric gratings over diverse spectral ranges. Recently, near total absorption in monolayer graphene based on critical coupling was presented at a visible wavelength of 605 nm [56]. In some other recent studies, multilevel structures were investigated and enhanced graphene absorption was reported [57, 58, 59]. The main drawback of the multilevel structures is the complexity of the fabrication process since it requires the deposition of multiple material layers. Experimental and measured results for several fabricated graphene-based structures have also been presented [15-18]. The maximum experimentally measured values of absorption reported are 35% at  $0.73\mu\text{m}$  [60], 40% at  $0.7\mu\text{m}$  [61], 45% at  $10\mu\text{m}$  [62] and 99% at  $1.48\mu\text{m}$  [63]. However, perfect, broadband, tunable and polarization-independent absorption of light in monolayer graphene for photonic applications is still a challenging problem and needs further research and exploration. In this framework, it is worth pointing out that the absorption spectra of resonant gratings are highly sensitive to the angle of incident light.

In previous work, it has been demonstrated that graphene-based gratings can be exploited to modulate the Fano-like signature of GMRs [64]. Moreover, 2D arrays of rectangular gold nano-patches grown on monolayer graphene were used

to experimentally demonstrate the polarization dependence of plasmonic gratings at normal incidence [65]. Apart from grating based structures, perfect absorbers based on metamaterials have also been reported [66, 67, 68, 69]. In this work, a two-dimensional (2D) dielectric grating has been numerically investigated through the rigorous coupled-wave analysis (RCWA) method. Parametric study has been performed for the design optimization. The optical response of the proposed device has been studied under the oblique incidence of a plane wave source. It has been shown that it has a stable optical absorption of around 40% over a considerable wide angular range of  $20^\circ$ . Electromagnetic field distributions at resonant frequencies are presented to explain the underlying physical phenomenon for optical absorption.

### 2.2.2 Design of the two-dimensional grating

Figure 2.2(a) shows the sketch of the proposed 2D dielectric grating. It consists of a periodic array of polymethyl-methacrylate (PMMA) cylindrical pillars deposited on a tantalum pentoxide ( $Ta_2O_5$ ) waveguide. A slab of silicon dioxide ( $SiO_2$ ) is used as a substrate. The monolayer graphene is placed on top of the waveguide under the PMMA pillars. The proposed 2D dielectric grating can be realized by means of Nano Imprint Lithography (NIL) [70]. This technology can foster the faster fabrication of polymeric-based dielectric gratings at low cost. The choice of the proposed 2D configuration is based on the possibility to have an insensitive polarization behaviour at normal incidence for the GMRs that are excited in the  $Ta_2O_5$  dielectric waveguide. The thickness of the monolayer graphene is set equal to  $0.34nm$ . A thin buffer layer of PMMA (20 nm-thick) is also placed over the monolayer graphene considering the quality of graphene is not affected by pillar fabrication. Geometrical parameters of the device are detailed in Figure 1(b). The thickness  $t_{Ta_2O_5}$  of the  $Ta_2O_5$  slab and the PMMA pillar height  $t_{PMMA}$  are initially set equal to  $150nm$  and  $600nm$  respectively. The PMMA pillars have symmetric periodicity both in x- and y- directions and the value is chosen equal to  $600nm$  at the start. The radius  $r$  of the cylindrical PMMA pillars is chosen as  $250nm$ .

The 2D graphene-based dielectric gratings were simulated by means of RSoft-DiffactMOD that implements a Fourier-space method, the rigorous coupled-wave analysis (RCWA), to solve scattering from periodic structures. The refractive indices for PMMA,  $Ta_2O_5$ , and  $SiO_2$  were retrieved from Palik et al. [71]. For monolayer graphene, complex refractive index  $n = 3 + jC_1 * \lambda/3$  reported in [29] at visible wavelengths is used where  $C_1$  is equal to  $5.446\mu m^{-1}$  and  $\lambda$  is the free space wavelength, to take into account the losses.

### 2.2.3 Numerical results

Figure 2.3 shows the reflectance, transmittance, and absorption spectra of the device with and without graphene layer for the TE and TM polarizations at normal incidence. For TE electric field is launched along x-axis whereas for TM the electric field

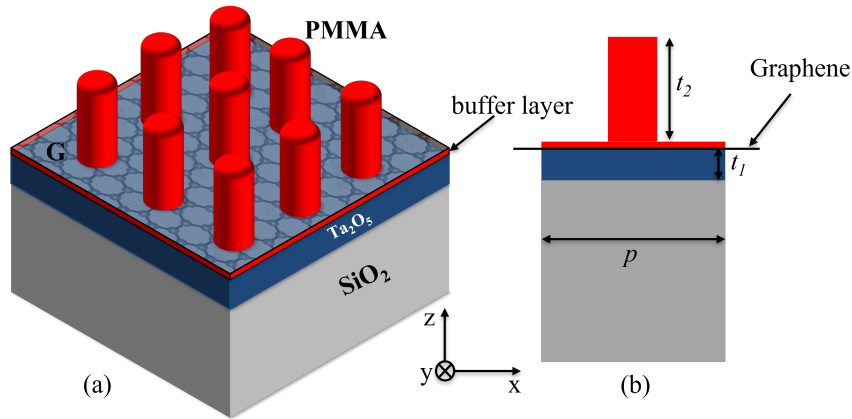


FIGURE 2.2: (a) Sketch of a 2D graphene-based dielectric grating with an array of cylindrical nanopyllars. (b) The cross-sectional ( $xz$ ) view of the single period of the device used for simulations.

is launched along  $y$ -axis. The absorption spectra show resonant peaks at the  $0.71\mu m$ ,  $0.9\mu m$ , and  $0.96\mu m$  wavelengths. These correspond to absorption of 20%, 50%, and 40% respectively. The absorption is zero when the structure has no graphene layer since the configuration is lossless. It can be noted that the optical response is insensitive to the polarization of the incoming light wave due to the symmetry of the device (2D square lattice).

The electromagnetic field distributions are shown in Fig.2.4 (a)-(d) at the resonant wavelength of  $0.9\mu m$  (maximum absorption) for the TE and TM polarizations, respectively. It clearly illustrates that the fields are concentrated around monolayer graphene. The white lines represent the device structure where the monolayer graphene is positioned at  $z = 0.15\mu m$  (that corresponds to the thickness of the  $Ta_2O_5$  and buffer layers). The comparison between Fig.2.4(a-b) (with graphene) and Fig.2.4(c-d) (without graphene) shows the difference between the values of field magnitudes of about a factor 2.

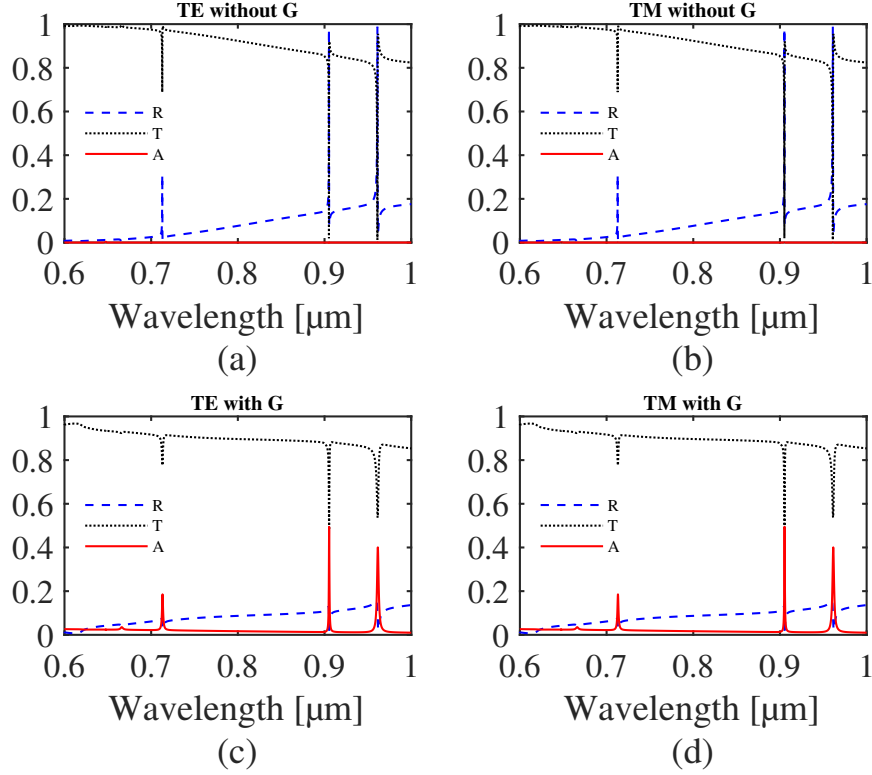


FIGURE 2.3: Optical reflectance (dashed blue line), the transmittance (dotted black line), and absorption (solid red line) spectra (a-b) without and (c-d) with graphene layer for both (a-c) TE and (b-d) TM plane waves at normal incidence. The device period  $p$ , waveguide  $\text{Ta}_2\text{O}_5$  thickness  $t_{\text{Ta}_2\text{O}_5}$ , and PMMA pillars height  $t_{\text{PMMA}}$  for this simulation result are set as  $600\text{nm}$ ,  $150\text{nm}$ , and  $600\text{nm}$  respectively.

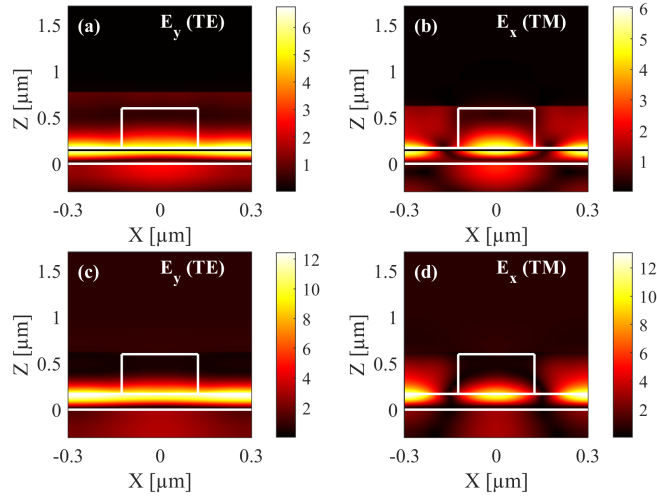


FIGURE 2.4: Field profiles (a) amplitude of  $E_y$  component and (b) amplitude of  $E_x$  component at  $0.9\mu\text{m}$  for the device parameters of Fig.2.2. The white lines show the device structure where the monolayer graphene is positioned at  $z = 0.15\mu\text{m}$  (marked by the black line). (c-d) field profiles without the monolayer graphene.

Next, the optimization of the device geometrical parameters has been performed. Figure 2.5 describes the absorption ( $A$ ) spectra at different grating periods ( $p$ ) while  $Ta_2O_5$  layer thickness  $t_{Ta_2O_5}$  and PMMA pillar height  $t_{PMMA}$  are kept constant. It is evident that absorption peak wavelength can be tuned over the visible and near-infrared wavelengths by changing the grating period. The sliding of the resonant wavelengths with increasing device period agrees well with the analysis presented in [51]. Each absorption spectrum shows multiple peaks which result from multiple guided mode resonances. Also, there is an increase in absorption with increasing period length. Since the device is polarization independent for normally incident plane waves, therefore, the absorption spectra for TE polarized plane waves have been shown only.

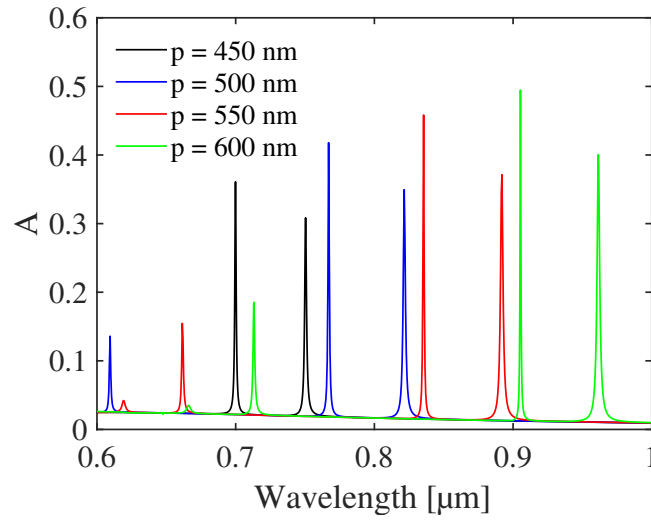


FIGURE 2.5: Absorption spectra of the proposed structure under varying grating period for normally incident TE polarized plane wave. The waveguide  $Ta_2O_5$  thickness  $t_{Ta_2O_5}$ , and PMMA pillars height  $t_{PMMA}$  are fixed at  $150nm$  and  $600nm$  respectively.

The effects of variation of  $Ta_2O_5$  layer thickness  $t_{Ta_2O_5}$  and PMMA pillar height  $t_{PMMA}$  on the absorption spectrum have also been investigated. Figure 2.6(a) depicts the effect of change of  $t_{Ta_2O_5}$  on the absorption spectrum. There is a red shift in the resonant wavelength as the thickness of the  $Ta_2O_5$  waveguide is increased from  $80nm$  to  $160nm$ . Multiple resonances appear among which the prominent ones can be seen in the absorption map. Figure 2.6(b) shows the effect of change of  $t_{PMMA}$  on the absorption spectrum revealing no changes when the PMMA thickness is varied in the range of  $300nm$  to  $900nm$ .

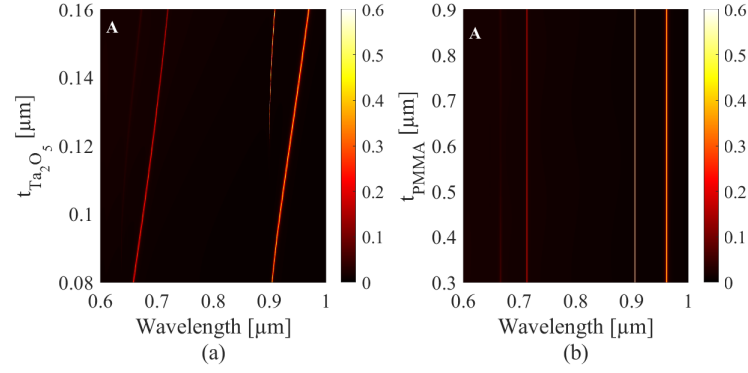


FIGURE 2.6: (a) Absorption map with respect to the variation of  $Ta_2O_5$  layer thickness  $t_{Ta_2O_5}$  under TE at normal illumination when the period  $p$  and PMMA pillar height  $t_{PMMA}$  are fixed at  $600nm$  and  $600nm$  respectively. (b) Absorption map under TE normal illumination, when PMMA pillar thickness  $t_{PMMA}$  is varied from  $300nm$  to  $900nm$ . The period  $p$  and waveguide  $Ta_2O_5$  thickness  $t_{Ta_2O_5}$  are fixed at  $600nm$  and  $150nm$  respectively.

Further, the optical response of the proposed device has been analysed under the oblique incidence of the plane wave source. Figure 2.7 shows the absorption maps when the incidence angle is changed from  $0^\circ$  to  $90^\circ$  for both TE and TM polarizations. It can be observed from the maps that the resonance at normal incidence splits into two arms for angular incidence. This behaviour is typical of a grating structure that can be derived by the absorption spectra. It is interesting to note that the absorption spectra do not split into two arms for certain resonant wavelengths and absorption is nearly independent of the source angle for specific angular ranges.

To further elaborate these important results, the absorption spectra of the device for both TE and TM polarizations are shown in Fig.2.8 in an angular range of  $0^\circ - 20^\circ$  for two different device periods. The absorption is limited within narrow bandwidths of  $\sim 15nm$  and  $\sim 20nm$  for the maps in (a-b) and (c-d) respectively over a considerable wide angular range of  $20^\circ$ . The slope is about  $0.5nm/degree$  in the  $0^\circ - 10^\circ$  range.

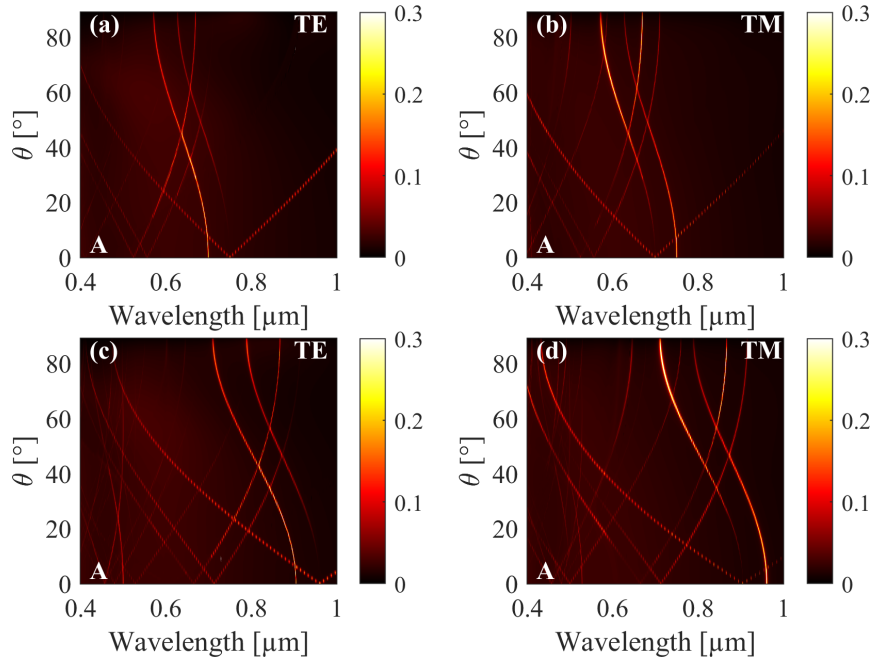


FIGURE 2.7: Absorption maps of the device for varying incidence angle ( $0^\circ - 90^\circ$ ) under both TE and TM polarizations. For (a) and (b) device period  $p$ , the waveguide  $Ta_2O_5$  thickness  $t_{Ta_2O_5}$ , and PMMA pillars height  $t_{PMMA}$  are fixed at  $450nm$ ,  $150nm$ , and  $600nm$  respectively whereas for (c) and (d) the period  $p$  is changed to  $600nm$ .

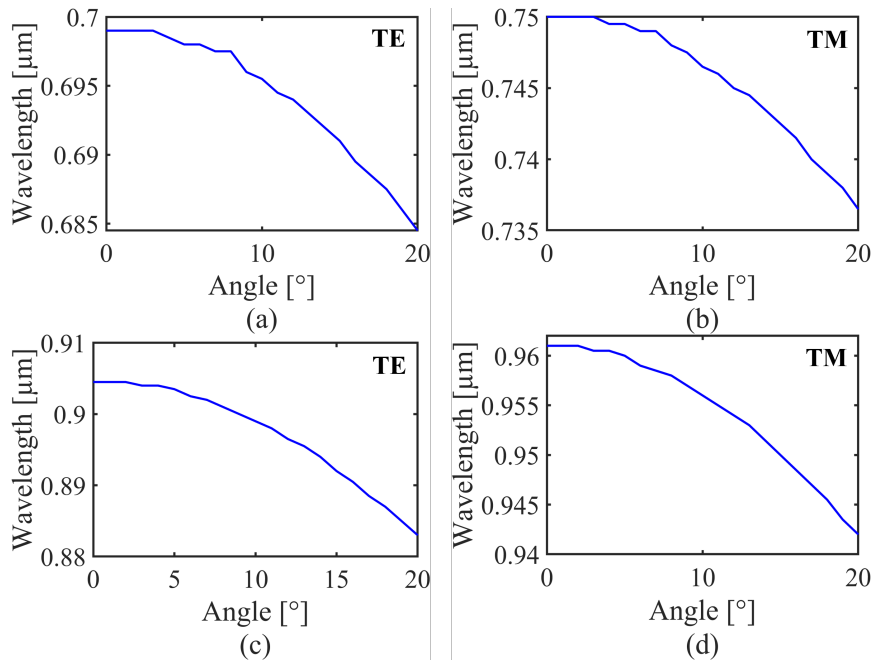


FIGURE 2.8: Peak absorption wavelength when the incident angle is varied in range  $0^\circ - 20^\circ$ . (a-b) The device period  $p$ , the waveguide  $Ta_2O_5$  thickness  $t_{Ta_2O_5}$ , and PMMA pillars height  $t_{PMMA}$  are fixed at  $450nm$ ,  $150nm$ , and  $600nm$  respectively. (c-d) The device period  $p$ , the waveguide  $Ta_2O_5$  thickness  $t_{Ta_2O_5}$ , and PMMA pillars height  $t_{PMMA}$  are fixed at  $600nm$ ,  $150nm$ , and  $600nm$  respectively.

Another important result is depicted in Fig.2.9 which shows absorption spectra in an angular range of  $70^\circ - 90^\circ$ . It can be noted that the absorption is limited in narrow bandwidths of  $\sim 25nm$  and  $\sim 10nm$  nm for the angular ranges of  $70^\circ - 90^\circ$  and  $75^\circ - 90^\circ$  respectively in both (a) and (b) maps. Furthermore, the device behaviour is similar under both TE and TM polarizations.

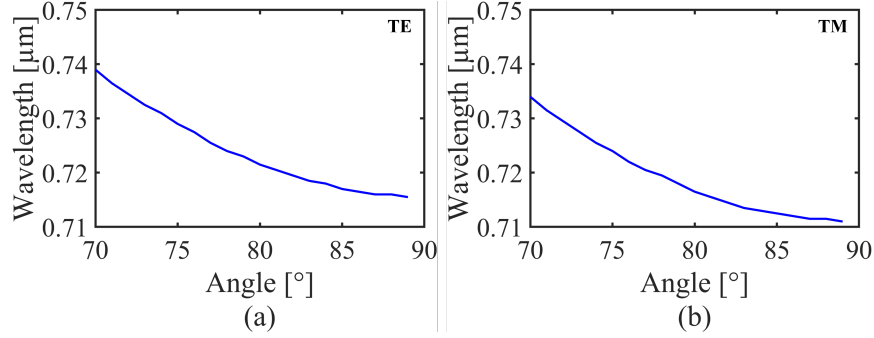


FIGURE 2.9: Peak absorption wavelength of the device for varying incidence angle ( $70^\circ - 90^\circ$ ) under both TE and TM polarizations. The device period  $p$ , the waveguide  $Ta_2O_5$  thickness  $t_{Ta_2O_5}$ , and PMMA pillars height  $t_{PMMA}$  are fixed at  $600nm$ ,  $150nm$ , and  $600nm$  respectively.

In short, the observations in Figs.2.8 and 2.9 prove the near insensitivity of the proposed device to the angle and polarization of the incident light in multiple angular ranges of around  $20^\circ$ . Angular response of the proposed device shows clear improvement compared to results reported in [60] for graphene-based absorber based on a one-dimensional grating where absorption spectra split into two arms from  $0^\circ - 20^\circ$  under similar simulation conditions.

## 2.2.4 Discussion

In previous works [60, 61], light absorption in graphene-based 1D dielectric gratings based on PMMA rectangular strips has been experimentally demonstrated. However, the response of the structures is sensitive to the oblique incidence of light. The proposed device is based on a 2D grating of cylindrical PMMA pillars that exploit GMRs to enhance light absorption in the monolayer graphene. The proposed structure achieved light absorption of more than 40% at multiple wavelengths for both TE and TM polarizations over narrow bandwidths in the visible and near-infrared ranges. The device performance is insensitive to variation in the PMMA pillar height which is an important measure in terms of device stability and fabrication tolerances.

The simulation results further revealed that the device has a considerable stable angular response. The absorption spectra are nearly independent of the angle of the impinging light up to  $20^\circ$  with a slope of  $\sim 0.5nm/degree$ . Moreover, the response is less sensitive to the polarization of the incident plane waves.

In conclusion, the proposed optical absorber is less sensitive to geometrical parameters variations, polarization, and angle of the incident light. It can be easily realized using nanofabrication technologies such as nano-imprint lithography. These results pave the way to the realization of polarization insensitive optical absorbers that can be efficiently exploited in several applications and photonic devices such as biosensors, optical filters, modulators, and efficient photodetectors.

## 2.3 Thermal tuning of resonant grating using phase change material

### 2.3.1 State of the art

Phase change materials are currently receiving great attention for the development of tunable photonic devices. The phase transition can be controlled externally by temperature, electrical, or an optical signal. This results in drastic changes in the electrical and optical properties of the material. The ability to dynamically change the physical characteristics of the material can open-up new possibilities for the design and fabrication of the electrical and optical devices whose response can be dynamically controlled and modulated. Some of these materials, namely GeSbTe (GST), have been successfully adopted in photonic devices [72]. Vanadium dioxide ( $\text{VO}_2$ ) is one of the most promising phase change materials. It undergoes reasonably large changes in the refractive index under a low intensity stimulus. The insulator to a metal phase transition happens at a temperature of  $68^\circ\text{C}$  which is easily attainable under ordinary circumstances. The phase transition of  $\text{VO}_2$  is reversible once the external stimulus is removed and it can withstand millions of cycles. Moreover, the phase transition is achievable over broadband range of optical wavelengths from visible to infrared. Numerous types of  $\text{VO}_2$  based devices have been demonstrated for nanophotonic applications including tunable metasurfaces for optical absorbers and polarization converters [73, 74, 75, 76, 77, 78, 79, 80], tunable optical waveguides and nano-antennas [32], [81], and sensors based on switchable plasmonic structures of  $\text{VO}_2$  [82].

In this work, a numerical study of a resonant grating structure coated with a thin layer of  $\text{VO}_2$  has been performed to investigate the optical response of the structure under phase change behaviour of the  $\text{VO}_2$  layer. The grating structure supports guided mode resonances [83], and the resonant grating has a large sensitivity to the refractive index changes in the surrounding media. Guided mode resonances have been exploited for numerous useful applications in the photonic devices [9], [60], [61]. Together with a resonant grating structure, the phase transition properties of a phase change material such as  $\text{VO}_2$  can lead to newer prospects for tunable photonic devices. The theoretical simulations are performed by rigorous coupled-wave analysis (RCWA) where a temperature dependent complex-refractive-index data for thin films of  $\text{VO}_2$  over the visible and infrared wavelength range has been

incorporated in the numerical model. Under a thermal stimulus, the phase change behaviour of VO<sub>2</sub> nanoparticles have been exploited to modulate the reflectance of the structure. In the following sections, the design, fabrication, and characterization of the proposed configuration are detailed. The PMMA nanopillars are fabricated on a sputtered Cu/AlN bilayer using a nanoimprint lithography system exploiting a silicon mold. The VO<sub>2</sub> nanoparticles are deposited by spin-coating. The fabricated samples are characterized by means of an ad-hoc setup in which a heater produces a temperature ramp from room temperature to 80°C. The experimental results are in good agreement with the numerical findings.

### 2.3.2 Numerical model

The resonant structures under discussion are sketched in Fig.2.10. Figure 2.10(a) shows an ultra-thin film of VO<sub>2</sub> supported on a glass substrate. This structure is used as a reference to compare the higher values of switching in the reflectance achieved when an ultra-thin film of VO<sub>2</sub> is used with a resonant grating. The structure in Fig.2.10(b) consists of an optically thick layer of copper, an aluminium nitride (AlN) dielectric spacer and a VO<sub>2</sub> thin film on top. This kind of three-layered structure acts as a Fabry-Pérot resonator. Finally, Figure 2.10(c) shows a polymethyl methacrylate (PMMA) nano-pillar grating with a square lattice ( $p_x = p_y$ ) built on a slab waveguide of AlN that is grounded by a thick copper (Cu) layer. An ultra-thin film of VO<sub>2</sub> then coats the waveguide layer, as well as the top surface of nanopillars. The geometrical parameters are designed to ensure grating resonances in the VIS-NIR range. This structure can support several different resonances, for example, Mie resonances when pillars act individually and Fano-like resonances when nanopillars collectively act a grating. Surface plasmon polaritons confined near the copper surface can be other possible modes of this structure. The photonic modes can be designed at any wavelength from visible to infrared by optimizing the geometrical parameters of the structure. The signature resonances can be observed in the reflectance spectra of the structure given the fact that the transmittance through the structure is abated by the copper layer. The photonic modes can be designed at almost any wavelength in the visible and infrared ranges by optimizing the geometrical parameters of the structure [10].

A rigorous coupled-wave analysis (RCWA) method is used for the optical simulations. A unit cell of the grating structure is used under a linearly polarized plane wave excitation propagating in the -z direction. Periodic boundary conditions are set in the x and y directions whereas perfectly matched layer boundary conditions are used along z direction.

VO<sub>2</sub> has a phase transition temperature  $\sim 68^\circ\text{C}$  which is very near to room temperature. Below the phase transition temperature, it acts an insulator whereas above the phase transition temperature it in in a metallic state. When this material is heated above the phase transition temperature there is a structural change inside the material from a monoclinic insulator phase to a tetragonal metallic phase. This results in

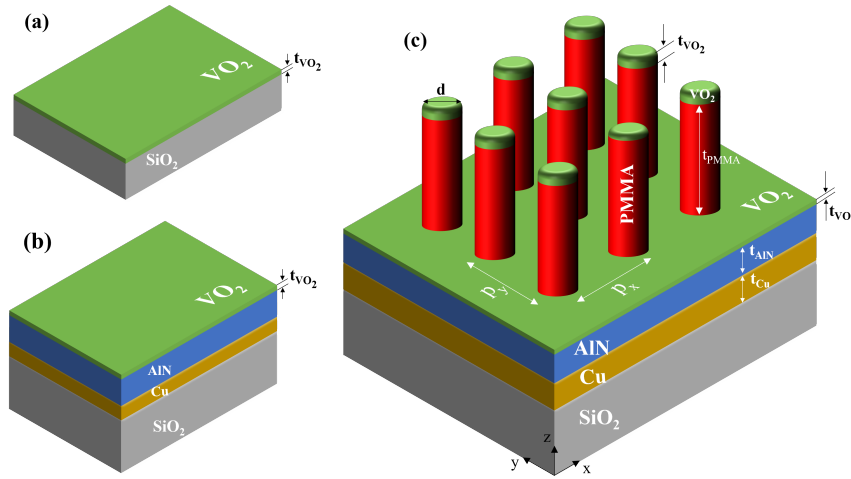


FIGURE 2.10: (a) A sketch of an unpatterned semi-infinite ultra-thin VO<sub>2</sub> film on top of a glass substrate, (b) A sketch of an unpatterned semi-infinite VO<sub>2</sub> film on top of a AlN/Cu bilayer supported by glass substrate, (c) A sketch of the periodic array of nano-pillars coated with an ultra-thin film of VO<sub>2</sub>.

changes in the electrical and optical properties of the material. The experimentally measured refractive index data for a thin film of VO<sub>2</sub> is taken from [33]. The details of measured complex refractive index of vanadium dioxide at two different temperatures, 30°C and 100°C which corresponds to an insulator and a metallic phase of the material are given in Chapter 1 section 1.4. In all simulations, the reflectance spectra are calculated at two different temperatures, i.e.,  $T < T_0$  ( $T_0$  being the phase transition temperature of VO<sub>2</sub>) which corresponds to the insulating phase of VO<sub>2</sub> and  $T > T_0$  which corresponds to the metallic phase of VO<sub>2</sub>.

### 2.3.3 Numerical results

Figure 2.11 shows the reflectance spectra from an unpatterned semi-infinite ultra-thin ( $\lambda/60$ ) film of VO<sub>2</sub> on a glass substrate (Fig.2.10(a)) under normal incidence for the low temperature insulating and high temperature metallic phases as well as the absolute difference between the two. The black dotted curves represent the absolute difference ( $\Delta = R_{insulator} - R_{metal}$ ) in the reflectance spectra. It is observed that an ultra-thin film of VO<sub>2</sub> is totally transparent at VIS-NIR wavelengths for both low and high temperature states. An unpatterned ultra-thin film of VO<sub>2</sub> on a sapphire substrate has been demonstrated as a perfect absorber at  $11.75\mu m$  [84].

The results shown in Fig.2.12 show the optical response of the unpatterned semi-infinite structure shown in Fig.2.10(b). In particular, Fig.2.12(a) depicts the delta-reflectance spectra obtained under normal incidence where the delta-reflectance is defined as the difference between the reflectance at low (insulator) and high temperature (metal) states. As it can be inferred by the plot in Fig.2.12(a), there is no prominent change in the reflectance for an ultra-thin layer of VO<sub>2</sub> (i.e. thickness of

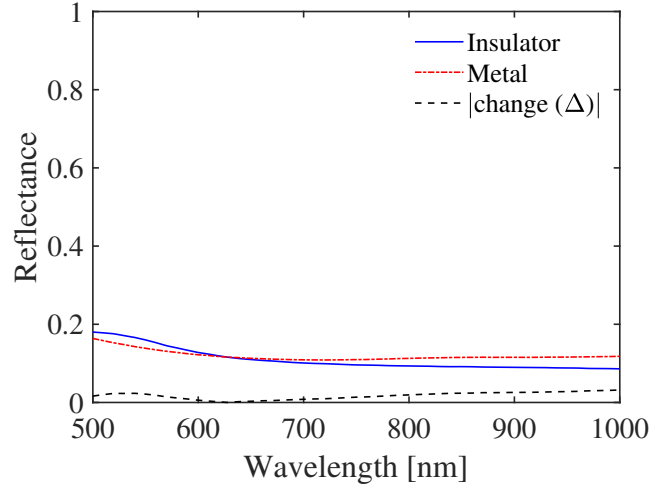


FIGURE 2.11: Reflectance spectra from a semi-infinite ultra-thin ( $\lambda/60 = 10nm$ ) layer of  $VO_2$  under normal incidence for the low temperature insulating (blue line) and high temperature metallic (dashed-dotted red line) phases as well as the absolute difference between the two (dashed black line).

few nanometers). Conversely, as the thickness of the  $VO_2$  layer is increased, the reflectance shows a notable phase transition effect. It is shown that a thermal control of the  $VO_2$  phase enables up to 40% switching in the reflectance. This broadband reflectance change shows a red shift as the thickness of  $VO_2$  layer is increased. For a fixed thickness of  $VO_2$  film, the thickness of AlN layer can be adjusted to spectrally tune the switching response over the VIS-NIR wavelengths. This is illustrated in Fig.2.12(b) where the thickness of the AlN layer is varied from 80 to 160nm. For a 150nm thick AlN layer, a broadband change ( $\Delta\lambda \sim 200nm$ ) in the reflectance spectra is obtained with a maximum value of 35% centered at a wavelength of 752nm. This is mentioned by a dashed-dotted white line in Fig.2.12(b) and the corresponding spectral response is shown in Fig.2.12(c). Similarly, Fig.2.12(d) shows the spectral response of the structure when the thickness of AlN layer is set to 90nm.

Next, the resonant grating structure shown in Fig.2.10(c) is studied. Two different grating periodicities  $p_x = p_y$  of 670nm and 750nm are considered in this study. The PMMA pillar has height ( $t_{PMMA}$ ) and diameter ( $d$ ) of 590nm and 275nm, respectively. The AlN waveguide layer atop the copper layer and the copper layer are both 150nm thick. The entire structure is coated with an ultra-thin  $VO_2$  film of 10nm thickness.

Reflectance spectra of the grating structure with a period of 750nm is shown in Fig.2.13(a). The grating structure introduces resonances at 752nm and 760nm in the reflectance spectra. At resonance, more than 40% and 30% switching is observed in the reflectance at 752nm and 760nm, respectively. The grating also introduces a filtering effect. The broadband reflectance change from an unpatterned semi-infinite  $VO_2$  layer reduces to a narrowband response centered around the resonant wavelengths. Since the switching response can be tuned in VIS-NIR range by changing the thickness of AlN, Fig. 2.13(b) shows the reflectance spectra from a grating with

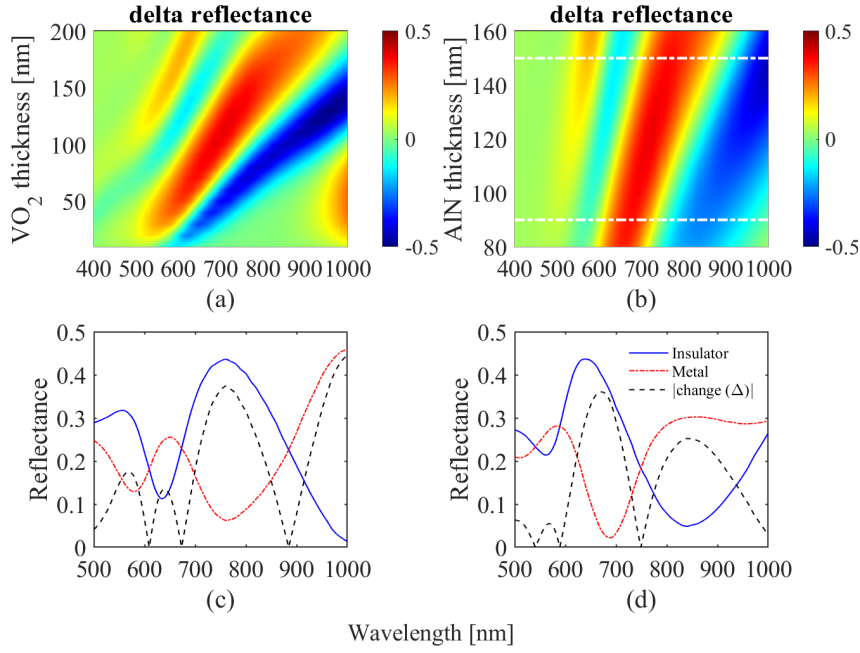


FIGURE 2.12: (a) Map of the delta-reflectance spectra from an unpatterned semi-infinite structure shown in Fig.2.10(b) under normal incidence when the thickness of  $\text{VO}_2$  film is changed from  $10\text{nm}$  to  $200\text{nm}$ . The thickness of  $\text{AlN}$  layer is fixed at  $150\text{nm}$ . (b) Map of the delta-reflectance spectra from an unpatterned semi-infinite structure shown in Fig. 2.10(b) covered with a thin ( $150\text{nm}$ ) film of  $\text{VO}_2$  under normal incidence when the thickness of  $\text{AlN}$  layer is changed from  $80\text{nm}$  to  $160\text{nm}$ . (c) Line plots of the reflectance corresponding to the upper white line ( $t_{\text{AlN}} = 150\text{nm}$ ) in (b) showing the low temperature insulating (blue line) and high temperature metallic (dashed-dotted red line) phases as well as the absolute difference between the two (dotted black line). (d) As in (c) corresponding to the lower white line ( $t_{\text{AlN}} = 90\text{nm}$ ) in (b).

a period of  $670\text{nm}$ . For this structure the thickness of  $\text{AlN}$  is set to be  $90\text{nm}$ . A 30% switching in the reflectance is obtained at the resonant wavelength of  $679\text{nm}$ . These results are rather remarkable considering the fact that an ultra-thin layer of  $\text{VO}_2$  is incorporated with the grating structure. The large change in the reflectance may be associated with increased sensitivity to small variations in refractive index of the surrounding media, and to the strong light matter interaction under resonant conditions of the structure. The strong light matter interaction at resonance may be quantified by the strength of field enhancement when a photonic mode of the grating is excited at the resonant wavelength of  $752\text{nm}$  under normal incidence. The enhanced electric and magnetic fields are plotted in Fig.2.14.

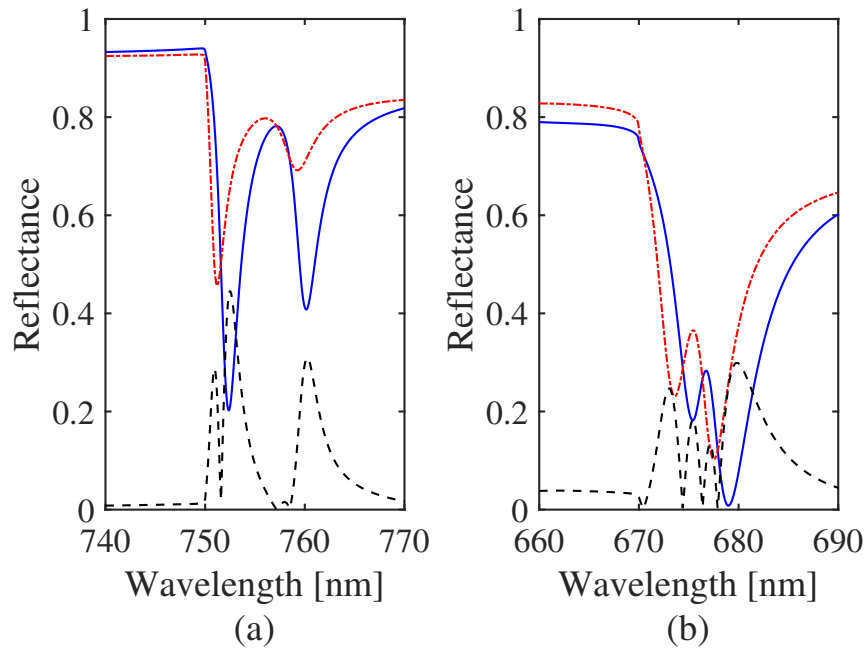


FIGURE 2.13: Reflectance spectra of a pillar grating coated with an ultra-thin ( $10\text{nm}$ ) film of  $\text{VO}_2$  under normal incidence for the low temperature insulating (blue line) and high temperature metallic (dashed-dotted red line) phases as well as the absolute difference between the two (dotted black line). The grating has a period of  $750\text{nm}$  and AlN layer has a thickness of  $150\text{nm}$ . (b) Same as in (a) for a grating that has a period of  $670\text{nm}$  and AlN layer has a thickness of  $90\text{nm}$ .

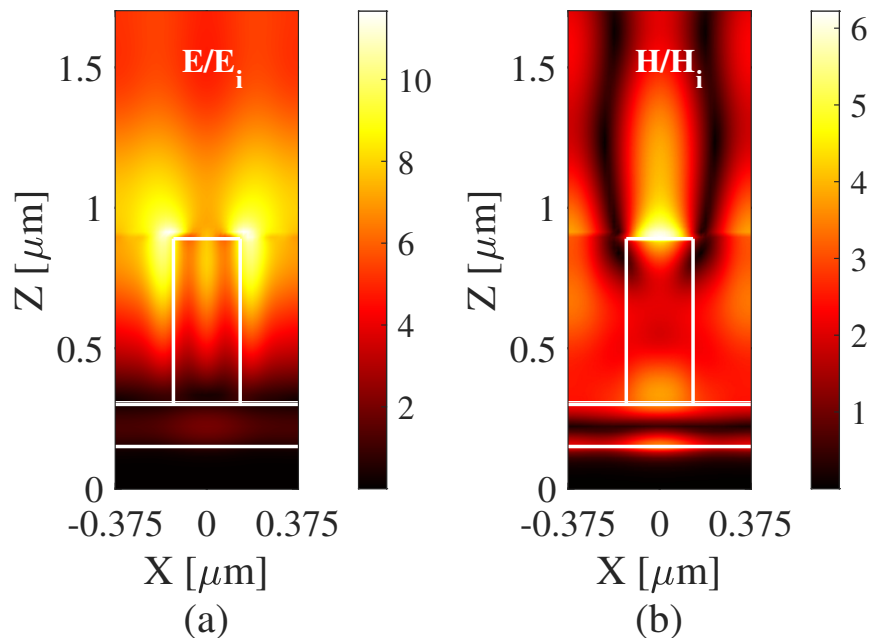


FIGURE 2.14: Electric and magnetic fields enhancement on resonance at  $752\text{nm}$  for the configuration in Fig.2.10(c).

In order to study the effects of oblique incidence and different polarizations the

change in the reflectance was plotted in Fig.2.15 for the two structures shown in Figs.2.10(b-c) at VIS-NIR wavelengths and for angles of incidence that range from 0 to 90 degrees. Both TM and TE polarizations are considered. For TM electric field is launched along y-axis whereas for TE the electric field is launched along x-axis. The broadband reflectance switching given by the unpatterned semi-infinite structure is insensitive to the angle of incident light over a wide angular range of 50 degrees. Also, it is nearly equal for both TM and TE polarizations in this angular range. Several resonances typically present in grating structures are observable in the reflectance spectra. The sharp dips near  $750nm$  are typical Rayleigh anomalies associated with the excitation of grating modes, also known as guided mode resonances. The broader features at higher wavelengths are instead associated with Fabry-Pérot modes confined in the AlN layer. The resonances split for the incident angles greater than zero. Furthermore, the diameter and height of the nano-pillar were varied to study their effect on the optical response of the grating. These parameters were found to have no significant effect on the optical response of the grating under phase transition of  $VO_2$ .

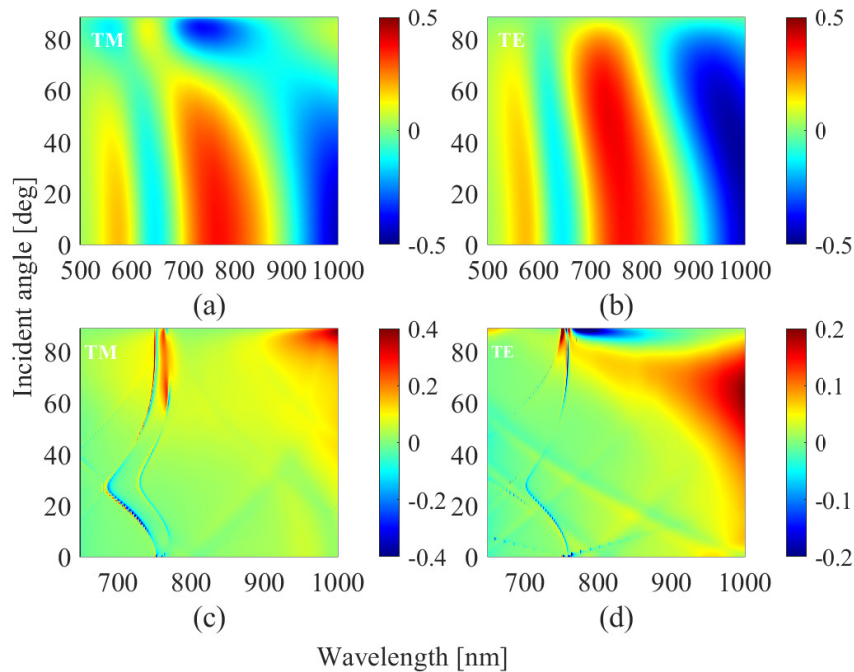


FIGURE 2.15: (a) Simulated delta-reflectance from an unpatterned semi-infinite structure (Fig.2.10(b)) covered with  $150nm$  thick  $VO_2$  film at VIS-NIR wavelengths for  $[0 - 90]$  degree incidence angle of the TM polarized incident light. (b) Same as in (a) for TE polarized incident light. (c) Simulated delta-reflectance spectra from grating covered with an ultra-thin ( $10nm$ ) film of  $VO_2$  at VIS-NIR wavelengths for  $[0 - 90]$  degree incidence angle of the TM polarized incident light. (d) Same as in (c) for TE polarized incident light.

### 2.3.4 Device fabrication

The step-by-step procedure of the nanopillar grating fabrication is elaborated in Fig.2.16. A Cu/AlN bilayer has been deposited by a DC magnetron sputtering technique on top of the  $\text{SiO}_2$  substrate. Then, a polymethyl methacrylate (PMMA) layer has been spin-coated over it. Finally, a silicon mold has been used to stamp an array of PMMA nanopillars using a nanoimprint lithography system [70]. The fabricated pillars array has a period,  $p = 600\text{nm}$ , and diameter of about  $250\text{nm}$ .  $\text{VO}_2$  nano-powders have been deposited by spin-coating on the pillars. Spin-coating of the alcoholic solution of  $\text{VO}_2$  nano-powder has been carried out at  $2000\text{ rpm}$  for  $40\text{ s}$  followed by sample heating at  $160^\circ\text{C}$  for  $10\text{ min}$  on a hot plate.  $\text{VO}_2$  nano-powders have been synthesized according to a sol-gel method, following the work of Choi et al. [85]. An SEM image of the fabricated nanopillar grating taken before the spin-coating of  $\text{VO}_2$  nano-powders is shown in Fig.2.17(a). An image of the pillar grating taken from the microscope objective is shown in Fig.2.17(b). The black dots correspond to  $\text{VO}_2$  nano-particle clusters. Figure2.18 shows the SEM of the nanopillar grating taken after the spin-coating of  $\text{VO}_2$  nano-powder.

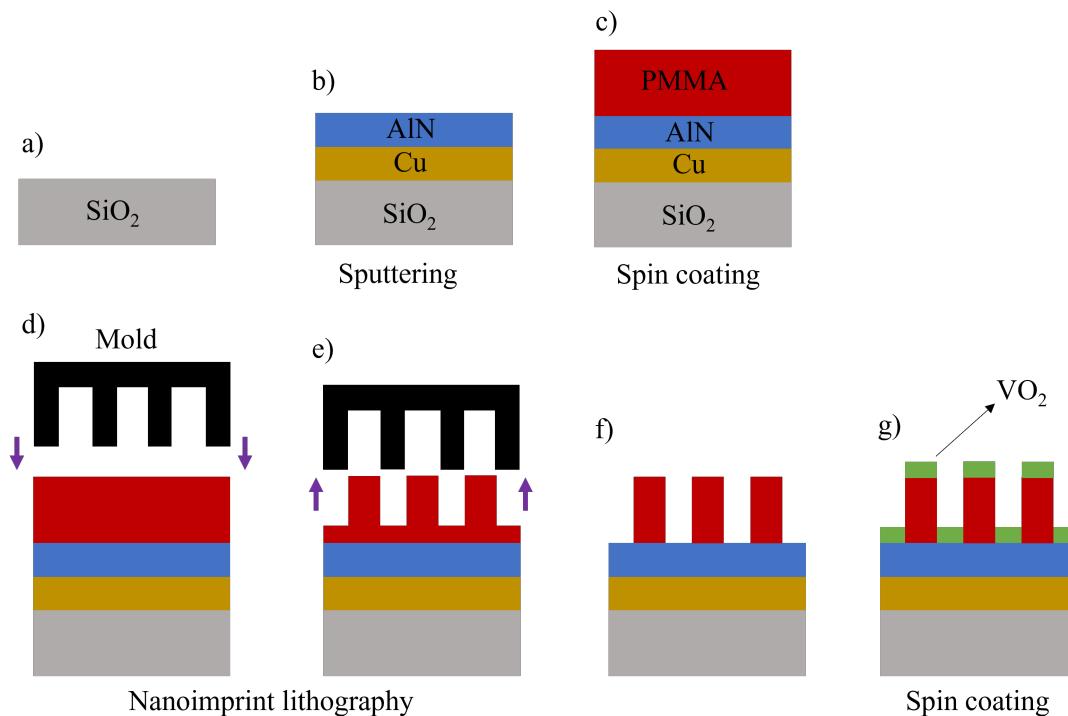


FIGURE 2.16: Schematic diagram of the steps involved in the fabrication process of a  $\text{VO}_2$  layer atop nanopillars. (b) Sputtering, (c) spin coating, (d-e-f) nanoimprint lithography and (g)  $\text{VO}_2$  nanoparticles spin coating.

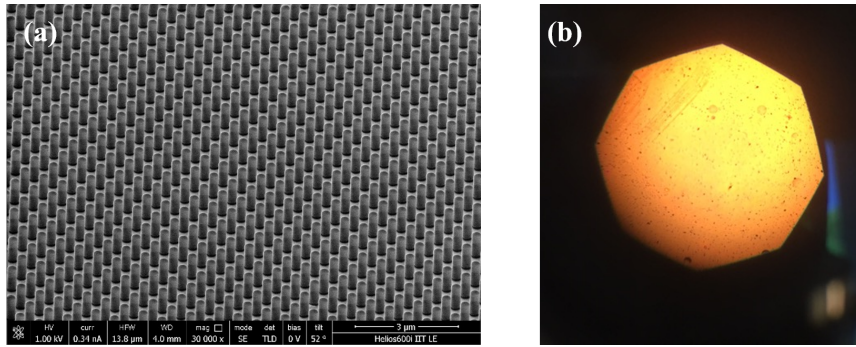


FIGURE 2.17: (a) An SEM picture of the fabricated nanopillar grating taken before the spin-coating of  $\text{VO}_2$  nano-powders [70] (b) An image of the pillar grating taken from the microscope objective. The black dots correspond to  $\text{VO}_2$  nano-particle clusters.

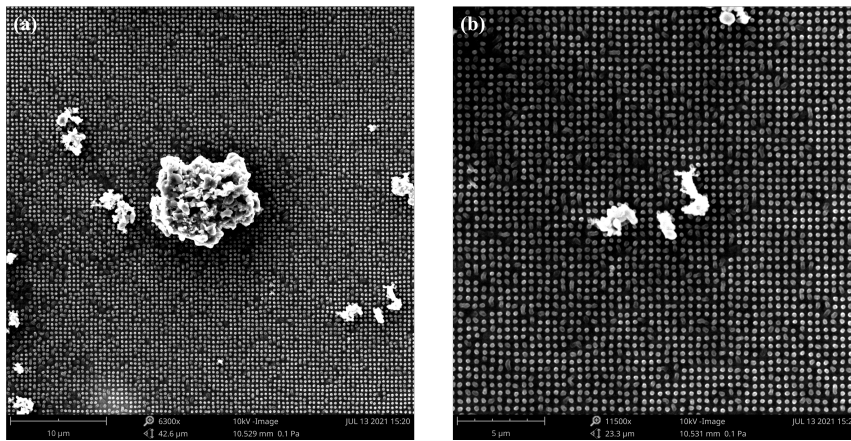


FIGURE 2.18: An SEM picture of the nanopillar grating taken after the spin-coating of  $\text{VO}_2$  nano-powder (a) at  $10\mu\text{m}$  scale (b) at  $5\mu\text{m}$  scale.

### 2.3.5 Device characterization

The experimental setup sketched in Fig.2.19 has been used to characterize the device. A broadband light source, filtered in the  $400\text{nm} - 700\text{nm}$  range, is focused on the sample through a low numerical-aperture infinity-corrected microscope objective ( $5x$ ,  $NA = 0.10$ ). The reflected light is collected by an aspherical fiber lens collimator. Finally, an optical spectrometer (HR4000 from Ocean Optics) connected through a multimode optical fiber records the spectra. The HR4000 has a 3648-element CCD-array detector with an optical resolution of  $1\text{nm}$  (FWHM) in the range of interest and provides an integration time of up to 65 seconds.

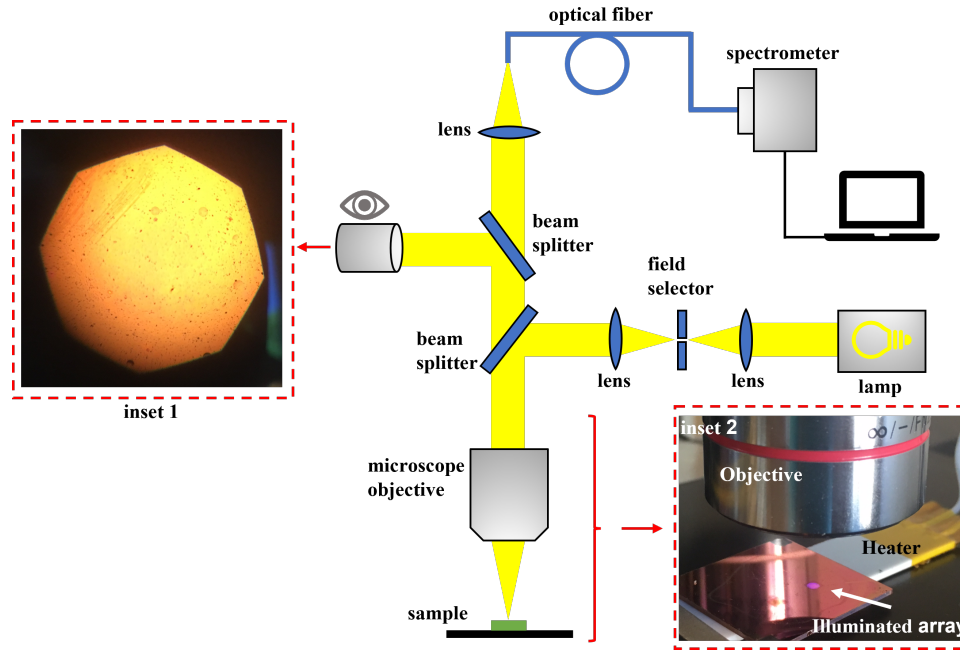


FIGURE 2.19: A sketch of the optical measurement setup. An optical image of the device as seen from the microscope (dots correspond to the  $\text{VO}_2$  NP clusters) is shown in inset 1. Inset 2 shows the heater used in the setup for sample heating.

In inset 1 of Fig.2.19, an image of the sample acquired by an optical microscope is shown. The black dots in the image correspond to the  $\text{VO}_2$  NP clusters. A heater (as shown in inset 2 of Fig.2.19) has been used to slowly increase the sample temperature from room temperature to  $80^\circ\text{C}$ . The data is recorded in a 6 minute measurement cycle in which the heater is turned on after one minute. It is kept on for the next three minutes and it was then turned off for the last two minutes. In this way, in one measurement cycle, the sample is heated above the phase transition temperature of  $\text{VO}_2$  ( $T_0$ ) and cooled down back to a lower temperature. The data are recorded at each second. Several measurement cycles are repeated to confirm the reversible nature of the reflectance tunability. The measured reflectance of the grating structure under normal incidence is shown in Fig.2.20. The reversible behaviour of the device reflectance under a thermal stimulus can be seen from the plots in Fig.2.20(a) taken at three different instants during a measurement cycle when the temperature is increased from room temperature ( $T < T_0$ ) to a value greater than the phase transition temperature ( $T > T_0$ ) and decreased back to room temperature ( $T < T_0$ ). To further illustrate the changes in the spectra, we show the colormap of the measured reflectance change ( $\Delta$ ) as a function of time in Fig.2.20(b), following a full cycle of transition from a low to a high-temperature state of the system and back from a high to a low-temperature state. The colour bar shows the change in the reflectance of the sample. Maxima and minima are observed above and below the resonant wavelength of  $\sim 600\text{nm}$ . It is also clear from the map that the device behaviour returns to the lower temperature state after the thermal stimulus is removed by turning off the

heater at 240 s. The dynamic behaviour of the temperature change is visible as well around the switching instants of 60 s and 240 s marked by the dotted white lines on the colormap.

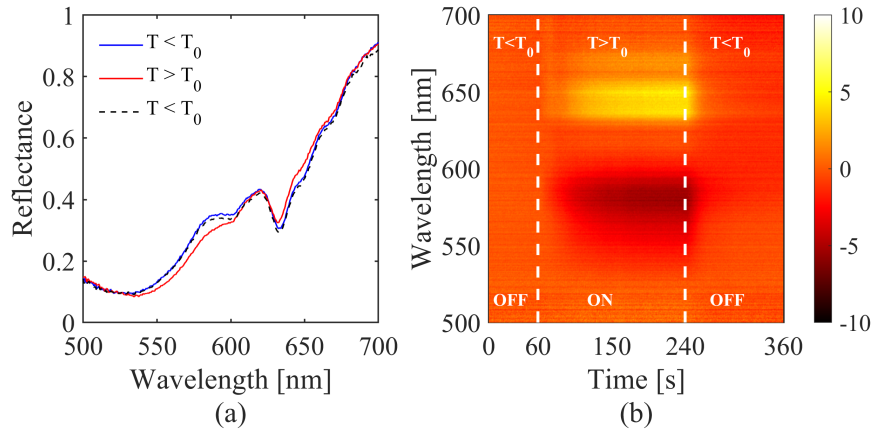


FIGURE 2.20: (a) Measured reflectance spectra of the device under a thermal stimulus at three different time instants when the temperature is increased from the room temperature ( $T < T_0$ ) to a value higher than the phase transition temperature of  $\text{VO}_2$  ( $T > T_0$ ) and decreased back to the lower temperature. (b) The colormap of the change in the measured reflectance during a full measurement cycle of 6 minutes.

The experiment-versus-theory comparison is shown in Fig.2.21. Dissimilarities between experimental results and theoretical calculations are due to the finite numerical aperture in the experiment, which limits the ability to resolve the very narrow spectral features predicted by numerical simulations. In the simulations, a plane-wave excitation is used, while in the experiment a cone of light of about  $12^\circ$  around normal incidence illuminates the grating.

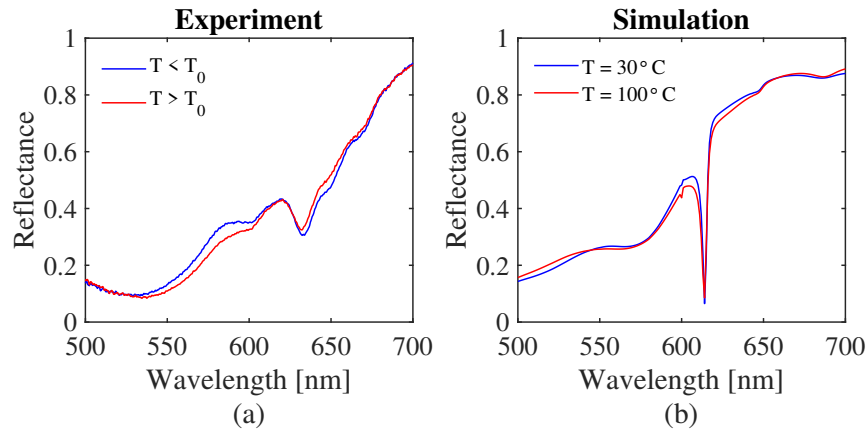


FIGURE 2.21: (a) Experimental reflectance from the grating at low temperature insulating phase ( $T < T_0$ ) and high temperature ( $T > T_0$ ) metallic phase. (b) Simulated reflectance from the grating at low temperature insulating phase ( $T < T_0$ ) and high temperature ( $T > T_0$ ) metallic phase.

### 2.3.6 Discussion

A resonant grating that includes a thin layer of phase-change material (vanadium dioxide) has been designed, fabricated, and characterized to achieve tunable optical response in the visible. Despite the inherently small perturbation introduced by the thin layer of vanadium dioxide, highly confined photonic modes are able to boost the optical sensitivity of the grating and improve the capability to modulate the optical response under the application of an external stimulus. The low and high temperature states of vanadium oxide are induced by mounting the sample on a thermal heater, demonstrating a 10% reflectance variation in the visible near  $600\text{nm}$ . For future investigations the behaviour of the sample will be tested by using a pump-probe excitation scheme, therefore with a fast, optical excitation that triggers the phase-change transition. Future work will be also dedicated to assessing the tunable properties of the structure at infrared wavelengths, where resonances are expected to be more significantly quenched by absorption losses introduced by the metallic phase of vanadium dioxide.

## Chapter 3

# Design of Plasmonic Gratings for Sensing and SERS Applications

### 3.1 Introduction to plasmonics

#### 3.1.1 Surface plasmon polariton

Surface plasmon polaritons (SPPs) are surface waves that are supported at an interface between a material with positive dielectric constant and a material with negative dielectric constant (that happens to be a metal). Due to their highly subwavelength nature and strong dispersive characteristics, they are hot research topic in the fields of optics and nanophotonic. They find numerous applications in sensors, microscopy, and bio-photonics.

The physical properties of the SPP are described in terms of their dispersion and spatial profile. Classical analysis of SPP using Maxwell's equations is described in great details in reference books on this topic. An excellent reference on this topic is the book by S.A. Maier [19]. The starting point for this analysis is the central equation of electromagnetic wave theory.

$$\nabla^2 \mathbf{E} - \frac{\epsilon}{c^2} \frac{\partial^2 \mathbf{E}}{\partial t^2} = 0 \quad (3.1)$$

Assuming small variation of  $\epsilon$  and under a harmonic time dependence of electric field, i.e.  $\mathbf{E}(\mathbf{r}, t) = \mathbf{E}(\mathbf{r})e^{-j\omega t}$ , it can be written as the well-known Helmholtz equation.

$$\nabla^2 \mathbf{E} - k_0^2 \epsilon \mathbf{E} = 0 \quad (3.2)$$

where  $k_0 = \omega/c$  is the free space wave vector.

Next, a simple 1D geometry (as sketched in Fig.3.1) of an infinite half space that is bounded at only one interface is assumed where equation (3.2) is solved separately in regions of constant  $\epsilon$  and solutions are obtained by matching proper boundary conditions. The wave propagates along x-axis whereas  $\epsilon$  varies only along z-axis. The interface is assumed at  $z = 0$ . Under these circumstances, the electric field can now be described as  $\mathbf{E}(x, y, z) = \mathbf{E}(z)e^{-j\beta x}$ .  $\beta$  is a complex number called the propagation constant of the travelling wave. This transforms equation (3.2) as:

$$\frac{\partial^2 \mathbf{E}(z)}{\partial z^2} - (k_o^2 \varepsilon - \beta^2) \mathbf{E}(z) = 0 \quad (3.3)$$

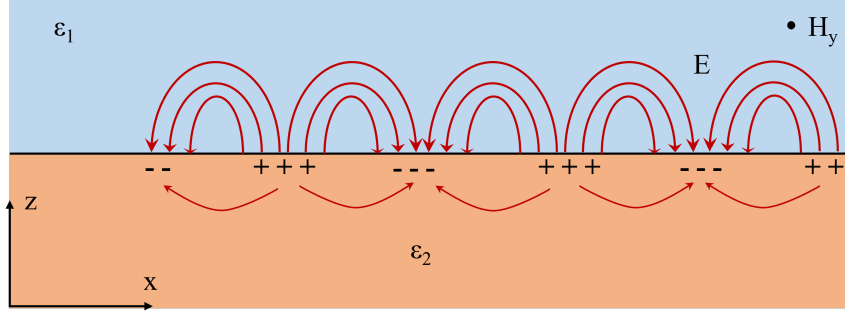


FIGURE 3.1: Sketch of a SPP propagation at a single interface between a metal and a dielectric.

Starting from Maxwell equations and assuming  $\frac{\partial}{\partial y} = 0$ , two sets of equations for two independent polarization modes (TM and TE) are obtained. SPP are not supported by TE mode as a surface wave can propagate only when the electric field is normal to the surface under non-zero boundary conditions. The TM mode (or p mode where only  $E_x$ ,  $E_z$  and  $H_y$  are non-zero field components) equations are written as:

$$\begin{aligned} \frac{\partial E_x}{\partial z} - j\beta E_z &= j\omega\mu_0 H_y \\ \frac{\partial H_y}{\partial z} &= j\omega\varepsilon_0 \varepsilon E_x \\ j\beta H_y &= -j\omega\varepsilon_0 \varepsilon E_z. \end{aligned} \quad (3.4)$$

Based on this wave equation for TM mode can be written as:

$$\frac{\partial^2 H_y}{\partial z^2} + (k_o^2 \varepsilon - \beta^2) H_y = 0. \quad (3.5)$$

Assuming an exponential field decay away along z-axis, the field solutions have the form,

$$\begin{aligned} H_i(z) &= H_{y,i} e^{j\beta x} e^{-k_i z} \\ E_x(z) &= E_{x,i} e^{j\beta x} e^{-k_i z} \\ E_z(z) &= E_{z,i} e^{j\beta x} e^{-k_i z} \end{aligned} \quad (3.6)$$

here  $i = 1, 2$  corresponds to region below the interface ( $z < 0$ ) and above the interface ( $z > 0$ ), respectively. The TM modes equations (3.4) can be solved by substituting the solution from (3.5). After imposing the boundary conditions, the dispersion

relation is obtained. The general dispersion relation for the  $i^{\text{th}}$  medium is written as follows:

$$k_0^2 \mu_{o,i} \varepsilon_i = \beta^2 - k_i^2. \quad (3.7)$$

The continuity of the field at the interface implies the following condition also known as the existence condition for SPP.

$$\frac{\varepsilon_1}{k_1} + \frac{\varepsilon_2}{k_2} = 0 \quad (3.8)$$

Equations (3.7) and (3.8) are combined to obtain a generalised expression for the dispersion relation.

$$\beta = k_0 \sqrt{\left( \frac{\varepsilon_1 \varepsilon_2}{\varepsilon_1 + \varepsilon_2} \right)} \quad (3.9)$$

The permittivity  $\varepsilon_1$  and  $\varepsilon_2$  in the above expression can have a real or complex values.

As discussed in chapter 1, metals lose their metallic character above the plasma frequency  $\omega_p$  as the real part of the permittivity of a metal becomes positive and eventually attains a value of unity far beyond the plasma frequency. Assuming a negligible damping factor, the  $\varepsilon_2$  can be written as using the Drude model.

$$\varepsilon_2 = 1 - \frac{\omega_p^2}{\omega^2} \quad (3.10)$$

By substituting this equation into the dispersion relation for SPP and taking a limit  $\beta$  approaches infinity, an expression for surface plasma frequency is obtained.

$$\omega_{sp} = \frac{\omega_p}{\sqrt{1 + \varepsilon_1}} \quad (3.11)$$

This sets an upper limit for the SPP frequency.

### 3.1.2 Excitation of surface plasmon

As discussed above the SPP are electromagnetic waves that propagate along the metal-dielectric interface with a propagation constant of  $\beta$ . Since the value of projection of wavevector in dielectric ( $k_x = k \sin \theta$ ) is always smaller than  $\beta$  special phase-matching techniques are required to excite SPP.

One of the most common techniques to excite SPP is the prism-based coupling technique. A three-layer system is used where the metal layer is sandwiched between two dielectric layers. One dielectric layer can be air ( $\varepsilon = 1$ ). The other dielectric layer, that is usually in the form of a prism, should have higher dielectric constant  $\varepsilon$ . When light impinges the dielectric-metal interface under total internal reflection condition at an angle  $\theta$ , metal gets an in-plane wavevector  $k_x = k \sqrt{\varepsilon} \sin \theta$  that is greater than  $\beta$  and can excite a SPP at metal-air interface. The excitation of SPP is detected as a sharp dip in the reflected light. The prism-based coupling scheme is

also known as attenuated total reflection. Two different geometries for prism-based coupling, depicted in Figs.3.2(a-b), are known as Kretschmann configuration and Otto configuration, respectively. In Kretschmann configuration a thin metal film is placed on top of a glass prism while in the Otto configuration there is a small air gap between the prism and metal film.

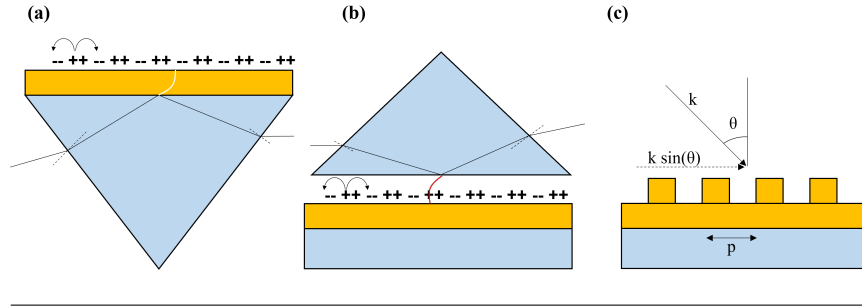


FIGURE 3.2: (a) A sketch of the Kretschmann configuration for SPP coupling (b) A sketch of the Otto configuration for SPP coupling (c) A sketching showing phase-matching condition of light to SPP using a 1D grating.

SPP can also be excited by using a grating. The reciprocal lattice vectors of the grating can fulfil the phase-matching condition by providing the missing momentum. The grating can be realised by patterning the metal surface with a lattice of slits or holes. A one-dimensional array of slits is shown in Fig.3.2(c). Phase-matching condition is established whenever the following condition is fulfilled.

$$\beta = k \sin \theta \mp m \frac{2\pi}{p} \quad (3.12)$$

where  $p$  is the lattice constant and  $m$  is an integer. With grating coupling the excitation of SPP is also detected as a sharp dip in the reflected light. In case of a grating, the reverse process is also possible when a SPP propagating along a surface encounters a grating and can couple to light and radiate.

### 3.2 FIB milled 2D array of plasmonic nanoplatelets

The emergence of lab-on-fiber platforms has revived the interest in the fabrication of sub-wavelength periodic nanostructures on unconventional substrates, such as the tip of an optical fiber. In this context, Focussed Ion Beam (FIB) milling provides for a versatile approach to prototype photonic structures and metasurfaces with a limited number of fabrication steps [86, 87, 88]. FIB milling inherently generates sub-20 nm gaps and results in tapered grooves.

In this work, a 2D array of gold nanoplatelets has been designed, fabricated and characterized [17], [89]. It is shown that FIB milling inherently generates sub-20-nm gaps. Numerical models of the grating structure employing RCWA and FDTD methods have been developed to model a periodic array of the nanoplatelets as well

as a finite subset of the array with limited number of grating elements. The effect of the gap morphology on the array optical properties have been studied, and it is experimentally and numerically demonstrated that illuminating a subset of elements on the array generates multiple spectral features in the reflection and transmission spectra. As a possible application, the array performance in the detection of refractive index (RI) changes has been investigated.

### 3.2.1 Device fabrication and measurements

Nanoplatelets arrays are milled in a gold film (180 nm-thick) deposited by electron beam deposition on a quartz microscope coverslip (Ted Pella). A 5 nm thick layer of Cr is used to promote adhesion between gold and quartz. The arrays are realized by milling thin slits of metal with a Ga<sup>+</sup> FIB system (FEI dual-beam Helios-NanoLab600i, beam current 7.7 pA, voltage 30 kV). The beam is sequentially scanned in the two milling directions (from edge to edge), Horizontal (H) and Vertical (V), with minimal line overlap (5 – 10%). The design is shown in Fig.3.3(a). The array morphology was characterized by Scanning Electron Microscopy (SEM). As shown in Fig.3.3(b), the combination of the edge effect and the redeposition of sputtered material produced gaps approaching 10 nm in width at the platelet's corners.

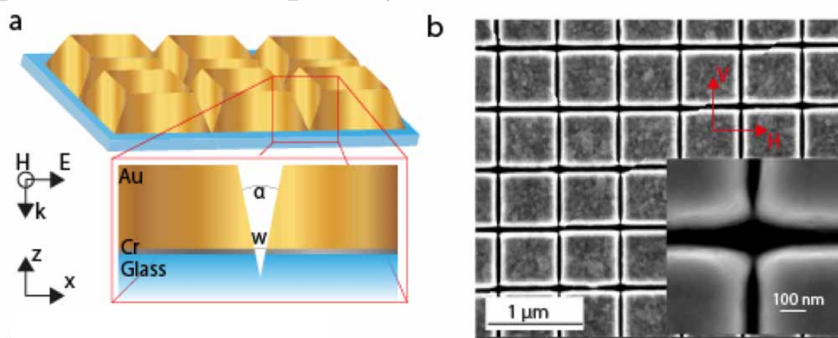


FIGURE 3.3: Design of nanoplatelet array with a close-up of the tapered groove extending into the substrate. (b) An SEM picture of an array [17] with  $P = 630\text{nm}$ . The inset shows a zoom on the nanoplatelets corner, with a gap width approaching 10 nm.

The spectral response is measured for arrays with reversed milling order  $A_1(B_1)$  starting from the V direction, and  $A_2(B_2)$  starting from the H direction. The milling order influences the orientation of the narrow gaps at the NP corners (Figs.3.4(a,d)). The reflectance and transmittance spectra show that the gap morphology influences the array performances depending on the polarization of incoming light. Resonance signatures are recognizable in the spectra for both devices (Figs.3.4 (b-c) and (e-f)). Besides a grating state sharp peak at the array periodicity (indicated as II), a blue-shifted peak (I) and a broad, red-shifted resonance (III) are also observed for both A and B arrays. The dip, indicated as III, is a hybrid state related to the availability of a Fabry-Pérot mode inside the cavity which propagates in the metal-insulator-metal

TABLE 3.1: Measured geometrical parameters of the fabricated nanoplatelets arrays.

Device	Period (nm)	Gap (nm)	Width (nm)	Gold thickness (nm)
$A_1$	550	32	103	180
$A_2$	550	32	67	180
$B_1$	630	32	103	180
$B_2$	630	32	67	180

(MIM) waveguide. The presence of the MIM waveguide is responsible for the high transmission in Figure 3.4. A maximum of  $\sim 10\%$  transmittance has been measured.

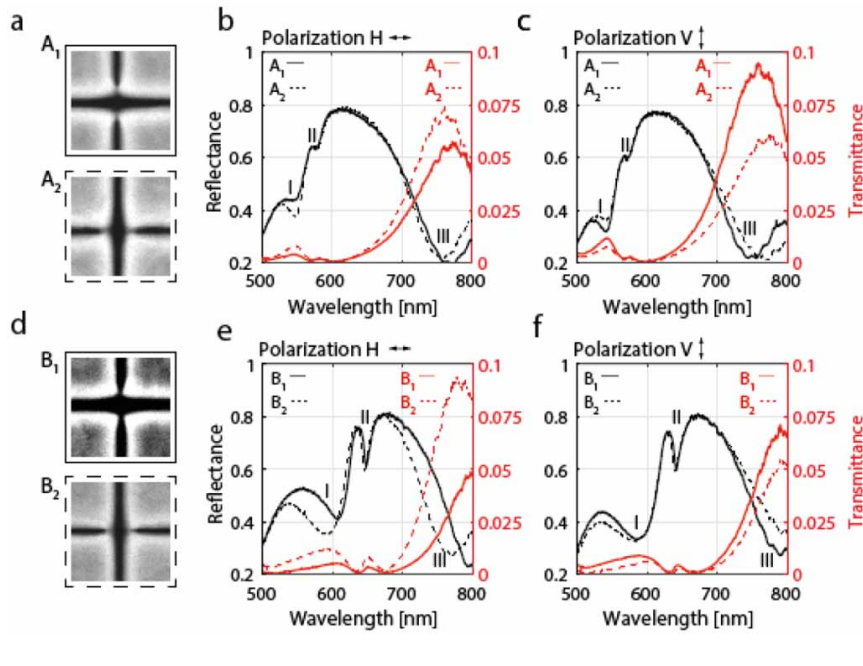


FIGURE 3.4: (a) Nano-gap orientation in array  $A_1$  and array  $A_2$ , milled at period  $P_A = 550\text{nm}$  with V-H and H-V order, respectively [17]. (b) Reflectance (black) and transmittance (red) spectra for  $A_1$  (solid line) and  $A_2$  (dashed line) for H-polarized light. (c) As in (b) for V-polarized light. (d) Nano-gap orientation in array  $B_1$  and array  $B_2$ , milled at period  $P_B = 630\text{nm}$  with V-H and H-V groove order, respectively. (e) As in (b) for  $B_1$  and  $B_2$  arrays. (f) As in (c) for  $B_1$  and  $B_2$  arrays.

### 3.2.2 Numerical Modelling

To describe the physical origin of the measured spectra, a numerical model of the FIB-milled NP-arrays has been developed. The nano-platelets have been modelled with trapezoidal gold patches placed on top of the glass substrate, following Fig.3.3(a). The 2D sketch of the gold nanoplatelets grating is shown in the Fig.3.5(a).

The measured geometrical parameters of the fabricated devices are detailed in Table 3.1. The gold platelets have trapezoidal shape. The tapered grooves have the

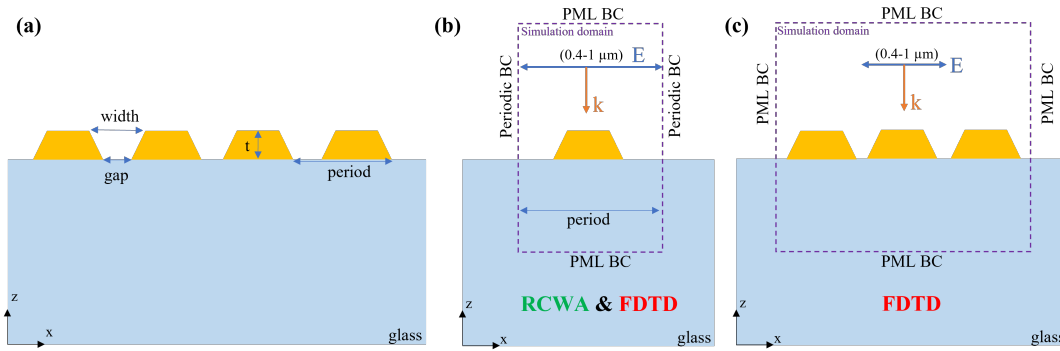


FIGURE 3.5: (a) 2D Sketch of the gold nanoplatelets grating (b) A sketch of a unit cell of the periodic array simulated as a periodic structure using RCWA and FDTD methods (c) A sketch of a finite subset of the periodic array simulated FDTD method.

dimension, called gap, of  $32\text{nm}$  at the floor (glass-gold interface) in both horizontal and vertical directions. At the ceiling (gold-air interface) the grooves dimensions (called width) are  $103\text{nm}$  and  $67\text{nm}$  in horizontal and vertical directions respectively. The thickness of gold platelets is set equal to  $180\text{nm}$ .

First, a periodic structure is considered by using periodic boundary conditions along  $x$  axis and absorbing boundary conditions along  $z$  axis in  $xz$  plane as sketched in Fig.3.5(b). Two different simulation techniques namely finite difference time domain method (FDTD) and rigorous coupled wave analysis method (RCWA) are used for simulations. For gold Drude-Lorentz model, described in Chapter 1 section 1.2.3, has been used. Figure 3.6 shows the reflection and the transmission spectra of the periodic grating structure. The V grating state can be observed in the spectra. However, compared to the measured results of Fig.3.4, the simulation results shown in Fig.3.6 do not show a dip around  $600\text{nm}$ .

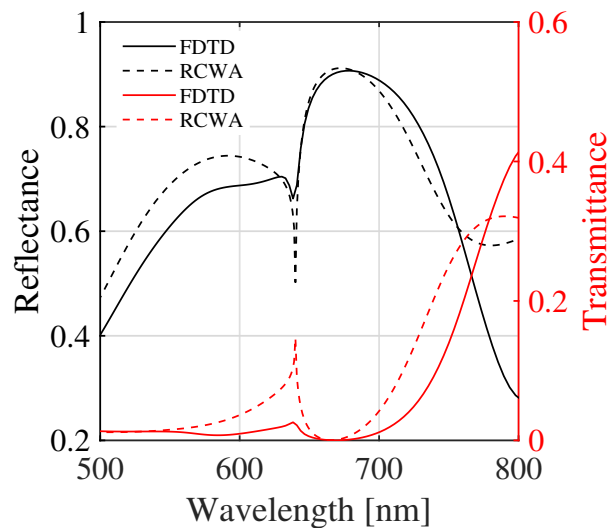


FIGURE 3.6: Reflectance and transmittance spectra for device  $B_1$ .

RCWA simulations for the infinite structure revealed that the spectra are based on contributions from all the grating orders ( $0, \pm 1$ ). This means the first dip is due to missing diffraction orders  $\pm 1$ . This is because the experimental setup exploits a spot that illuminates a finite number of NPs. Hence, under normal incidence, the higher diffracted orders could not be collected by the lens.

In order to match the experimental setup, a finite grating structure as sketched in Fig.3.5(c) has been simulated. A 2D FDTD model of the grating employing absorbing boundary conditions in all four directions in the  $xz$  plane is used. The grating structure is illuminated by a normally incident Gaussian pulsed source with a Gaussian spatial profile (TM polarization, electric field along the  $x$ -axis) centered at  $600nm$ . Figures 3.7(b-c) show the numerical reflectance and transmittance spectra when the Gaussian illumination covers 20 NPs (beam waist equal to 10 periods). As it can be inferred from the plot, when considering a finite-size device, the shape and features of the simulated spectra match the experimental results and a second dip (II) emerges at the blue side of the reflection spectra for both arrays A ( $p = 550nm$ ) and B ( $p = 630nm$ ). In particular for arrays B, FDTD simulations confirm that the first dip (I) is due to the first-order diffraction that is not collected in the experimental setup. It can be further observed from Fig. 3.7(d) that under increasing width of the illuminating beam waist from 5 to 40 periods, dip (I) is red-shifting and decreasing in intensity eventually matching the results for an infinite structure. Conversely, the dip (II) is blue shifted and moves towards  $\lambda = p$  as for the infinite structure (Fig.3.7(a)).

To fully account for the effect of variations in the NP geometry, the reflectance and transmittance spectra are studied while varying the array period and the gap size. As expected, a variation of the array periodicity shifts all the spectral features consistently (Fig.3.7(e)). On the other hand, an increase on the gap size (Fig.3.5) from 0 to  $50nm$ , only the magnitude and position of the dips around  $600nm$  (I) and  $800nm$  (III) (Fig.3.7(f)) are altered. This can explain the small difference in the position of the peaks in the range  $750 - 800nm$  in the experimental spectra. Overall, these numerical results confirmed hypothesis, since simulations are in very good agreement with the measurements.

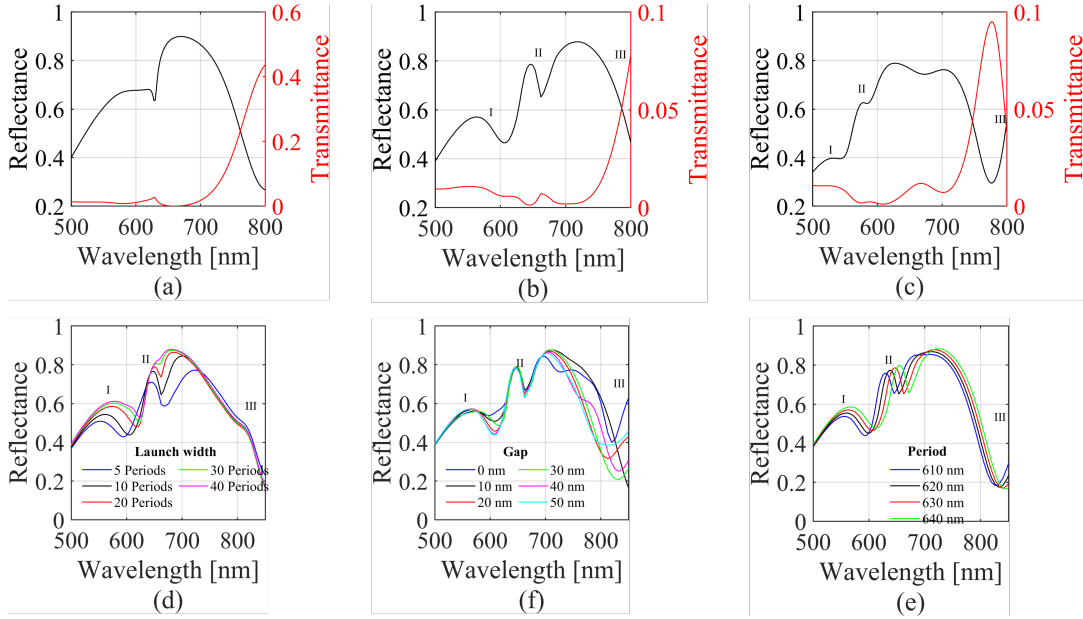


FIGURE 3.7: (a) Reflectance (black) and transmittance (red) spectra for infinite arrays of gold NPs, with periodicity  $p = 630\text{nm}$  calculated with FDTD method. (b) FDTD simulation of reflectance (black) and transmittance (red) for a normally incident Gaussian beam pulse with a Gaussian spatial profile (TM polarization, centered at  $600\text{nm}$ ) (c) As in b for  $p = 550\text{nm}$ . (d-e-f) Effect of the variation of the illumination beam waist (d), of the array periodicity (e) and of the bottom gap size  $w$  (f) on the reflectance spectrum.

### 3.2.3 Sensing performance

The performance of the NP array as a refractive index sensor has been predicted by the numerical simulations and validated by the measurements. For this purpose, the NP array with  $p = 630\text{nm}$  covered in a thin layer ( $3\mu\text{m}$  thick) of distilled water ( $RI = 1.33$ ) and isopropyl alcohol (IPA) ( $RI = 1.37$ ) is simulated. Fig.3.8(a) shows that the reflection dip from IPA covered grating is red shifted when compared to the reflection dip from water covered grating. Figure 3.8(b) shows the measured reflectance spectra with NP array immersed in distilled water (blue dots) and IPA (red dots). Blue and red lines are obtained by interpolating the data with second order Fourier series. Similarly, sensing performance has also been tested based on the transmitted light by using the extra ordinary transmission (EOT) properties of the NP array. The numerical and experimental transmittance from the NP grating covered with water and IPA are shown in Fig.3.8(d) and (e), respectively. The values of numerical as well as experimental sensitivity ( $S$ ) and figure of merit (FOM) are given in the Table 3.2 for both reflection and transmission domains. These values are consistent with the literature on similar sensor architectures [90]. The sensitivity is defined as shift in the resonant wavelength per refractive index unit (RIU). The FOM is calculated by dividing the sensitivity by the full width at half maximum (FWHM) value of the resonance dip. Alternatively, Dark Field (DF) microscopy is

TABLE 3.2: Simulated and experimental values of the sensitivity and FOM for both reflection and transmission domains.

Domain	Simulated		Experimental	
	S (nm/RIU)	FOM (1/RIU)	S (nm/RIU)	FOM (1/RIU)
Reflection	500	10	$622 \pm 134$	7
Transmission	575	36	425	25

used to image the NP array immersed in air or IPA. The acquired DF images with the sample covered in air and in IPA are shown Fig. 3.8(c).

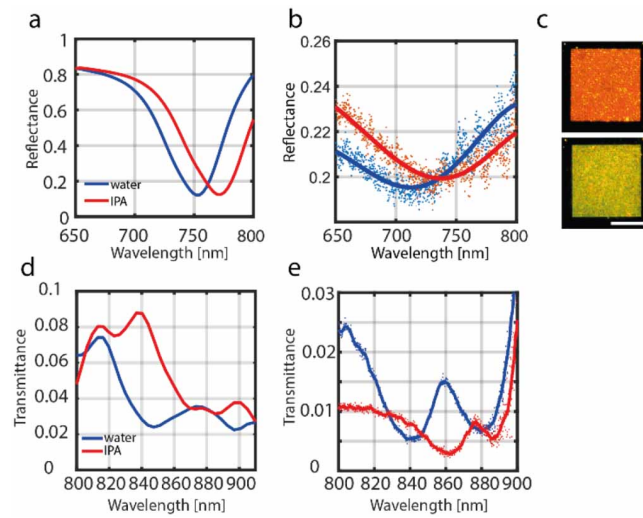


FIGURE 3.8: (a) Simulated reflectance when a thin film of distilled water (blue line) or isopropylic alcohol (red line) covers the NP array. (b) Reflectance spectra measured with the array immersed in distilled water (blue dots) or IPA (red dots). (c) Dark field images of a NP array with periodicity  $p = 550\text{nm}$  covered in air (top) or IPA (bottom). Scale bar is  $15\mu\text{m}$ . (d) As in (a) for transmitted light (e) (d) As in (b) for transmitted light.

In conclusion, a comprehensive experimental and theoretical description of the combination of plasmonic and diffractive effects in finite, 2D arrays of NPs with sub-20 nm gaps fabricated with Ga FIB milling has been provided. A high optical transmission (approaching 10%) has achieved by illuminating a subset of the array (20 elements). The sensing performance of the NPs array has been demonstrated both using the reflected and transmitted light.

### 3.3 Plasmonic nanostructures on curved surface

#### 3.3.1 State of the art and recent developments

Surface plasmon polaritons (SPP) or Surface plasmon resonances (SPR) are longitudinal electromagnetic waves that exist at the boundary of a metal and a dielectric medium. These waves originate due to the resonant interaction of electromagnetic fields of a light wave with the free-electron plasma of metal [14]. Apart from other unique properties of nonradiative bound nature, extremely short wavelengths, and strong near fields, the SPP modes are highly sensitive to changes in the refractive index of the surrounding media. This has been exploited to develop plasmonic sensors for chemical, biological, and biomedical applications. With the recent advances in nanofabrication techniques, several challenges in the design and fabrication process have been addressed and considerably growing research interest has been observed in this field [91]. Plasmonic sensors have been studied and realized on several different platforms including planar glass and silicon substrates [13], [92, 93, 94], prisms [95], and optical fibers [96].

In addition to the planar platforms, plasmonic devices on curved and flexible surfaces can open exciting new possibilities for the next generation of optical devices with new functionalities. Propagation on curved surfaces can be designed to mimic optical fiber-based plasmonic devices, for example, advanced optical probes for biological sensing applications [97, 98]. A new term has been coined in this regard called "Lab on Fiber". Optical fibers have widely been used as light guiding devices, especially for the telecommunication industry. The ability to fabricate nanostructures on the optical fiber or near the tip of the optical fiber can bring breakthroughs in the field of medical diagnostic and bio-sensing. Considerable development has been made in fabrication technologies to realize sub-wavelength plasmonic structures on curved and flexible surfaces [99, 100, 101, 102]. This, as a result, has expanded the applicability of optical fiber for a new class of devices that involve nanostructures incorporated with optical fibers to confine and manipulate light at the nanoscale [103].

The implications and challenges related to curved space plasmonic devices have been addressed in both theoretical and experimental domains to explain and physically understand the curvature induced optical effects [104, 105]. In recent work, Danveer Singh et al., have experimentally demonstrated the guiding and focusing of the plasmonic beam in curved space plasmonic devices [106]. In the context of plasmonic devices on curved surfaces, it is necessary to understand the fundamental properties of SPP around curved surfaces. Surface curvature seems to have diminishing effects on the propagation of SPP. For example, Jiunn-Woei Liaw et al. described that in comparison to a planar surface, the attenuation constants of SPP on a curved surface are larger due to the radial radiation of the wave energy into the surrounding medium [107]. Similarly, Keisuke Hasegawa et al. analyzed SPP propagating around bends and explained that the curvature leads to the distortion of the

phase fronts causing the fields to radiate energy away from the metal-dielectric interface [108]. The adverse curvature effects can be more prominent for highly curved surfaces where curvature radius is in the range of a few hundred microns or less. In another theoretical study, Hyunwoong Lee et al. simulated a  $50\text{nm}$  thick layer of gold on a curved glass substrate for both convex and concave curvatures. They studied the effect of curvature radius on SPR and concluded that the higher curvature tends to decrease resonance shift of plasmonic modes and broadens the resonant characteristics which could lead to performance degradation of plasmonic devices built over curved surfaces [109].

Nanofabrication is a complicated and expensive process even on the planar substrates. The curved space devices pose further changes making it more challenging. Therefore, in the framework of curved space plasmonic devices, the development of accurate numerical simulation models for design and analysis is an important aspect. In the following, plasmonic nanostructure on a curved surface, which could mimic a real device built upon an optical fiber, have been investigated through numerical simulations. Curvature induced effects on the plasmonic features have been studied. Tapered optical fibers that have a typical diameter of fewer than 100 microns can be thought of as a highly curved surface.

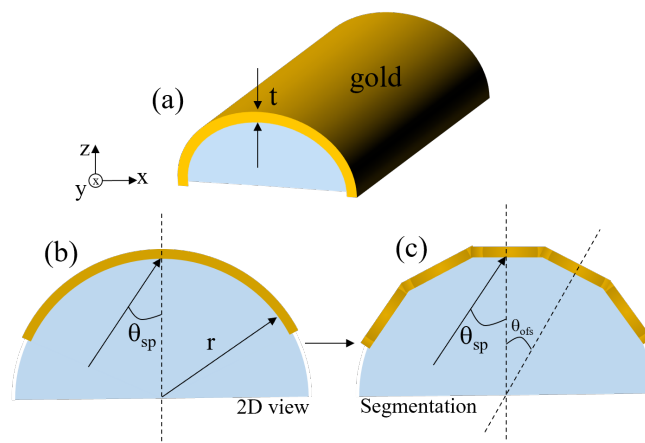


FIGURE 3.9: (a) A sketch of a continuous layer on a curved cylindrical substrate. (b) a 2D view of the geometry. (c) a 2D view with segmentation of the curved surface.

Fig.3.9(a) shows a cylindrical glass substrate of curvature  $r$  coated with a gold layer of thickness  $t$ . A planar structure approximation technique is used to numerically simulate the curved structure [109, 110]. Since the structure is homogeneous along  $y$ -axis, a 2D geometry as depicted in Fig.3.9(b) has been used for numerical simulations. Numerical simulations are performed using the RCWA method which is a Fourier-space technique to solve scattering from periodic structures. The refractive index of glass is taken as 1.5. For the optical constants of gold, Johnson and Christy data has been used [21]. It is assumed that all reflected light is collected

and superposed. The collected light can be quantized by the following relation in equation 3.13.

$$R(\lambda) = \frac{1}{N} \sum_i^N R_i(\lambda, k_i) \quad (3.13)$$

$$\theta_{in} = \theta_{sp} \pm \theta_{ofs} \quad (3.14)$$

Where  $N$  is the total number of segments and  $k_i$  is the wave vector of light beam incident at the  $i^{th}$  segment.  $R(\lambda)$  is the total reflection spectra which are averaged discrete sum of individual transmission spectra from each segment.  $\theta_{sp}$  is the angle at which momentum matching takes place and a surface plasmon is excited. This angle can be calculated by RCWA a simulation. A map of the reflection spectra for the  $50nm$  gold layer on the glass substrate is shown in Fig.3.10(a) when the light incidence angle is varied from  $0^\circ$  to  $70^\circ$ . It can be observed from Fig.3.10(b) that the coupling occurs at  $37^\circ$  and  $55^\circ$  for air and water backgrounds, respectively. Under normal light incidence, light wave vectors strike at each segment at a different angle depending upon the geometrical position of a segment for a given radius of curvature (Fig.3.9(c)). These are called the offset angles ( $\theta_{ofs}$ ). These angles can be added or subtracted from the light wave vector angle  $\theta_{ofs}$  on a planar substrate to account for the curvature effects. This approximates the spectra obtained by an actual curved substrate.

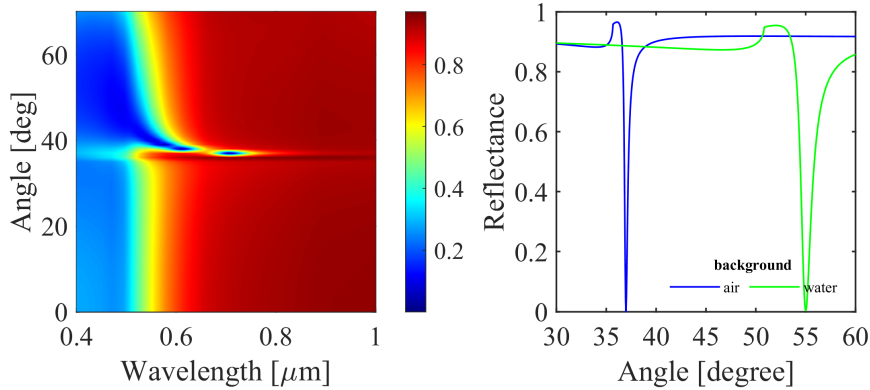


FIGURE 3.10: (a) Reflectance map for a  $50nm$  gold as the light incident angle is varied from 0 to 70 degrees. (b)  $\theta_{ofs}$  deduced when the background is air ( $37$  degrees) and water ( $55$  degrees).

Fig.3.11(a-c) shows the reflectance spectra for three different thicknesses of the gold layer equal to  $30nm$ ,  $50nm$ , and  $70nm$ , respectively. It can be observed from the spectra that with increasing curvature the sharp spectral features disappear. This is because of the large attenuation of the plasmonic waves along the curved surface.

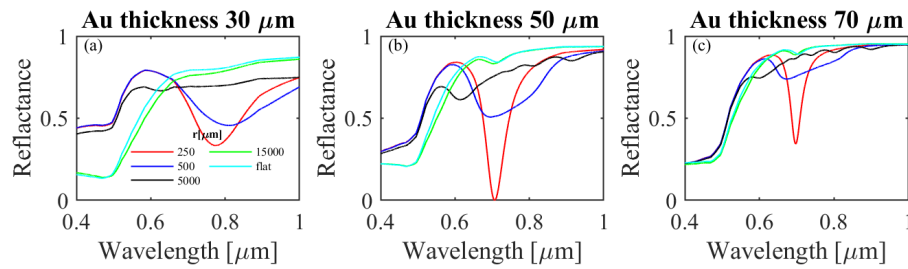


FIGURE 3.11: (a) Reflectance spectra for a 30nm gold layer when the curvature radius is changed from 250 $\mu\text{m}$  to a flat surface. (b) same as (a) for 50nm gold layer (c) same as (a) for a 70nm gold layer.

### 3.3.2 Segmented-wave analysis of plasmonic grating on a curved surface

The plasmonic grating on a cylindrical glass substrate under investigation is shown in Fig.3.12. The grating has a period ( $p$ ) of 630nm with a slit width ( $w$ ) of 100nm. The thickness of the gold layer is set as 130nm.

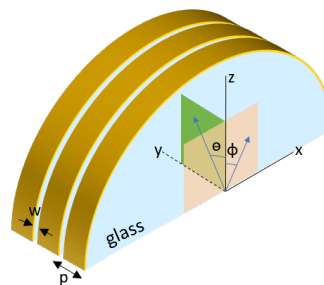


FIGURE 3.12: A sketch of the gold nano-grating on a cylindrical glass substrate.

A segmentation-based approximation technique is used to numerically simulate the curved structure. The light wavevectors propagate along the cylinder axis which is represented by the angle theta ( $\theta$ ) in  $yz$  plane whereas the angle phi ( $\phi$ ) represents the tilt of wavevectors along the surface curvature in the  $xz$  plane (Fig.3.12). Numerical simulations are performed using an FDTD model. A 2D view of the curved structure is depicted in Fig.3.13. A curvature radius of 5  $\mu\text{m}$  is used in the simulation model. Each strip of the curved grating has an arc length  $L$  which is fixed as 4.166 $\mu\text{m}$ .

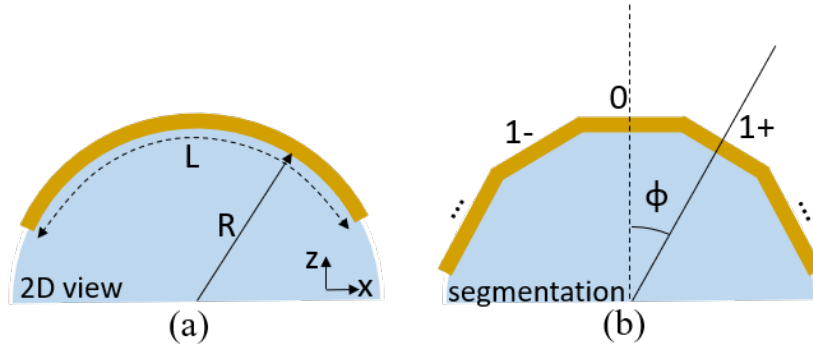


FIGURE 3.13: (a) A 2D view of the geometry (b) A 2D view with segmentation of the curved surface.

The proposed approach starts by dividing the gold strip into  $N$  planar segments where each segment is located at a different geometrical position as shown in Fig.3.13(b). The segment index  $n$  varies from  $-(N-1)/2$  to  $+(N-1)/2$ , where  $N$  is an odd number. If  $\alpha(L/R)$  represents the angle subtended by the total arc length considered, the angle  $\alpha$  for each segment is given, as in:

$$\phi_n = n \frac{\alpha}{N} \quad (3.15)$$

For the analysis,  $N$  has been assumed as 11. Each segment is simulated by a 3D model under TM polarized plane wave excitation at visible and NIR wavelengths ( $\lambda = 400 - 1000nm$ ). The source is in the glass substrate whereas the transmission monitor is placed on the top of the grating structure in air. PML boundary conditions are used in both  $x$  and  $z$  directions while a periodic boundary condition is used along the  $y$ -axis. The angle  $\phi$  ( $\phi$ ) is fixed as calculated by equation (3.15) and the angle  $\theta$  ( $\theta$ ) is fixed equal to 0 degree. The resulting transmittance spectra of  $N$  segments is quantized as described by the relation under the assumption that all the transmitted light is collected and superposed as follows:

$$T(\lambda) = \frac{1}{N} \sum_n^N T_n(\lambda, k_n) \cos \phi_n \quad (3.16)$$

where  $N$  is the total number of segments and  $k_n$  is the wave vector of light beam incident at the  $n$ th segment.  $\phi_n$  represents the incident angle at  $n$ th segment. Cosine of  $\phi$  accounts for the reduction in the effective area due to the curvature.  $T(\lambda)$  is the total transmittance which is averaged discrete sum of individual transmittance spectrum from each segment. Results in Fig.3.14 show the transmittance spectra from 6 planar segments under normal incidence ( $\theta = 0$ ) when  $\phi$  is varied. Each segment is located at a different geometrical position determined by the angle  $\phi$  ( $\phi$ ). The spectra are shown only for the positive angles for simplicity as the results are similar for negative angles due to the symmetry of the nanostructure as evident from Fig.3.13(b).

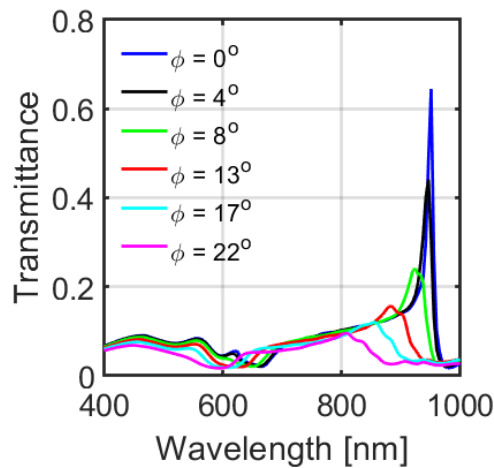


FIGURE 3.14: Transmittance spectra from segments when angle  $\phi$  is varied in the  $xz$  plane.

The total transmittance spectra obtained using equation (3.16) is shown in Fig.3.15 as solid line. To validate the results from the segmentation-based technique, the actual curved structure has been simulated by using a 3D FDTD model. The results for the curved structure are shown in Fig.3.15 as dashed line. There is reasonably good agreement between the results from two methods when a scaling factor of 1.6 is applied to the segmented-wave approximation result.

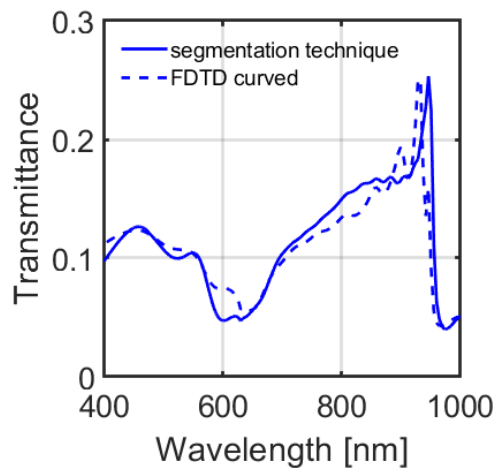


FIGURE 3.15: Total transmittance spectra obtained by segmentation-based technique (solid line) and by the 3D FDTD curved model (dashed line).

It is possible to conclude that a gold nano-grating on a curved surface has been analysed through a segmented-wave approximation technique as well as by a 3D FDTD model of the curved grating. The results from both the techniques show a

good agreement. This is a good starting point to further extend this segmentation-based technique to simulate complex structures especially on curved structures - for example, an optical fiber - to reduce the simulation time and computational load.

### 3.4 Spectrally tunable curved plasmonic grating on tapered optical fiber

#### 3.4.1 Grating emission spectra

Figure 3.16(a) illustrates the geometrical shape of the curved grating on a tapered optical fiber. Assuming a slow varying taper, the grating structure can be considered as shown in inset. The glass cylinder has a curvature radius  $R$ . The gold strips have a length  $L$  along the cylinder curvature.  $L$  refers to the size of the fiber window. The slits in between two gold strips have a width  $w$ . The gold layer has a thickness  $t$ . The grating has a period  $p$ .

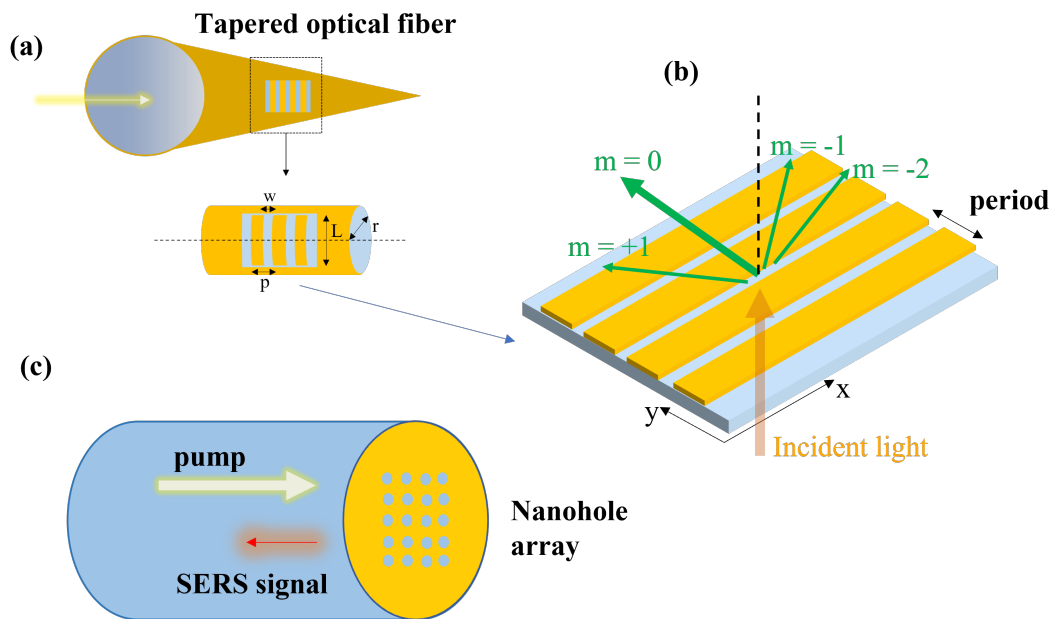


FIGURE 3.16: (a) A sketch of a curved plasmonic grating on gold coated tapered optical fiber. The inset shows the grating on uniform cylindrical glass substrate assuming a slow varying taper (b) A sketch of the gold grating on a planar glass substrate showing diffracted orders in the transmission domain under an excitation from the glass substrate (c) A sketch of an array of nanoholes on the end facet of an optical fiber. The end facet is coated with a gold layer.

For the emission spectra calculations, the curved grating has been approximated with a planar grating. The sketch of the planar gold grating on the glass substrate is shown in Fig.3.16(b). Diffracted angle of a particular diffracted order is calculated by the grating diffraction equation at a given wavelength and angle of the incident light in the transmission domains.

Three different fabricated periodicities –  $630\text{nm}$ ,  $700\text{nm}$ , and  $750\text{nm}$  – for the grating structure (sketched in Fig.3.16(b)) have been used for the calculations. The gold strips have a thickness of  $130\text{nm}$  whereas the width of the slits in between the gold strips is  $100\text{nm}$ . The grating is excited by a TM polarized (E field along y-axis as in Fig.3.16(b)) plane wave source at visible-NIR wavelengths ( $500 - 850\text{nm}$ ). First, the diffracted angles for the four diffracted orders ( $0^{\text{th}}$ ,  $1^{\text{st}}$ ,  $-1^{\text{st}}$  and  $-2^{\text{nd}}$ ) have been calculated using the grating equation described below:

$$n_t \sin(\theta_m) = n_{inc} \sin(\theta_{inc}) + m \frac{\lambda}{p} \quad (3.17)$$

where  $n_t$  and  $n_{inc}$  are the refractive indices in the transmission and incidence domains respectively,  $m$  is the diffracted order,  $\lambda$  is the free space wavelength of the incident light,  $p$  is the grating period,  $\theta_{inc}$  is the incident angle and  $\theta_m$  is the angle of the  $m^{\text{th}}$  diffracted order. Only the above mentioned four diffracted orders have been considered because only these carry a significant amount of power and the power carried by the rest of the orders is negligible or zero. The incident angle,  $\theta_{inc}$ , has been varied in the range from 0 to 89 degrees at each wavelength of the light source in  $500 - 850\text{nm}$  range. Figure 3.17 represents the results of the calculated diffracted angles for the grating with a periodicity of  $630\text{nm}$ .

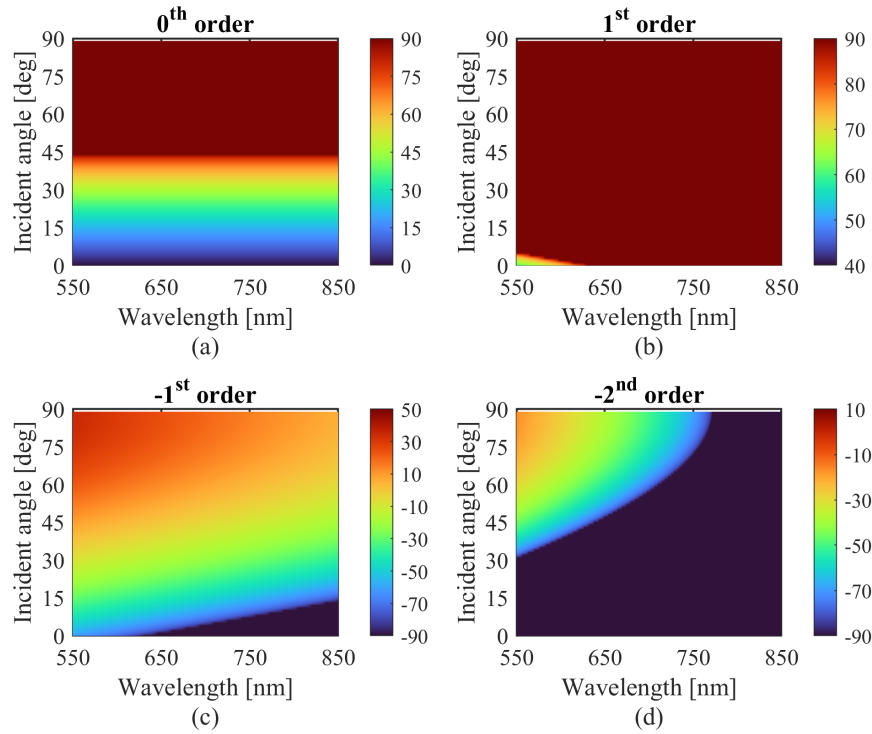


FIGURE 3.17: Maps of diffracted angles for transmitted orders at each wavelength and the angle of incidence (a)  $0^{\text{th}}$  order (b)  $1^{\text{st}}$  order (c)  $-1^{\text{st}}$  order (d)  $-2^{\text{nd}}$  order. The colour bar indicates the emission angles.

With the diffraction equation one can calculate the direction of the diffracted

orders but it does not tell us about diffraction efficiency of each diffracted order. For that, the fields must be calculated by solving Maxwell's equations. The RCWA method (DiffractMOD from RSoft) has been employed to calculate the power in each diffracted order. The simulated results of the power spectra for the four diffracted orders under consideration are shown in Fig. 3.18. The colour bar represents the normalized transmitted power.

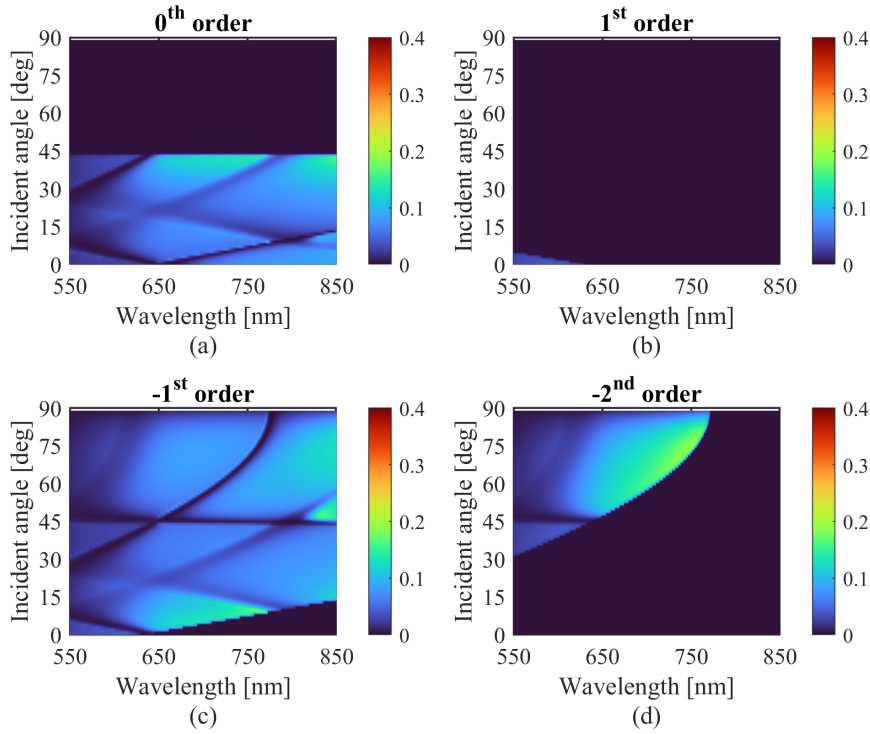


FIGURE 3.18: Maps of diffracted power for transmitted orders at each wavelength and the angle of incidence (a)  $0^{th}$  order (b)  $1^{st}$  order (c)  $-1^{st}$  order (d)  $-2^{nd}$ , respectively.

Next, the data is interpolated to get the required results where the transmitted power in each diffracted order is mapped as a function of the source wavelength and the diffracted angle. Then, the maps of Fig. 3.18 in emission angles are translated exploiting the maps in Fig.3.17. Figure 3.19 shows the resultant maps of the transmitted power when the emission angle is considered for the four diffracted orders for the grating period of  $630nm$  in the transmission domain range of  $[-50 + 50]$  degrees.

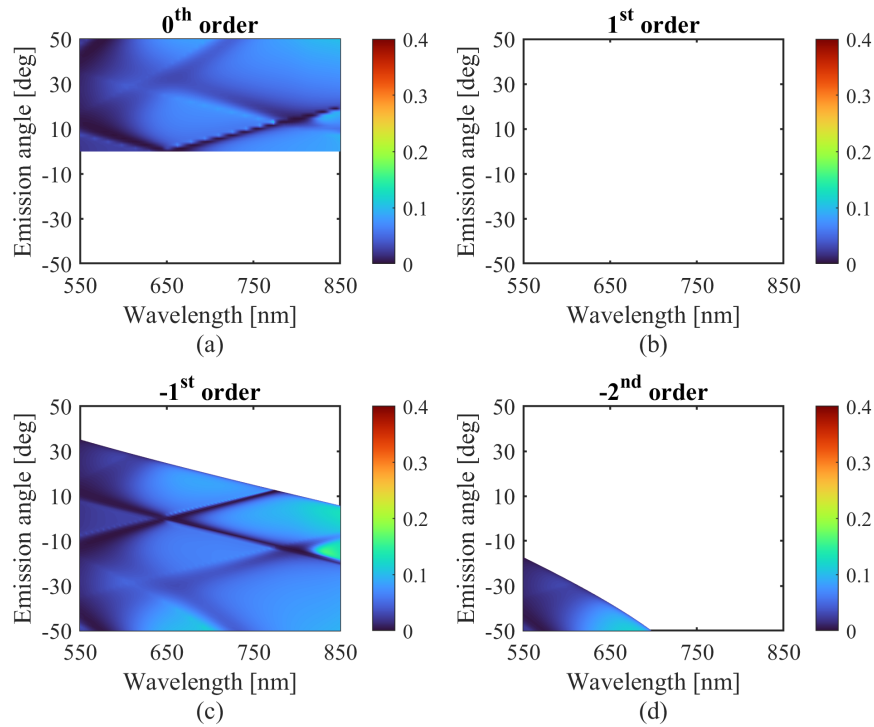


FIGURE 3.19: Emission spectra of the individual diffracted orders as function of the wavelength and emission angles (a)  $0^{th}$  order (b)  $1^{st}$  order (c)  $-1^{st}$  order (d)  $-2^{nd}$ . The considered range for emission angles is  $[-50\ 50]$  degrees.

As a final step, the total emission spectra of the grating structure are generated by combining the emission spectra of the individual diffracted orders. The results are shown in the Fig.3.20 for the three different periodicities of the grating structure  $630\text{nm}$ ,  $700\text{nm}$ , and  $750\text{nm}$ . It can be observed that the emission spectra is spectrally tunable by changing the grating periodicity.

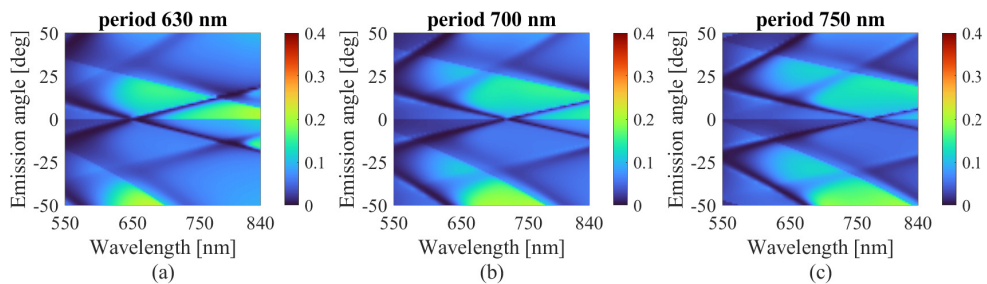


FIGURE 3.20: Emission spectra (dispersion diagram) of the grating as function of the wavelength and diffracted angles for three periodicities (a)  $630\text{nm}$  (b)  $700\text{nm}$  (c)  $750\text{nm}$ .

An SEM picture of the fabricated curved nanograting is shown in Fig.3.21(a) [111]. The optical response of the fabricated grating was measured using a Fourier micro spectroscopy system depicted in Fig.3.21(b). The emission diagrams of the

three different curved nanogratings milled with periodicities of  $630\text{nm}$ ,  $700\text{nm}$  and  $750\text{nm}$  were measured. The resultant emission diagrams are shown in Fig.3.21(c). As expected, the resonances shift according to the grating periodicity. The measured results agree well with the emission spectra of the curved grating predicted by the numerical model.

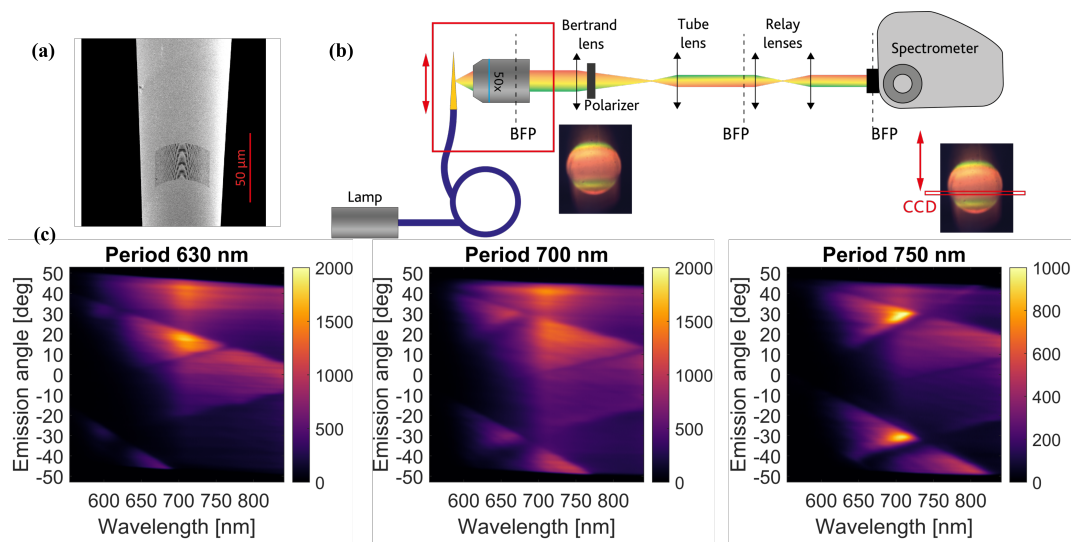


FIGURE 3.21: Spectrally tunable surface plasmon resonances on the curved fiber surface. (a) An SEM picture of the fabricated curved nanograting on a tapered optical fiber. (b) Diagram of the Fourier microscopy system used to measure the dispersion diagrams for curved nanograting at several periodicities. (c) Measured dispersion diagrams for curved nanograting milled with periodicities of  $630\text{nm}$ ,  $700\text{nm}$ , and  $750\text{nm}$  [111].

### 3.5 Surface Enhanced Raman Scattering (SERS)

Surface enhanced Raman spectroscopy (SERS) is a very powerful and extremely sensitive analytical tool for the detection of chemical and biological substances. It has been demonstrated for an ultimate limit of single-molecule detection [112] and biosensing in a single living cell [113].

Plasmonic nanostructures are employed as platform for SERS that can create electric field hotspots. This as a result remarkably enhances the Raman signal from the target molecules. The enhancement factor can range from  $10^6$  to  $10^{12}$  [114]. The enhancement mainly comes from the electromagnetic phenomenon. The electromagnetic enhancement is proportional to the field hotspot as  $E^4$ . There is also a contribution of chemical phenomenon in the total overall enhancement which is typically in the range of  $\sim 10^2$  [114, 115].

With recent progress in nanofabrication technologies, there has been a revived interest in SERS. In the field of bio-photonics there is a growing interest in the design and development of optical fiber probes. Such probes integrated with SERS active

substrates have been demonstrated as biological sensors. In this framework Ag/Au nanostructures have been used at the tip of tapered optical fiber [116, 117, 118]. Apart from tapered optical fiber, plasmonic nanostructures on the fiber facet have also been demonstrated for the detection of SERS [119, 120].

Although a considerable experimental work on optical fiber probes for SERS applications is reported in the technical literature there are no sufficient numerical studies found in this domain. In the following a numerical design approach for the SERS studies is presented. A numerical model of the plasmonic grating fabricated on a tapered optical fiber is developed. Apart from the electric field calculations the model can simulate the SERS signal from a target material by using the non-linear optical properties. Additionally, numerical analysis of a nano-hole array fabricated on the optical fiber facet is presented.

### 3.5.1 Curved plasmonic grating as a SERS platform

To analyse curved grating as a SERS platform, a three-dimensional (3D) finite difference time domain (FDTD) model of the curved grating structure shown in Fig.3.12(b) has been developed. It supports the non-linear material models where the refractive index changes as a function of the input field intensity and allows to study Kerr and Raman interactions. The dispersive third order ( $\chi^3$ ) nonlinear properties are described in Chapter 1 section 1.2.5.

The curved cylindrical glass substrate has a radius  $R$  equal to  $30\mu\text{m}$ . The gold strips have an arc length  $L$  of  $25\mu\text{m}$  along the glass surface curvature (fiber window). The grating has a periodicity  $p$  of  $600\text{nm}$  with a width  $w$  of  $470\text{nm}$ . The gold layer is  $130\text{nm}$  thick. These geometrical parameters are used based on the fabricated device. In simulations, to reduce the computational load, the  $L$  and  $R$  parameters have been reduced by a factor of 10 to manage the computational load. However, this does not affect the surface curvature as it depends upon  $L/R$  ratio.

Olive oil has been used as the target material in this work. The optical properties such as refractive index and the third order non-linearity are well known. Moreover, the Raman spectra of olive oil has strong peaks at  $1441\text{cm}^{-1}$  and  $2887\text{cm}^{-1}$ . Many biological tissues have these signatures due to lipid contents. The third-order electric susceptibility of olive oil has been taken from [121]. Olive oil Raman spectra have distinct peaks at  $1441\text{cm}^{-1}$  ( $885\text{nm}$ ) and  $2887\text{cm}^{-1}$  ( $1015\text{nm}$ ) measured with a laser source at  $785\text{nm}$  [122]. The input electric field is modelled as a TM polarized plane wave impinging at  $60^\circ$  on the grating following the experiments.

Figure 3.22 shows the simulated Raman spectra of a thin layer of olive oil (0.5 micron) in both transmission and reflection domains when it is excited by a  $785\text{nm}$  continuous wave. The spectra are calculated with an input field intensity of  $E = 1 \times 10^6 \text{V/m}$ . For comparison, SERS signals from olive oil with a planar grating are also calculated using a 2D FDTD model. The results are shown in Fig.3.23. The simulated SERS spectra showing the Stoke signals at  $1441\text{cm}^{-1}$  ( $885\text{nm}$ ) and  $2887\text{cm}^{-1}$  ( $1015\text{nm}$ ) in transmission and reflection domains when a thin layer of olive

oil is placed on a planar gold grating. The grating has a period  $p = 600nm$ , width  $w = 100nm$  and the gold layer thickness is  $130nm$ . The input field intensity used is  $E = 5 \times 10^5 V/m$ .

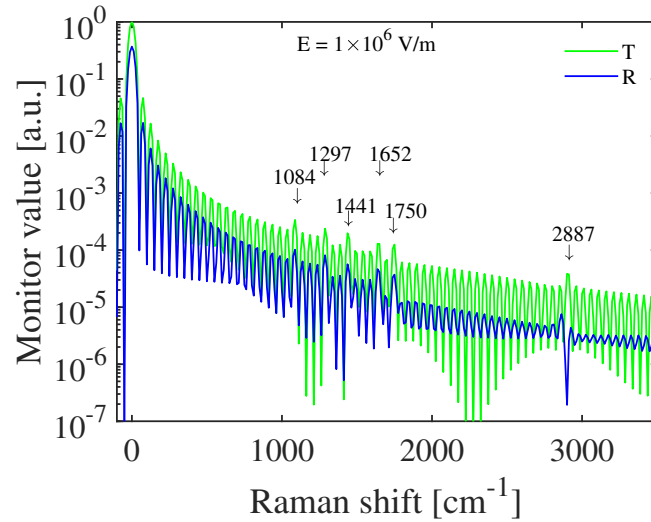


FIGURE 3.22: The simulated Raman spectra of a thin layer (0.5 micron) of olive oil in transmission and reflection domains at an input field intensity of  $E = 1 \times 10^6 V/m$ .

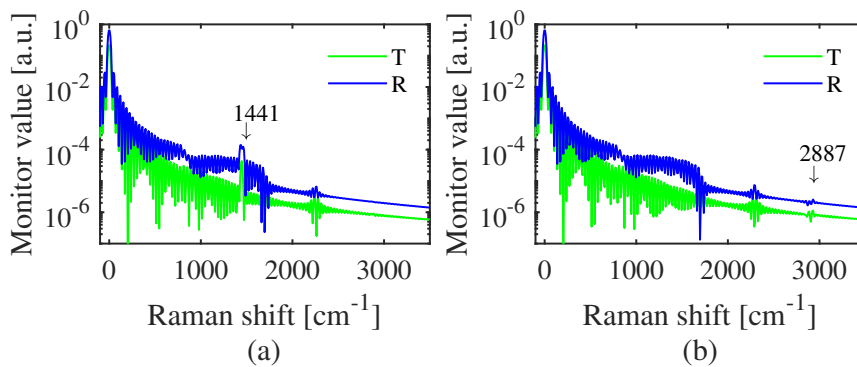


FIGURE 3.23: (a) The simulated SERS spectra showing the Stoke signal at  $1441cm^{-1}$  ( $885nm$ ) in transmission and reflection domains when a thin layer of olive oil is placed on a planar gold grating (b) Same as in (a) showing the Stoke signal at  $2887cm^{-1}$  ( $1015nm$ ). A 2D FDTD model of gold grating is used to calculate these spectra. The grating has a period  $p = 600nm$ , width  $w = 100nm$  and the gold layer thickness is  $130nm$ . The input field intensity used is  $E = 5 \times 10^5 V/m$ .

Simulated SERS spectra of olive oil using a 3D model of curved grating for the Stoke's peaks of  $1441cm^{-1}$  and  $2887cm^{-1}$  are shown in Fig.3.24 and Fig.3.25, respectively. The period, width and the gold thickness of the fabricated device are  $600nm$ ,  $470nm$  and  $130nm$ , respectively. A geometrical parameter study of the width and gold thickness (Fig.3.25) shows the strength of SERS signal is sensitive to these parameters. The minimum pump field intensity used for these simulations is  $10^5 V/m$ .

Below this value no reasonable enhancement is observed in the SERS signals. This is because of the lower field enhancement given by the plasmonic grating. While a grating is not an ideal structure for achieving higher field enhancements it can give higher optical transmission compared to a nano-hole array, for example. Based on the requirement of higher optical transmission a grating is used in this study.

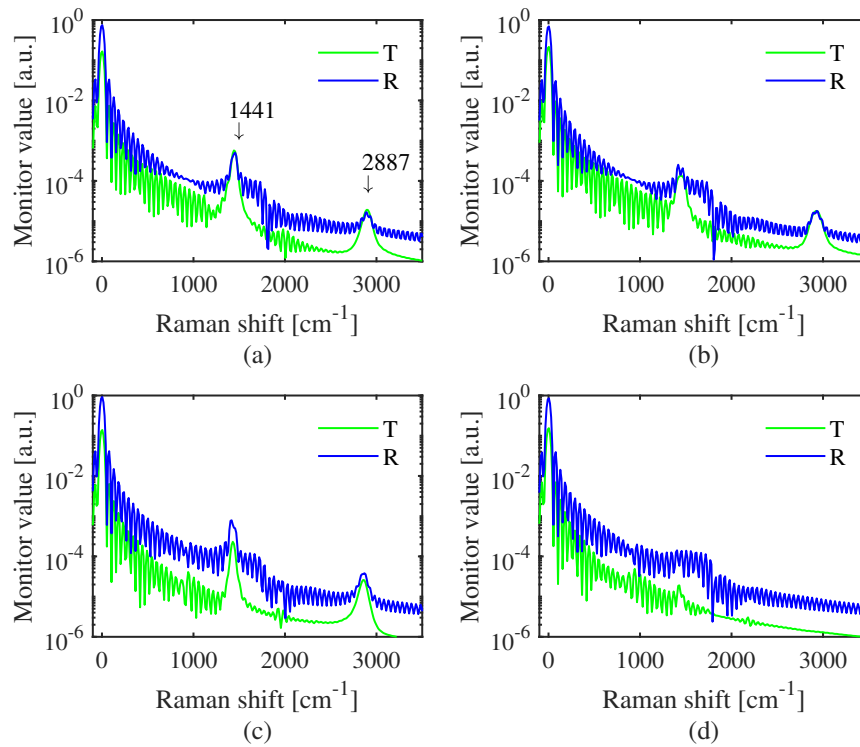


FIGURE 3.24: The simulated SERS spectra showing the Stoke signal at  $1441\text{cm}^{-1}$  ( $885\text{nm}$ ) in transmission and reflection domains when a thin layer of olive oil is placed on a curved gold grating (a) The grating has a period  $p = 600\text{nm}$ , width  $w = 300\text{nm}$  and the gold layer thickness is  $100\text{nm}$  (b) The grating has a period  $p = 600\text{nm}$ , width  $w = 300\text{nm}$  and the gold layer thickness is  $130\text{nm}$  (c) The grating has a period  $p = 600\text{nm}$ , width  $w = 470\text{nm}$  and the gold layer thickness is  $100\text{nm}$  (d) The grating has a period  $p = 600\text{nm}$ , width  $w = 470\text{nm}$  and the gold layer thickness is  $130\text{nm}$ . A 3D FDTD model of gold grating is used to calculate these spectra. The input field intensity used is  $E = 1 \times 10^5 \text{V/m}$ . Apart from the targeted Stoke signal at  $1441\text{cm}^{-1}$  a second Stoke peak at  $2887\text{cm}^{-1}$  also appears in the spectra.

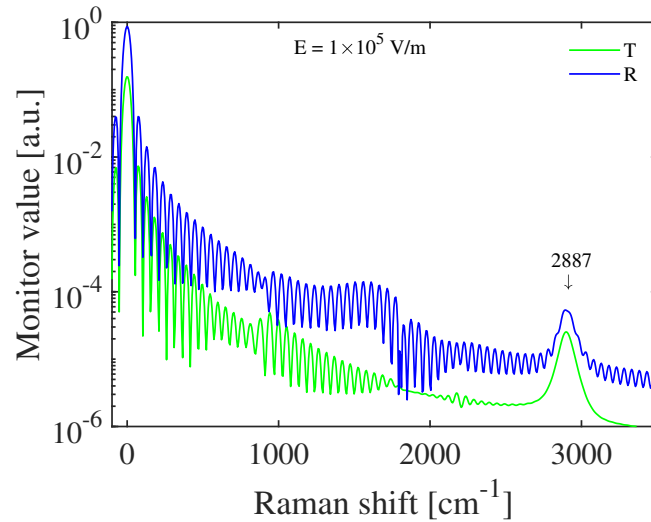


FIGURE 3.25: The simulated SERS spectra showing the Stoke signal at  $2887\text{cm}^{-1}$  ( $1015\text{nm}$ ) in transmission and reflection domains when a thin layer of olive oil is placed on a curved gold grating. The grating has a period  $p = 600\text{nm}$ , width  $w = 470\text{nm}$  and the gold layer thickness is  $130\text{nm}$ . A 3D FDTD model of gold grating is used to calculate these spectra. The input field intensity used is  $E = 1 \times 10^5 \text{V/m}$ .

For the curved grating, field intensity has been calculated at the source wavelength of  $785\text{nm}$  and the Stoke's wavelengths of  $885\text{nm}$  ( $1441\text{cm}^{-1}$ ) and  $1015\text{nm}$  ( $2887\text{cm}^{-1}$ ). A field monitor placed in the gap along the side wall of the gold strip snaps the field in XZ domain (Fig.3.12). Two other field monitors - one placed at the center ( $x = 0$ ) and other near the corner - picture the field in YZ domain. The field plots in Fig.3.26 show sizable enhancements at all three wavelengths. Also, the field enhancements are more in the reflection domain as compared to the transmission domain.

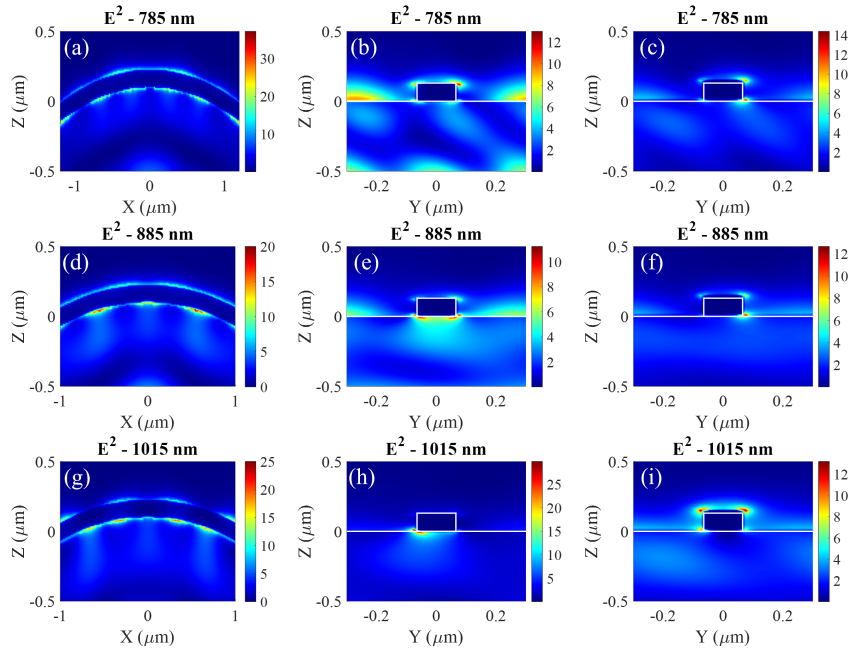


FIGURE 3.26: (a) Electric field intensity profile of the curved grating in XZ plane at 885nm when light is incident at an angle ( $\theta$ ) of  $60^\circ$  [111] (b) Electric field intensity profile of the curved grating in YZ plane at 885 nm snapped at the center of the curved grating, (c) Same as in (b) snapped at the corner of the curved grating, (d) Same as in (a) at 1015nm, (e) Same as in (b) at 1015nm, (f) Same as in (c) at 1015nm.

Figure 3.27 shows the experimental results related to Raman signals measurements from olive oil by the curved nanograting fabricated on the tapered optical fiber [111]. The fabricated device parameters are described in the starting paragraph of this section. For these measurements the tapered optical fiber was immersed in olive oil as depicted in Fig.3.27(a). A laser source of 785nm was used as pump. The source excitation via the curved nanograting as EOT generated a Raman signal. The Raman signal was collected by the same grating and coupled into the optical fiber. Figures 3.27 (b-c) show the Raman signal of the lipid bands of olive oil at  $1441\text{cm}^{-1}$  and  $2887\text{cm}^{-1}$ , respectively. For comparison, the Raman signal collected through the tapered optical is plotted against a reference Raman spectrum. The measured Raman results find good agreement with the numerically computed Raman spectra. In simulations an input field intensity of  $\sim 10^5\text{V/m}$  is used. Below this value no sizeable surface enhancement can be achieved. However, the experimental system was limited to  $\sim 10^3\text{V/m}$  on the curved nanograting through the optical fiber.

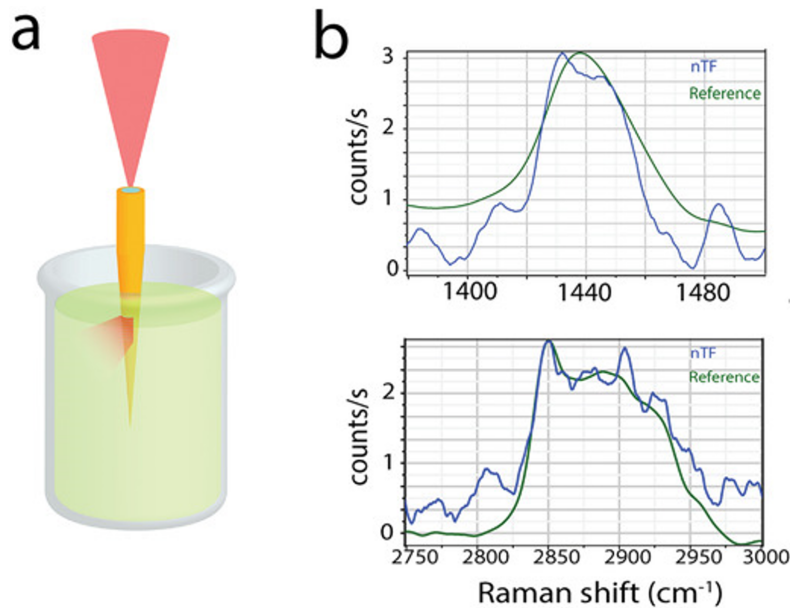


FIGURE 3.27: Plasmon-assisted spectroscopy with tapered optical fiber probe. (a) Sketch of the experimental measurement. The tapered optical fiber, immersed in olive oil, receives illumination from the back facet. The  $785\text{nm}$  light is emitted from the curved nanograting that, in turn, collects the Raman signal and couples it with the waveguide. (b) Raman spectra of olive oil collected with the tapered optical fiber (blue) and with a standard objective lens (green) around the  $1441\text{cm}^{-1}$  (top) and  $2800 - 3000\text{cm}^{-1}$  (bottom) bands. The intensity counts of the reference signals have been normalized to the tapered optical fiber measurements for the ease of comparison. nTF in the legend stands for the nano tapered fiber [111].

### 3.5.2 EOT from a nanohole array on optical fiber facet

Finally, a set of arrays of nanoholes on the facet of a fiber has been numerically analysed (Fig.3.16(c)). The fiber facet has a diameter of  $50\mu\text{m}$ . Nine nanohole arrays are milled on the fiber facet in the form of  $3 \times 3$  matrix. Each nanohole array has different periodicity. The periodicities are  $[560, 580, 600, 620, 640, 660, 680, 700, 720]\text{nm}$ . The nanohole has diameter as well as depth of  $100\text{nm}$ . The simulated transmittance through nanohole arrays is shown in Fig.3.28 at  $633\text{nm}$  for plane wave excitation considering a periodic nanohole array structure. A peak in the transmittance (EOT) for  $640\text{nm}$  period array is because of the fact that the grating period matches the wavelength of the incident light.

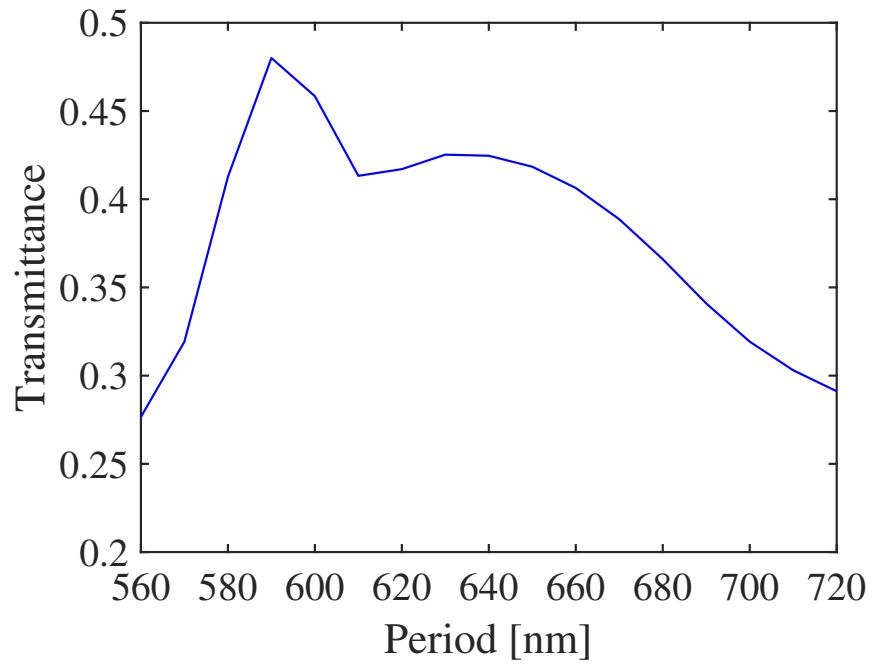


FIGURE 3.28: Simulated transmittance through nanohole arrays at 633 nm.

To compute a near field image from a sub-section of a nanohole array a finite portion of the nanohole array is simulated employing a 3D FDTD model. A Gaussian beam with a spot size of  $3.5\mu\text{m}$  is used at  $633\text{nm}$ . The computed field intensity is shown in Fig.3.29.

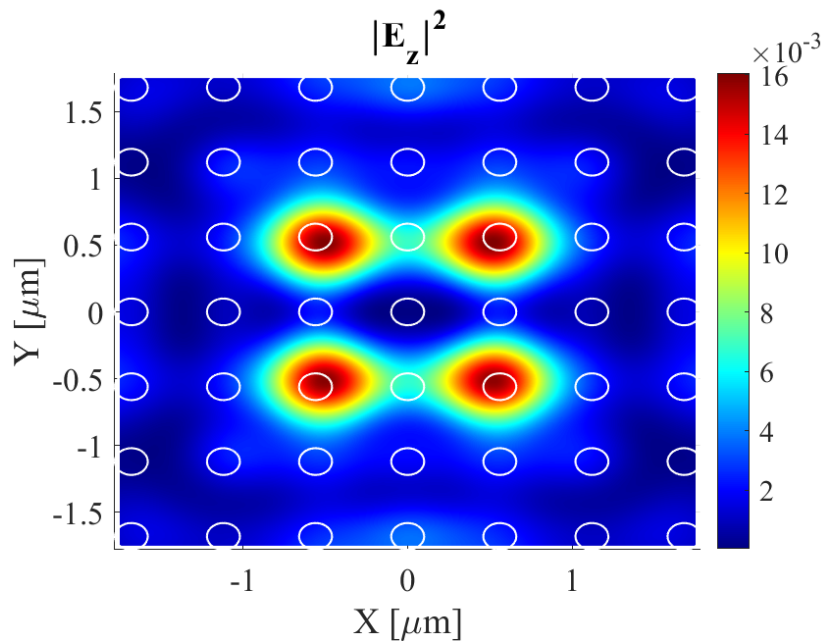


FIGURE 3.29: Near field image from a sub-section of a nanohole array showing sub-diffraction beam shaping.

## Chapter 4

# Conclusion

Optical devices based on resonant periodic structures have become incredibly important because of their wide-ranging applications in communication system, biosensing, and spectroscopy. This thesis describes the design, fabrication, and characterization of the resonant optical structures that are based on dielectric and metallic gratings. The main outcomes of this research are briefly summarized in the following paragraphs.

- A 2D grating of cylindrical PMMA pillars has been designed and analysed through numerical simulations. It exploits GMRs to enhance light absorption in the monolayer graphene. It achieved light absorption of more than 40% at multiple wavelengths for both TE and TM polarizations over narrow bandwidths in the visible and near-infrared ranges. The proposed optical absorber is less sensitive to geometrical parameters variations, polarization, and angle of the incident light. It can be easily realized using nanofabrication technologies such as nano-imprint lithography. These results can pave the way for the development of easy to fabricate and experimentally viable graphene-based optical absorbers for future photonic devices.
- A resonant pillar grating that includes a thin layer of phase-change material (vanadium dioxide) has been designed, fabricated, and characterized to achieve tunable optical response in the visible. Despite the inherently small perturbation introduced by the thin layer of vanadium dioxide, highly confined photonic modes are able to boost the optical sensitivity of the grating and improve the capability to modulate the optical response under the application of an external stimulus. The low and high temperature states of vanadium oxide are induced by mounting the sample on a thermal heater, demonstrating a 10% reflectance variation in the visible near 600 nm. Future work will be also dedicated to assessing the tunable properties of the structure at infrared wavelengths, where resonances are expected to be more significantly quenched by absorption losses introduced by the metallic phase of vanadium dioxide.  $\text{VO}_2$  has a great potential for the development of tunable and reconfigurable photonic devices due to its phase change properties. Resonant gratings with tunable spectral response may find application in sensors, filters, absorbers, and detectors.

- An RCWA and a FDTD models of a 2D array of nanoplatelets have been developed to give a comprehensive theoretical description of the combination of plasmonic and diffractive effects in finite as well as periodic structures of the fabricated array. A high optical transmission (approaching 10 %) has been achieved by illuminating a subset of the array (20 elements). The sensing performance of the NPs array has been demonstrated both using the reflected and transmitted light. These results will be helpful for the future research on the plasmonic nanostructures for advanced biosensing applications.
- A gold nano-grating on a curved surface has been analysed through a segmented-wave approximation technique as well as by a 3D FDTD model of the curved grating. The results from both the techniques show a good agreement. This is a good starting point to further extend this segmentation-based technique to simulate complex structures especially on curved structures such as an optical fiber to reduce the simulation time and computational load.
- An RCWA simulation model has been developed to compute the emission spectra of a plasmonic grating. The simulated results agree well with the measured emission spectra from a grating fabricated on a curved surface.
- A 3D FDTD model of a curved grating has been developed to engineer the field enhancement for SERS measurements. Further, the non-linear material models are incorporated in the 3D FDTD model to study Kerr and Raman interactions. This enabled the simulation model to compute the SERS spectra of a target material where the curved grating has been used as a SERS active platform. Several geometrical parameters such as grating slit widths and thickness of gold layer are studied. Optical fiber based SERS probes are gaining importance due to their potential in endoscopic spectroscopy and highly sensitive biosensing at desired locations. The nanofabrication of such probes is challenging, and it requires expensive equipment. The development of accurate optical simulation models is, therefore, important as they can give useful information for the design and optimal performance of such nanostructures.

# Bibliography

- [1] R.-B. Hwang, *Periodic Structures: Mode-matching Approach and Applications in Electromagnetic Engineering*. Wiley-IEEE Press, 2012.
- [2] J. E. Harvey and R. N. Pfisterer, "Understanding diffraction grating behavior: including conical diffraction and rayleigh anomalies from transmission gratings," *Optical Engineering*, vol. 58, no. 8, pp. 087105–, 2019.
- [3] R. W. Wood, "On a remarkable case of uneven distribution of light in a diffraction grating spectrum," *Proceedings of the Physical Society of London*, vol. 18, no. 1, pp. 269–275, 1902.
- [4] J. W. Strutt, "On the dynamical theory of gratings," *Proceedings of the Royal Society of London. Series A, Containing Papers of a Mathematical and Physical Character*, vol. 79, no. 532, pp. 399–416, 1907.
- [5] U. Fano, "The theory of anomalous diffraction gratings and of quasi-stationary waves on metallic surfaces (sommerfeld's waves)," *J. Opt. Soc. Am.*, vol. 31, no. 3, pp. 213–222, 1941.
- [6] A. Hessel and A. A. Oliner, "A new theory of wood's anomalies on optical gratings," *Appl. Opt.*, vol. 4, no. 10, pp. 1275–1297, 1965.
- [7] G. Quaranta, G. Basset, O. J. F. Martin, and B. Gallinet, "Recent advances in resonant waveguide gratings," *Laser and Photonics Reviews*, vol. 12, no. 9, p. 1800017, 2018.
- [8] R. Magnusson and Y. H. Ko, "Guided-mode resonance nanophotonics: fundamentals and applications," *Nanoengineering: Fabrication, Properties, Optics, and Devices XIII*, vol. 9927, pp. 992702–, 2016.
- [9] M. F. Kashif, G. V. Bianco, T. Stomeo, M. A. Vincenti, D. de Ceglia, M. De Vittorio, M. Scalora, G. Bruno, A. D'Orazio, and M. Grande, "Graphene-based cylindrical pillar gratings for polarization-insensitive optical absorbers," *Applied Sciences*, vol. 9, no. 12, 2019.
- [10] M. F. Kashif, A. D'Orazio, M. Grande, T. Stomeo, F. Guido, M. de Vittorio, M. A. Vincenti, I. Vassalini, I. Alessandri, C. de Angelis, and D. de Ceglia, "Thermal tuning of resonant gratings using a phase-change material," in *2020 22nd International Conference on Transparent Optical Networks (ICTON)*, pp. 1–4, 2020.

- [11] E. Kretschmann and H. Raether, "Notizen: Radiative decay of non radiative surface plasmons excited by light," *Zeitschrift für Naturforschung A*, vol. 23, no. 12, pp. 2135–2136, 1968.
- [12] D. de Ceglia, M. A. Vincenti, M. Scalora, N. Akozbek, and M. J. Bloemer, "Plasmonic band edge effects on the transmission properties of metal gratings," *AIP Advances*, vol. 1, no. 3, p. 032151, 2011.
- [13] M. Grande, M. A. Vincenti, T. Stomeo, G. Morea, R. Marani, V. Marrocco, V. Petruzzelli, A. D'Orazio, R. Cingolani, M. D. Vittorio, D. de Ceglia, and M. Scalora, "Experimental demonstration of a novel bio-sensing platform via plasmonic band gap formation in gold nano-patch arrays," *Opt. Express*, vol. 19, no. 22, pp. 21385–21395, 2011.
- [14] W. L. Barnes, A. Dereux, and T. W. Ebbesen, "Surface plasmon subwavelength optics," *Nature*, vol. 424, no. 6950, pp. 824–830, 2003.
- [15] S. Kasani, K. Curtin, and N. Wu, "A review of 2d and 3d plasmonic nanostructure array patterns: fabrication, light management and sensing applications," *Nanophotonics*, vol. 8, no. 12, pp. 2065–2089, 2019.
- [16] J. Langer, D. J. de Aberasturi, J. Aizpurua, R. A. Alvarez-Puebla, B. Auguie, J. J., and et. al, "Present and Future of Surface-Enhanced Raman Scattering," *ACS Nano*, vol. 14, no. 1, pp. 28–117, 2020.
- [17] F. Pisano, A. Balena, M. F. Kashif, M. Pisanello, G. de Marzo, L. Algieri, A. Qualtieri, L. Sileo, T. Stomeo, A. D'Orazio, M. D. Vittorio, F. Pisanello, and M. Grande, "High transmission from 2d periodic plasmonic finite arrays with sub-20 nm gaps realized with ga focused ion beam milling," *Nanotechnology*, vol. 31, no. 43, p. 435301, 2020.
- [18] M. F. Kashif, F. Pisano, A. Balena, M. Pisanello, G. de Marzo, L. Algieri, A. Qualtieri, L. Sileo, T. Stomeo, A. D'Orazio, M. D. Vittorio, F. Pisanello, and M. Grande, "Optical properties of finite subsets of fib-milled 2d periodic arrays of gold nanoplatelets with sub-20-nm gaps," in *Frontiers in Optics / Laser Science*, p. JTh4B.6, OSA, 2020.
- [19] S. Maier, *Plasmonics: Fundamentals and Applications*. Springer, 2007.
- [20] E. D. Palik, *Handbook of Optical Constants of Solids*. Academic Press, 1998.
- [21] P. B. Johnson and R. W. Christy, "Optical constants of the noble metals," *Phys. Rev. B*, vol. 6, pp. 4370–4379, 1972.
- [22] D. I. Yakubovsky, A. V. Arsenin, Y. V. Stebunov, D. Y. Fedyanin, and V. S. Volkov, "Optical constants and structural properties of thin gold films," *Opt. Express*, vol. 25, no. 21, pp. 25574–25587, 2017.

- [23] S. Zhang, W. Fan, K. J. Malloy, S. R. J. Brueck, N. C. Panoiu, and R. M. Osgood, "Demonstration of metal-dielectric negative-index metamaterials with improved performance at optical frequencies," *J. Opt. Soc. Am. B*, vol. 23, no. 3, pp. 434–438, 2006.
- [24] D. Barchiesi and T. Grosjes, "Fitting the optical constants of gold, silver, chromium, titanium, and aluminum in the visible bandwidth," *Journal of Nanophotonics*, vol. 8, no. 1, pp. 1–17, 2014.
- [25] G. Agrawal, *Fiber-Optic Communications Systems*. Wiley, 3rd ed., 2002.
- [26] K. Luke, Y. Okawachi, M. R. E. Lamont, A. L. Gaeta, and M. Lipson, "Broad-band mid-infrared frequency comb generation in a  $\text{Si}_3\text{N}_4$  microresonator," *Opt. Lett.*, vol. 40, no. 21, pp. 4823–4826, 2015.
- [27] R. W. Boyd, *Nonlinear Optics*. Academic Press, 4th ed., 2020.
- [28] K. S. Novoselov, A. K. Geim, S. V. Morozov, D. Jiang, Y. Zhang, S. V. Dubonos, I. V. Grigorieva, and A. A. Firsov, "Electric field effect in atomically thin carbon films," *Science*, vol. 306, no. 5696, pp. 666–669, 2004.
- [29] M. Bruna and S. Borini, "Optical constants of graphene layers in the visible range," *Applied Physics Letters*, vol. 94, no. 3, p. 031901, 2009.
- [30] G. W. Hanson, "Dyadic green's functions and guided surface waves for a surface conductivity model of graphene," *Journal of Applied Physics*, vol. 103, no. 6, p. 064302, 2008.
- [31] L. A. Falkovsky, "Optical properties of graphene," *Journal of Physics: Conference Series*, vol. 129, p. 012004, 2008.
- [32] P. Kepič, F. Ligmajer, M. Hrtoň, H. Ren, L. d. S. Menezes, S. A. Maier, and T. Šikola, "Optically tunable mie resonance  $\text{VO}_2$  nanoantennas for metasurfaces in the visible," *ACS Photonics*, vol. 8, no. 4, pp. 1048–1057, 2021.
- [33] C. Wan, Z. Zhang, D. Woolf, C. M. Hessel, J. Rensberg, J. M. Hensley, Y. Xiao, A. Shahsafi, J. Salman, S. Richter, Y. Sun, M. M. Qazilbash, R. Schmidt-Grund, C. Ronning, S. Ramanathan, and M. A. Kats, "On the optical properties of thin-film vanadium dioxide from the visible to the far infrared," *Annalen der Physik*, vol. 531, no. 10, p. 1900188, 2019.
- [34] A. Taflove and S. C. Hangness, *Computational Electrodynamics: The Finite-Difference-Time-Domain Method*. Artech House, 2nd ed., 2005.
- [35] M. S. Wartak, *Computational Photonics: An Introduction with MATLAB*. Cambridge University Press, 2013.
- [36] "Synopsys inc., rsoft products," <https://www.synopsys.com>.

- [37] “Lumerical inc., fdtd,” <https://www.lumerical.com>.
- [38] K. Knop, “Rigorous diffraction theory for transmission phase gratings with deep rectangular grooves,” *J. Opt. Soc. Am.*, vol. 68, no. 9, pp. 1206–1210, 1978.
- [39] M. G. Moharam and T. K. Gaylord, “Rigorous coupled-wave analysis of planar-grating diffraction,” *J. Opt. Soc. Am.*, vol. 71, no. 7, pp. 811–818, 1981.
- [40] M. S. L. Lee, P. Lalanne, J. C. Rodier, P. Chavel, E. Cambril, and Y. Chen, “Imaging with blazed-binary diffractive elements,” *Journal of Optics A: Pure and Applied Optics*, vol. 4, no. 5, pp. S119–S124, 2002.
- [41] E. Popov and M. Nevière, “Maxwell equations in fourier space: fast-converging formulation for diffraction by arbitrary shaped, periodic, anisotropic media,” *J. Opt. Soc. Am. A*, vol. 18, no. 11, pp. 2886–2894, 2001.
- [42] G. R. Hadley, “Wide-angle beam propagation using padé approximant operators,” *Opt. Lett.*, vol. 17, no. 20, pp. 1426–1428, 1992.
- [43] M. Veetikazhy, A. K. Hansen, D. Marti, S. M. Jensen, A. L. Borre, E. R. Andresen, K. Dholakia, and P. E. Andersen, “Bpm-matlab: an open-source optical propagation simulation tool in matlab,” *Opt. Express*, vol. 29, no. 8, pp. 11819–11832, 2021.
- [44] D. Yevick and B. Hermansson, “Efficient beam propagation techniques,” *IEEE Journal of Quantum Electronics*, vol. 26, no. 1, pp. 109–112, 1990.
- [45] S. S. Wang and R. Magnusson, “Theory and applications of guided-mode resonance filters,” *Appl. Opt.*, vol. 32, no. 14, pp. 2606–2613, 1993.
- [46] K. S. Novoselov, A. K. Geim, S. V. Morozov, D. Jiang, Y. Zhang, S. V. Dubonos, I. V. Grigorieva, and A. A. Firsov, “Electric field effect in atomically thin carbon films,” *Science*, vol. 306, no. 5696, pp. 666–669, 2004.
- [47] S. Szunerits and R. Boukherroub, “Graphene-based biosensors,” *Interface Focus*, vol. 8, no. 3, p. 20160132, 2018.
- [48] M. Freitag, T. Low, W. Zhu, H. Yan, F. Xia, and P. Avouris, “Photocurrent in graphene harnessed by tunable intrinsic plasmons,” *Nature Communications*, vol. 4, no. 1, p. 1951, 2013.
- [49] Z. Sun and H. Chang, “Graphene and graphene-like two-dimensional materials in photodetection: Mechanisms and methodology,” *ACS Nano*, vol. 8, no. 5, pp. 4133–4156, 2014. PMID: 24716438.
- [50] S. Z. Butler, S. M. Hollen, L. Cao, Y. Cui, J. A. Gupta, H. R. Gutiérrez, T. F. Heinz, S. S. Hong, J. Huang, A. F. Ismach, E. Johnston-Halperin, M. Kuno, V. V. Plashnitsa, R. D. Robinson, R. S. Ruoff, S. Salahuddin, J. Shan, L. Shi,

- M. G. Spencer, M. Terrones, W. Windl, and J. E. Goldberger, "Progress, challenges, and opportunities in two-dimensional materials beyond graphene," *ACS Nano*, vol. 7, no. 4, pp. 2898–2926, 2013. PMID: 23464873.
- [51] W. Gao, J. Shu, C. Qiu, and Q. Xu, "Excitation of plasmonic waves in graphene by guided-mode resonances," *ACS Nano*, vol. 6, no. 9, pp. 7806–7813, 2012. PMID: 22862147.
- [52] Y. Fan, C. Guo, Z. Zhu, W. Xu, F. Wu, X. Yuan, and S. Qin, "Monolayer-graphene-based broadband and wide-angle perfect absorption structures in the near infrared," *Scientific Reports*, vol. 8, no. 1, p. 13709, 2018.
- [53] S. Zhang, Y. Wang, S. Wang, and W. Zheng, "Wavelength-tunable perfect absorber based on guided-mode resonances," *Appl. Opt.*, vol. 55, no. 12, pp. 3176–3181, 2016.
- [54] B. Zhao, J. M. Zhao, and Z. M. Zhang, "Resonance enhanced absorption in a graphene monolayer using deep metal gratings," *J. Opt. Soc. Am. B*, vol. 32, no. 6, pp. 1176–1185, 2015.
- [55] M. A. Vincenti, D. de Ceglia, M. Grande, A. D'Orazio, and M. Scalora, "Nonlinear control of absorption in one-dimensional photonic crystal with graphene-based defect," *Opt. Lett.*, vol. 38, no. 18, pp. 3550–3553, 2013.
- [56] A. Mahigir and G. Veronis, "Nanostructure for near total light absorption in a monolayer of graphene in the visible," *J. Opt. Soc. Am. B*, vol. 35, no. 12, pp. 3153–3158, 2018.
- [57] J. Wu, "Ultra-narrow perfect graphene absorber based on critical coupling," *Optics Communications*, vol. 435, pp. 25–29, Mar. 2019.
- [58] L. Yang, J. Wang, and C. Lu, "Sensitive perfect absorber with monolayer graphene-based multi-layer dielectric grating structure," *Optik*, vol. 158, pp. 508–513, 2018.
- [59] J. Hu, Y. Qing, S. Yang, Y. Ren, X. Wu, W. Gao, and C. Wu, "Tailoring total absorption in a graphene monolayer covered subwavelength multilayer dielectric grating structure at near-infrared frequencies," *J. Opt. Soc. Am. B*, vol. 34, no. 4, pp. 861–868, 2017.
- [60] M. Grande, M. A. Vincenti, T. Stomeo, G. V. Bianco, D. de Ceglia, N. Aközbek, V. Petruzzelli, G. Bruno, M. D. Vittorio, M. Scalora, and A. D'Orazio, "Graphene-based perfect optical absorbers harnessing guided mode resonances," *Opt. Express*, vol. 23, no. 16, pp. 21032–21042, 2015.
- [61] M. Grande, M. A. Vincenti, T. Stomeo, G. V. Bianco, D. de Ceglia, N. Aközbek, V. Petruzzelli, G. Bruno, M. D. Vittorio, M. Scalora, and A. D'Orazio,

- "Graphene-based absorber exploiting guided mode resonances in one-dimensional gratings," *Opt. Express*, vol. 22, no. 25, pp. 31511–31519, 2014.
- [62] A. Safaei, S. Chandra, A. Vázquez-Guardado, J. Calderon, D. Franklin, L. Tetard, L. Zhai, M. N. Leuenberger, and D. Chanda, "Dynamically tunable extraordinary light absorption in monolayer graphene," *Phys. Rev. B*, vol. 96, p. 165431, 2017.
- [63] C.-C. Guo, Z.-H. Zhu, X.-D. Yuan, W.-M. Ye, K. Liu, J.-F. Zhang, W. Xu, and S.-Q. Qin, "Experimental demonstration of total absorption over 99% in the near infrared for monolayer-graphene-based subwavelength structures," *Advanced Optical Materials*, vol. 4, no. 12, pp. 1955–1960, 2016.
- [64] D. de Ceglia, M. A. Vincenti, M. Grande, G. V. Bianco, G. Bruno, A. D'Orazio, and M. Scalora, "Tuning infrared guided-mode resonances with graphene," *J. Opt. Soc. Am. B*, vol. 33, no. 3, pp. 426–433, 2016.
- [65] M. Grande, T. Stomeo, G. V. Bianco, M. A. Vincenti, D. de Ceglia, V. Petruzzelli, G. Bruno, M. De Vittorio, M. Scalora, and A. D'Orazio, "Fabrication of doubly resonant plasmonic nanopatch arrays on graphene," *Applied Physics Letters*, vol. 102, no. 23, p. 231111, 2013.
- [66] H. Lin, B. C. P. Sturmberg, K.-T. Lin, Y. Yang, X. Zheng, T. K. Chong, C. M. de Sterke, and B. Jia, "A 90-nm-thick graphene metamaterial for strong and extremely broadband absorption of unpolarized light," *Nature Photonics*, vol. 13, no. 4, pp. 270–276, 2019.
- [67] N. I. Landy, S. Sajuyigbe, J. J. Mock, D. R. Smith, and W. J. Padilla, "Perfect metamaterial absorber," *Phys. Rev. Lett.*, vol. 100, p. 207402, 2008.
- [68] Y. Xiang, X. Dai, J. Guo, H. Zhang, S. Wen, and D. Tang, "Critical coupling with graphene-based hyperbolic metamaterials," *Scientific Reports*, vol. 4, no. 1, p. 5483, 2014.
- [69] K. V. Sreekanth, M. ElKabbash, Y. Alapan, A. R. Rashed, U. A. Gurkan, and G. Strangi, "A multiband perfect absorber based on hyperbolic metamaterials," *Scientific Reports*, vol. 6, no. 1, p. 26272, 2016.
- [70] T. Stomeo, A. Casolino, F. Guido, A. Quattieri, M. Scalora, A. D'Orazio, M. D. Vittorio, and M. Grande, "2d dielectric nanoimprinted pmma pillars on metallo-dielectric films," *Applied Sciences*, vol. 9, no. 18, 2019.
- [71] E. D. Palik, *Handbook of Optical Constants of Solids*. Boston: Academic Press, 1997.
- [72] I. Vassalini, I. Alessandri, and D. de Ceglia, "Stimuli-Responsive Phase Change Materials: Optical and Optoelectronic Applications.," *Materials (Basel, Switzerland)*, vol. 14, no. 12, 2021.

- [73] H. Kocer, S. Butun, B. Banar, K. Wang, S. Tongay, J. Wu, and K. Aydin, "Thermal tuning of infrared resonant absorbers based on hybrid gold-vo2 nanostructures," *Applied Physics Letters*, vol. 106, no. 16, p. 161104, 2015.
- [74] D. Yan, M. Meng, J. Li, J. Li, and X. Li, "Vanadium dioxide-assisted broadband absorption and linear-to-circular polarization conversion based on a single metasurface design for the terahertz wave," *Opt. Express*, vol. 28, no. 20, pp. 29843–29854, 2020.
- [75] W.-W. Zhang, H. Qi, A.-T. Sun, Y.-T. Ren, and J.-W. Shi, "Periodic trapezoidal vo(2)-ge multilayer absorber for dynamic radiative cooling," *Optics express*, vol. 28, no. 14, pp. 20609–20623, 2020.
- [76] J. Huang, J. Li, Y. Yang, J. Li, J. li, Y. Zhang, and J. Yao, "Active controllable dual broadband terahertz absorber based on hybrid metamaterials with vanadium dioxide," *Opt. Express*, vol. 28, no. 5, pp. 7018–7027, 2020.
- [77] P. Yu, Z.-W. Li, R. Yao, Y.-F. Xu, X.-H. Cheng, and Z.-Q. Cheng, "A tunable dual-band terahertz hybrid metamaterial absorber based on vanadium oxide (VO<sub>2</sub>) phase transition," *The European Physical Journal D*, vol. 74, no. 1, p. 5, 2020.
- [78] Z. Song and J. Zhang, "Achieving broadband absorption and polarization conversion with a vanadium dioxide metasurface in the same terahertz frequencies," *Opt. Express*, vol. 28, no. 8, pp. 12487–12497, 2020.
- [79] J. He, M. Zhang, S. Shu, Y. Yan, and M. Wang, "VO(2) based dynamic tunable absorber and its application in switchable control and real-time color display in the visible region.," *Optics express*, vol. 28, no. 25, pp. 37590–37599, 2020.
- [80] H. Kocer, S. Butun, E. Palacios, Z. Liu, S. Tongay, D. Fu, K. Wang, J. Wu, and K. Aydin, "Intensity tunable infrared broadband absorbers based on vo2 phase transition using planar layered thin films," *Scientific Reports*, vol. 5, no. 1, p. 13384, 2015.
- [81] V. I. Polozov, S. S. Maklakov, S. A. Maklakov, V. A. Chistyayev, A. A. Politiko, K. M. Baskov, A. D. Mishin, D. A. Petrov, and V. N. Kisel, "Tunable parallel plate waveguide array based on VO<sub>2</sub> thin films," *IOP Conference Series: Materials Science and Engineering*, vol. 848, no. 1, p. 012073, 2020.
- [82] M. Yi, C. Lu, Y. Gong, Z. Qi, and Y. Cui, "Dual-functional sensor based on switchable plasmonic structure of vo2 nano-crystal films and ag nanoparticles," *Opt. Express*, vol. 22, no. 24, pp. 29627–29635, 2014.
- [83] D. de Ceglia, M. A. Vincenti, M. Scalora, N. Akozbek, and M. J. Bloemer, "Plasmonic band edge effects on the transmission properties of metal gratings," *AIP Advances*, vol. 1, no. 3, p. 032151, 2011.

- [84] M. A. Kats, D. Sharma, J. Lin, P. Genevet, R. Blanchard, Z. Yang, M. M. Qazilbash, D. N. Basov, S. Ramanathan, and F. Capasso, "Ultra-thin perfect absorber employing a tunable phase change material," *Applied Physics Letters*, vol. 101, no. 22, p. 221101, 2012.
- [85] Y. Choi, D. M. Sim, Y. H. Hur, H. J. Han, and Y. S. Jung, "Synthesis of colloidal  $\text{VO}_2$  nanoparticles for thermochromic applications," *Solar Energy Materials and Solar Cells*, vol. 176, pp. 266–272, 2018.
- [86] K. Sloyan, H. Melkonyan, and M. S. Dahlem, "Focused ion beam milling for prototyping 2D and 3D photonic structures," *The International Journal of Advanced Manufacturing Technology*, vol. 107, no. 11, pp. 4469–4480, 2020.
- [87] M. Principe, M. Consales, G. Castaldi, V. Galdi, and A. Cusano, "Evaluation of fiber-optic phase-gradient meta-tips for sensing applications," *Nanomaterials and Nanotechnology*, vol. 9, p. 1847980419832724, 2019.
- [88] Q. Wang and L. Wang, "Lab-on-fiber: plasmonic nano-arrays for sensing," *Nanoscale*, vol. 12, pp. 7485–7499, 2020.
- [89] M. F. Kashif, F. Pisano, A. Balena, M. Pisanello, G. de Marzo, L. Algieri, A. Quattieri, L. Sileo, T. Stomeo, A. D'Orazio, M. D. Vittorio, F. Pisanello, and M. Grande, "Optical properties of finite subsets of fib-milled 2d periodic arrays of gold nanoplatelets with sub-20-nm gaps," in *Frontiers in Optics / Laser Science*, p. JTh4B.6, Optical Society of America, 2020.
- [90] Y. Xu, P. Bai, X. Zhou, Y. Akimov, C. E. Png, L.-K. Ang, W. Knoll, and L. Wu, "Optical refractive index sensors with plasmonic and photonic structures: Promising and inconvenient truth," *Advanced Optical Materials*, vol. 7, no. 9, p. 1801433, 2019.
- [91] J. W. Lim, D. Ha, J. Lee, S. K. Lee, and T. Kim, "Review of micro/nanotechnologies for microbial biosensors," *Frontiers in bioengineering and biotechnology*, vol. 3, p. 61, 2015.
- [92] G. Magno, M. Grande, V. Petruzzelli, and A. dorazio, "Asymmetric hybrid double dielectric loaded plasmonic waveguides for sensing applications," *Sensors and Actuators B-chemical*, vol. 186, pp. 148–155, 2013.
- [93] M. Grande, R. Marani, F. Portincasa, G. Morea, V. Petruzzelli, A. dorazio, V. Marrocco, D. de Ceglia, and M. A. Vincenti, "Asymmetric plasmonic grating for optical sensing of thin layers of organic materials," *Sensors and Actuators B-chemical*, vol. 160, pp. 1056–1062, 2011.
- [94] R. Marani, V. Marrocco, M. Grande, G. Morea, A. D'Orazio, and V. Petruzzelli, "Enhancement of extraordinary optical transmission in a double heterostructure plasmonic bandgap cavity," *Plasmonics*, vol. 6, no. 3, pp. 469–476, 2011.

- [95] P. Arora, E. Talker, N. Mazurski, and U. Levy, "Dispersion engineering with plasmonic nano structures for enhanced surface plasmon resonance sensing," *Scientific Reports*, vol. 8, no. 1, p. 9060, 2018.
- [96] H.-Y. Lin, C.-H. Huang, G.-L. Cheng, N.-K. Chen, and H.-C. Chui, "Tapered optical fiber sensor based on localized surface plasmon resonance," *Opt. Express*, vol. 20, no. 19, pp. 21693–21701, 2012.
- [97] P. Vaiano, B. Carotenuto, M. Pisco, A. Ricciardi, G. Quero, M. Consales, A. Crescitelli, E. Esposito, and A. Cusano, "Lab on fiber technology for biological sensing applications," *Laser & Photonics Reviews*, vol. 10, no. 6, pp. 922–961, 2016.
- [98] M. Pisanello, A. D. Patria, L. Sileo, B. L. Sabatini, M. D. Vittorio, and F. Pisanello, "Modal demultiplexing properties of tapered and nanostructured optical fibers for in vivo optogenetic control of neural activity," *Biomed. Opt. Express*, vol. 6, no. 10, pp. 4014–4026, 2015.
- [99] S. Aksu, M. Huang, A. Artar, A. A. Yanik, S. Selvarasah, M. R. Dokmeci, and H. Altug, "Flexible plasmonics on unconventional and nonplanar substrates," *Advanced Materials*, vol. 23, no. 38, pp. 4422–4430, 2011.
- [100] M. Kahraman, P. Daggumati, O. Kurtulus, E. Seker, and S. Wachsmann-Hogiu, "Fabrication and Characterization of Flexible and Tunable Plasmonic Nanostructures," *Scientific Reports*, vol. 3, no. 1, p. 3396, 2013.
- [101] D. Zhang, W. Yu, T. Wang, Z. Lu, and Q. Sun, "Fabrication of diffractive optical elements on 3-d curved surfaces by capillary force lithography," *Opt. Express*, vol. 18, no. 14, pp. 15009–15016, 2010.
- [102] D. Xu, J. D. Owen, J. C. Papa, J. Reimers, T. J. Suleski, J. R. Troutman, M. A. Davies, K. P. Thompson, and J. P. Rolland, "Design, fabrication, and testing of convex reflective diffraction gratings," *Opt. Express*, vol. 25, no. 13, pp. 15252–15268, 2017.
- [103] A. Tuniz and M. A. Schmidt, "Interfacing optical fibers with plasmonic nanoconcentrators," *Nanophotonics*, vol. 7, no. 7, pp. 1279–1298, 2018.
- [104] N. Vogel, S. Utech, G. T. England, T. Shirman, K. R. Phillips, N. Koay, I. B. Burgess, M. Kolle, D. A. Weitz, and J. Aizenberg, "Color from hierarchy: Diverse optical properties of micron-sized spherical colloidal assemblies," *Proceedings of the National Academy of Sciences*, vol. 112, no. 35, pp. 10845–10850, 2015.
- [105] F. J. Torcal-Milla, L. M. Sanchez-Brea, and E. Bernabeu, "Near field diffraction of cylindrical convex gratings," *Journal of Optics*, vol. 17, p. 035601, Mar. 2015.

- [106] D. Singh, A. Libster-Hershko, R. Shiloh, and A. Arie, "Curved space plasmonic optical elements," *Opt. Lett.*, vol. 44, no. 21, pp. 5234–5237, 2019.
- [107] J.-W. Liaw and P.-T. Wu, "Dispersion relation of surface plasmon wave propagating along a curved metal-dielectric interface," *Opt. Express*, vol. 16, no. 7, pp. 4945–4951, 2008.
- [108] K. Hasegawa, J. U. Nöckel, and M. Deutsch, "Curvature-induced radiation of surface plasmon polaritons propagating around bends," *Phys. Rev. A*, vol. 75, p. 063816, 2007.
- [109] H. Lee and D. Kim, "Curvature effects on flexible surface plasmon resonance biosensing: segmented-wave analysis," *Opt. Express*, vol. 24, no. 11, pp. 11994–12006, 2016.
- [110] D. Kim and E. Sim, "Segmented coupled-wave analysis of a curved wire-grid polarizer," *J. Opt. Soc. Am. A*, vol. 25, no. 3, pp. 558–565, 2008.
- [111] F. Pisano, M. F. Kashif, A. Balena, M. Pisanello, F. De Angelis, L. M. de la Prida, M. Valiente, A. D'Orazio, M. De Vittorio, M. Grande, and F. Pisanello, "Plasmonics on a neural implant: Engineering light-matter interactions on the nonplanar surface of tapered optical fibers," *Advanced Optical Materials*, p. 2101649, 2021.
- [112] S. Nie and S. R. Emory, "Probing Single Molecules and Single Nanoparticles by Surface-Enhanced Raman Scattering.," *Science (New York, N.Y.)*, vol. 275, no. 5303, pp. 1102–1106, 1997.
- [113] J. P. Scaffidi, M. K. Gregas, V. Seewaldt, and T. Vo-Dinh, "SERS-based plasmonic nanobiosensing in single living cells," *Analytical and Bioanalytical Chemistry*, vol. 393, no. 4, pp. 1135–1141, 2009.
- [114] P. L. Stiles, J. A. Dieringer, N. C. Shah, and R. P. Van Duyne, "Surface-enhanced raman spectroscopy," *Annual Review of Analytical Chemistry*, vol. 1, no. 1, pp. 601–626, 2008.
- [115] N. Gupta and A. Dhawan, "Bridged-bowtie and cross bridged-bowtie nanohole arrays as sers substrates with hotspot tunability and multi-wavelength sers response," *Opt. Express*, vol. 26, no. 14, pp. 17899–17915, 2018.
- [116] P. Savaliya and A. Dhawan, "Tapered fiber nanoprobe: plasmonic nanopillars on tapered optical fiber tips for large em enhancement," *Opt. Lett.*, vol. 41, no. 19, pp. 4582–4585, 2016.
- [117] Z. Huang, X. Lei, Y. Liu, Z. Wang, X. Wang, Z. Wang, Q. Mao, and G. Meng, "Tapered optical fiber probe assembled with plasmonic nanostructures for surface-enhanced raman scattering application," *ACS Applied Materials & Interfaces*, vol. 7, no. 31, pp. 17247–17254, 2015. PMID: 26186260.

- [118] T. Hutter, S. R. Elliott, and S. Mahajan, "Optical fibre-tip probes for sers: numerical study for design considerations," *Opt. Express*, vol. 26, no. 12, pp. 15539–15550, 2018.
- [119] J. Kwak, W. Lee, J.-B. Kim, S.-I. Bae, and K.-H. Jeong, "Fiber-optic plasmonic probe with nanogap-rich Au nanoislands for on-site surface-enhanced Raman spectroscopy using repeated solid-state dewetting," *Journal of Biomedical Optics*, vol. 24, no. 3, pp. 1 – 6, 2019.
- [120] E. J. Smythe, M. D. Dickey, J. Bao, G. M. Whitesides, and F. Capasso, "Optical antenna arrays on a fiber facet for in situ surface-enhanced raman scattering detection," *Nano Letters*, vol. 9, no. 3, pp. 1132–1138, 2009. PMID: 19236032.
- [121] D. Débarre, W. Supatto, A.-M. Pena, A. Fabre, T. Tordjmann, L. Combettes, M.-C. Schanne-Klein, and E. Beaurepaire, "Imaging lipid bodies in cells and tissues using third-harmonic generation microscopy," *Nature methods*, vol. 3, no. 1, pp. 47–53, 2006.
- [122] M.-Q. Zou, X.-F. Zhang, X.-H. Qi, H.-L. Ma, Y. Dong, C.-W. Liu, X. Guo, and H. Wang, "Rapid authentication of olive oil adulteration by Raman spectrometry," *Journal of agricultural and food chemistry*, vol. 57, no. 14, pp. 6001–6006, 2009.